Dissertation

submitted to the
Combined Faculties for the Natural Sciences and for Mathematics
of the Ruperto-Carola University of Heidelberg, Germany
for the degree of
Doctor of Natural Sciences

Put forward by
Master of Science Sascha Rau
Born in Wiesbaden
Oral examination: October 26$^{\text{th}}$, 2020

High-precision measurement of the deuteron's atomic mass

First referee:	Prof. Dr. Klaus Blaum
Second referee:	Prof. Dr. Markus Oberthaler

Hochpräzise Messung der atomaren Masse von Deuteron

Zusammenfassung - Im Rahmen dieser Doktorarbeit wurde am Penningfallen-Experiment LIONTRAP (Light-Ion TRAP) eine Messkampagne zur Bestimmung der atomaren Masse von Deuteron, dem Atomkern von Deuterium, durchgeführt. Dafür wurden wesentliche Teile der ursprünglichen Experimentieranlage umgebaut und verbessert.
Das Messprinzip im LIONTRAP-Experiment basiert auf dem Vergleich der Zyklotronfrequenz eines zu messenden Ions mit der Zyklotronfrequenz eines Kohlenstoffions, woraus die Masse in atomaren Masseneinheiten extrahiert wird. Dabei ist LIONTRAP optimiert auf die speziellen Anforderungen von leichten Ionen, da bei diesen Inkonsistenzen in der Kombination verschiedener Messungen die Verwendung der Massenwerte für Anwendungen beispielsweise in der Neutrinophysik erschweren.
In der Messkampagne gelang es, die atomare Masse von Deuterium mit einer relativen Genauigkeit von $8{,}5 \cdot 10^{-12}$ zu bestimmen. Dabei handelt es sich um die bislang genaueste Massenmessung in atomaren Masseneinheiten überhaupt. Der Wert ist um einen Faktor 2,4 genauer als die bislang weltweit genaueste Massenmessung von Deuteron und zeigt eine Diskrepanz von 5 Standardabweichungen. Zusätzlich wurde eine Massenmessung am Molekülion HD^+ durchgeführt. Die Masse dieses Molekülions kann aus der bereits von LIONTRAP gemessenen atomaren Masse des Protons und der atomaren Masse von Deuterium abgeleitet werden, da die atomare Masse des Elektrons und die molekulare Bindungsenergie hinreichend genau bekannt sind. Die Übereinstimmung beider Werte für die atomare Masse von HD^+ stellt einen starken Konsistenzcheck unserer Messmethoden dar.

High-precision measurement of the deuteron's atomic mass

Abstract - In the framework of this thesis, a measurement campaign on the atomic mass of the deuteron, the nucleus of deuterium, was conducted at the Penning-trap experiment LIONTRAP (Light-Ion TRAP). For this purpose, major parts of the original experimental facility were rebuilt and improved.
The measurement principle at LIONTRAP is based on a comparison of the cyclotron frequency of the ion to of interest and the cyclotron frequency of a carbon ion. From this, the mass in atomic mass units is deduced. LIONTRAP is optimized on the special requirements of light ions, as inconsistencies in the combination of different measurements hamper the use of their mass values for applications for example in neutrino physics.
In the measurement campaign, it was possible to measure the atomic mass of deuteron with a relative precision of $8.5 \cdot 10^{-12}$. This is the most precise measurement in atomic mass units to date. The value is a factor 2.4 more precise than the previously most precise measurement and shows a discrepancy of 5 standard deviations. Additionally, a measurement of the molecular ion HD^+ was conducted. The mass of this molecular ion can be derived from the masses of the deuteron and the proton, previously also measured at LIONTRAP. The atomic mass of the electron and the molecular binding energy are sufficiently known to not add an additional uncertainty. Both values for the atomic mass of HD^+ agree, giving a strong confidence check of the measurement methods used at LIONTRAP.

Contents

1 Introduction

The rest mass is among the fundamental properties of all atomic and subatomic particles. Although in principle, only the masses of the elemental particles are considered truly fundamental [1], it is currently impossible to relate these masses to the mass of e.g. the proton on a satisfactory level of precision [2]. However, atomic mass ratios are needed as input parameter in a wide range of experiments especially in atomic physics. This starts with the hydrogen atom, one of the simplest and at the same time best studied atomic systems, where the electron-to-proton mass ratio influences the electronic level structure [3, 4, 5]. In this way, masses, transition frequencies and other fundamental constants shape a network of parameters. In this network, new measurements are constantly used to test our understanding of the fundamental interactions and look for phenomena, which cannot be explained within our models yet.

1.1 Content of the Thesis

The main topic of this thesis is the measurement of the deuteron mass in atomic mass units at LIONTRAP [6, 7, 8]. After a general introduction, where I discuss the motivation for light ion mass measurements, especially the so-called "light ion mass puzzle", the basic principles of mass measurements of a single ion in a Penning trap are reviewed. In chapter 3, I present the LIONTRAP setup, with a special focus on the improvements carried out in the framework of this thesis. In chapter 4, several measurements performed in preparation for the deuteron mass campaign are presented. There, the improvements of the setup are evaluated and important parameters for the measurement of the deuteron mass, such as temperature and the extend of field imperfections, are determined. The measurement of the deuteron atomic mass, which is also published in [6], is described in detail in chapter 5, including an evaluation of the systematic uncertainties. Besides the mass measurement of deuteron, a mass measurement of the HD^+ molecular ion allows to show consistency within the measurements reported in this thesis and the proton mass measured previously at LIONTRAP [8, 7]. The implication of the findings of this measurement campaign in the context of other, high-precision mass measurements and recent spectroscopy results are presented. Finally, the limiting factors of the deuteron mass campaign are analyzed. In chapter 6, I give an outlook on two measurement concepts, which can potentially improve future mass measurements at LIONTRAP, but could not yet be realized for the deuteron mass measurement. Finally, I summarize the findings of this thesis.

1.2 Motivation for Light Ion Mass Measurements

The motivations for light ion mass measurements have been reviewed recently, see [9, 10]. However, the motivation for measuring the mass of deuteron is strongly dependent on the interplay with other masses in the sector of light ions, especially the mass difference between tritium (T) and helium-3 (^{3}He). Here, I explain the role of this mass difference in the context of neutrino physics and review recent discrepancies in the literature known as "light ion mass puzzle", which hinder the use of these mass value in fundamental physics applications. Furthermore, I highlight the special role of the mass of deuteron for the determination of the neutron mass and in the context of tests of the mass-energy equivalence principle $E = mc^2$.

1.2.1 The Masses of Tritium and Helium-3

During the beta decay of tritium, an electron e^- and an electron-antineutrino $\bar{\nu}_e$ are emitted. Therefore, the kinematic beta-decay spectrum contains information on the effective rest mass of neutrinos. The fact that neutrinos have mass is well known since the evidence for neutrino oscillations was found in atmospheric [11] and solar [12, 13] neutrino fluxes. However, neutrino oscillations are not sensitive to the mass values itself, but to the squared mass difference $\Delta m_{ij} = |m_i^2 + m_j^2|$, where the indices i and j indicate the mass eigenstate ($i, j \in \{1, 2, 3\}$). The direct determination of neutrino rest masses by analyzing radioactive reaction kinematics provides access to the mass values themselves and is less model dependent than other approaches like cosmological observations and the search for neutrino-less double beta decay [14, 15].
The most recent limit for the absolute mass scale of neutrinos is 1.1 eV (90 % confidence level) [16] and comes from the KATRIN collaboration (Karlsruhe Tritium Neutrino experiment). In this experiment, a windowless gaseous molecular tritium source is combined with a large MAC-E filter to record the energy spectrum of the decay electrons close to its endpoint of approximately 18.6 keV.
In figure 1.1, the expected beta decay spectrum is shown. The region close to the endpoint of the spectrum is of interest. As the electrons carry nearly all the kinetic energy and the neutrino almost none, this region is sensitive to the neutrino rest mass. A neutrino rest mass > 0 has two effects:

1. The endpoint of the spectrum is shifted towards lower energy than one would expect from the masses of the involved particles.

2. The shape of the spectrum close to the endpoint changes qualitatively. For increasing neutrino rest mass, the spectrum ends more abruptly.

At the KATRIN experiment, the limit of the neutrino rest mass is primarily extracted from the shape of the spectrum. However, the endpoint can be used as an important consistency check, as the mass difference between T and ^{3}He can be used to predict the theoretical endpoint of the spectrum. When comparing

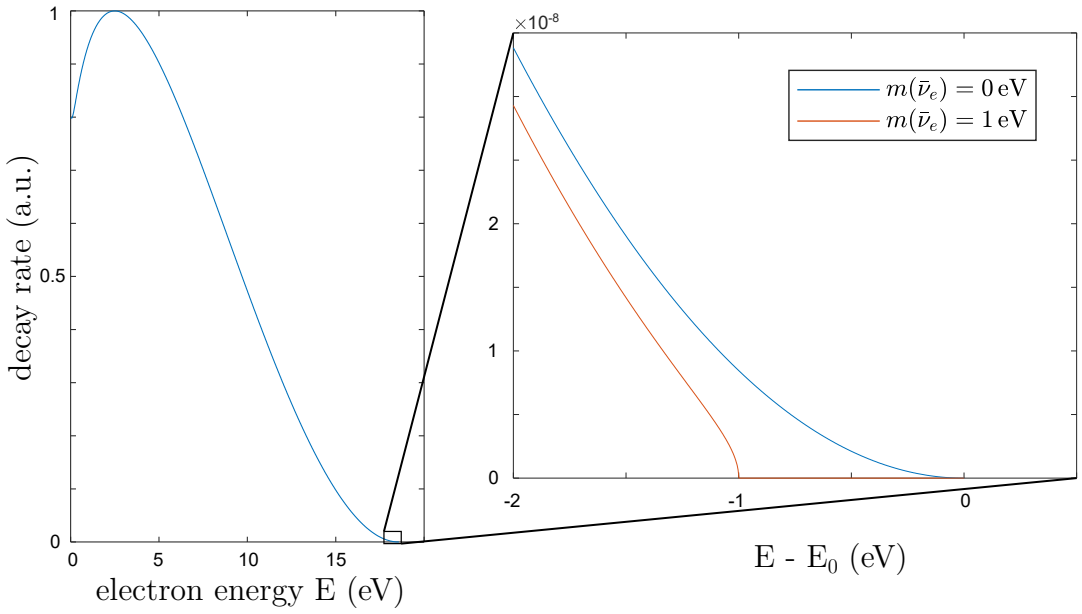

Figure 1.1: Beta-decay spectrum of tritium. Close to its endpoint, the maximum observable energy as well as the shape of the spectrum depend on the mass scale of neutrinos.

both values, one has to take various systematic effects into account, like the use of molecular instead of atomic tritium, rear-wall potentials and plasma effects. As all these effects potentially also influence the shape of the spectrum, a possibility to cross-check the modeling of these effects is of utmost importance.
The value with the lowest reported uncertainty for the mass difference of T and ^{3}He comes from the group of Ed Myers in the Florida State University (FSU)[17] and is

$$\left(M(\mathrm{T}) - M(^3\mathrm{He})\right) c^2 = 18\,592.01\,(7)\,\mathrm{eV}. \tag{1.1}$$

There, the mass difference was deduced using mass ratios of T and ^{3}He with the HD^+ molecular ion. However, plugging in the measured masses of the proton, the deuteron, the electron and the calculated molecular binding energy, this also allowed for a determination of the mass of ^{3}He in atomic mass units, which was discrepant with a direct measurement by the University of Washington (UW) [18] by $7.0\,(2.2) \cdot 10^{-9}$ u, a bit more than $3\,\sigma$. This hints towards underestimated uncertainties in at least one of the involved measurements, undermining the intended use as a consistency check for KATRIN.

1.2.2 The Puzzle of Light Ion Masses

This discrepancy was called "^{3}He puzzle" or "puzzle of light ion masses" in the literature [19, 8, 9]. Instead of expressing this inconsistency in terms of the mass

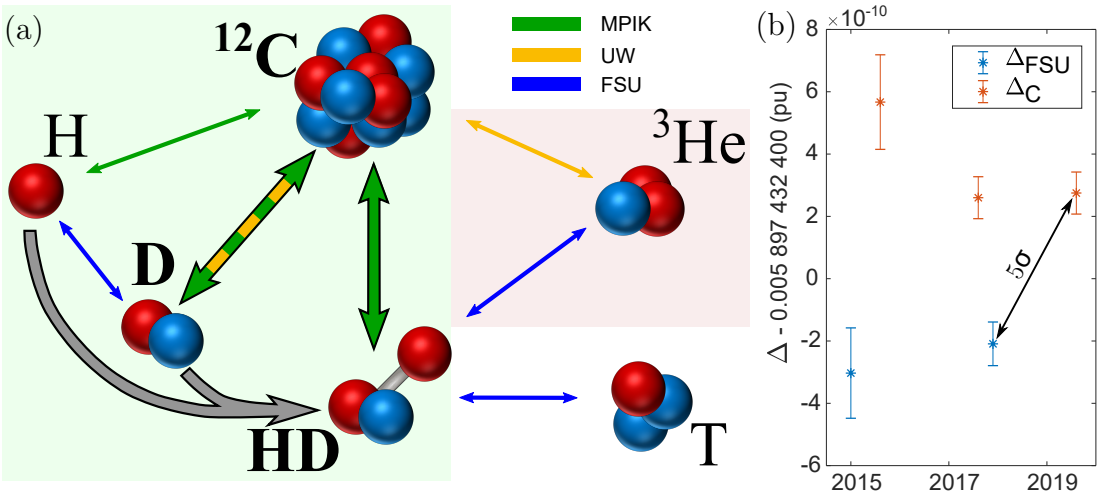

Figure 1.2: Puzzle of light ion masses. In (a), an overview of the involved nuclei and the measurements interlinking them is shown, together with the measurements presented in this thesis. Double headed arrows indicate measurements color coded by group, with the measurements reported in this thesis drawn thicker. The mass of HD^+ can be deduced from the mass of the proton and the deuteron, as the mass of the electron and the involved binding energy is known sufficiently well to not result in a loss of precision. The link between ^{3}He and T is needed for KATRIN. With the measurements in this thesis, the masses in the green area are consistent. This is no longer the case when taking into account the measurements involving ^{3}He. In (b) the values for $\Delta = m_p + m_d - m_h$ taken from mass ratio measurements of $HD^+/^3He^+$ (Δ_{FSU}) and from direct mass measurements (Δ_C) are shown. Currently both values differ by $5\,\sigma$. For details and references see text.

of ^{3}He, one can also inspect the quantity Δ defined as

$$\Delta := m_p + m_d - m_h, \tag{1.2}$$

where m_h denotes the mass of hellion, the helium-3 nucleus, and m_p and m_d denote the mass of the proton and the deuteron, respectively. This value, which is related to the proton separation energy of helium-3, can be deduced from the mass ratio of HD^+ and ^{3}He reported by the FSU (Δ_{FSU}), or by using the direct measurements of the involved masses in atomic mass units (Δ_C). In figure 1.2(a), an overview of the involved nuclei and the measurements interlinking them is shown, together with a plot on how both the values for Δ_{FSU} and Δ_C developed over the past few years. The 2015 value for Δ_C was solely given by measurements of the UW [18, 20]. For the 2017 value, the mass of the proton measured by LIONTRAP [8] was used for m_p. In 2019, this value was corrected by $15\,\mathrm{pu} \hat{=} 0.5\sigma$ [7]. The value for Δ_{FSU} was measured in 2015 [17] and remeasured with reduced uncertainty in 2017 [19]. With the measurements available in 2019, both values differed by

$$\Delta_C - \Delta_{\mathrm{FSU}} = 484\,(97)\,\mathrm{pu}. \tag{1.3}$$

While the new measurements reduced the discrepancy in absolute units, the reduced uncertainties resulted in a discrepancy of about $5\,\sigma$. To resolve this discrepancy, measurements of deuteron and helion are needed.

1.3 The Deuteron Mass

The second isotope of hydrogen was discovered in 1931 by Harold Urey using spectroscopic methods [21, 22]. Before that, Birge and Menzel [23] outlined that discrepancies in mass measurements using chemical methods [24] and a mass spectrograph [25] can be explained by the existence of a hydrogen isotope with mass two and an abundance of about 1/4500. It was named deuterium by its discoverer and colleagues [26]:

> "[...] we might reserve the name hydrogen for the natural mixture of the hydrogen isotopes, or for any other mixture where the isotopic composition is not important, and then give special names to both the H^1 and H^2 isotopes. [...] We wish to propose that the names for the H^1 and H^2 isotopes be protium and deuterium, respectively, from the Greek words protos and deuteros, meaning first and second."
>
> - Urey, Murphy and Brickwedde in [26], p. 513.

Interestingly, in this paper they also proposed the name deuteron for the nucleus of deuterium, although they disliked the idea of using that name, arguing that the deuteron was not a fundamental particle, while the proton and neutron were. Of course, it later turned out, that the proton and neutron are also not fundamental particles, at least not in the sense physicists believed back then, and the name deuteron is now frequently used. Although not yet discovered in 1933, the name tritium is already proposed in this paper.
Nowadays, the properties of deuteron like its mass [18], charge radius [27] and magnetic moment [28] are precisely measured and are used as input parameters in a range of experiments, among them hydrogen spectroscopy [27] and the spectroscopy of hydrogen molecular ions [29, 30, 31, 32].
Here, I want to highlight another application, where the deuteron mass is especially important: Its implication for the mass determination of the neutron m_n and tests of special relativity. The mass of the neutron is taken from the masses of the proton m_p, the deuteron m_d and a measurement of the neutron separation energy S_n, using $m_n = m_d - m_p + S_n(d)/c^2$. Such separation energies can be measured at neutron beam facilities [33, 34] by using the GAMS4 crystal spectrometer. There, the γ ray(s) following a neutron capture reaction are measured using Bragg spectroscopy. The neutron separation energy of deuteron of about $S_n(d) \approx 2.2\,\mathrm{MeV}$ was measured at the Institut Laue-Langevin (ILL) with a relative uncertainty of $\delta S_n(d)/S_n(d) = 1.8 \cdot 10^{-7}$ [33, 35], corresponding to a mass uncertainty of about

$4.3 \cdot 10^{-10}$ u. Currently, the separation energy measurement is limiting the determination of m_n, however, new measurements of S_n are planned in the future [36] using a newly developed spectrometer GAMS6.
By comparing the masses of heavier isotopes, which differ by one neutron, and measuring their neutron separation energy, one can test the equivalence of energy and mass, $E = mc^2$. This was done in the reactions $^{32}\mathrm{S} + n \rightarrow ^{33}\mathrm{S} + S_n(^{33}\mathrm{S})$ and $^{28}\mathrm{Si} + n \rightarrow ^{29}\mathrm{Si} + S_n(^{29}\mathrm{Si})$ [37]. In the equation

$$\left(m(^{A}\mathrm{X}) - m(^{A+1}\mathrm{X}) + m_d - m_p\right) c^2 = S_n(^{A+1}\mathrm{X}) - S_n(d), \tag{1.4}$$

the left hand side is determined via mass measurements, the right hand side via measurements of the γ energies. The test using silicon and sulfur isotopes yielded a fractional difference between the measured energies E and the mass difference Δmc^2 of $1 - \Delta mc^2/E = -1.4\,(4.4) \cdot 10^{-7}$ [37]. It should be noted, that although on the right hand side of equation (1.4) there is a difference of binding energies, the binding energy of the silicon and sulfur isotopes is with $\approx 8.6\,\mathrm{MeV}$ much higher than for deuteron, which is why these isotopes are suited for testing special relativity rather than extracting the neutron mass.
Chlorine-36 has a neutron separation energy comparable to ^{29}Si and ^{33}S, but a significantly larger cross section for neutron capture, which makes it a feasible candidate for a future improvement of the $E = mc^2$ test [38]. The current uncertainty for this separation energy is $S_n(^{36}\mathrm{Cl}) = 1.8\,\mathrm{eV}$, which corresponds to a relative precision of $2.1 \cdot 10^{-7}$. In the future, relative precisions at the level of $1 \cdot 10^{-8}$ are expected, corresponding to mass uncertainties of 92 pu. For the necessary mass measurements of ^{36}Cl and ^{35}Cl, this translates into a relative precision of $2.6 \cdot 10^{-12}$, which will be a challenge for future mass measurements. But even in the sector of light masses, this precision is challenging. The proton mass reported by LIONTRAP was differing by the UW value by 292 pu and for the deuteron mass reported in this thesis and the UW value [18] the difference is 292 pu, outlining the importance of these masses for future tests of $E = mc^2$.

2 Physics of a Single Particle in a Penning Trap

The tool used to reach the extreme precisions described in this thesis is a Penning trap. In these traps it is possible to store single ions in a nearly perfect vacuum, allowing storage times in the order of months. In this chapter I introduce the necessary background knowledge to understand our measurements. While the LIONTRAP setup is presented in detail only in chapter 3, where applicable I already introduce some numbers here, to allow the reader to get a grasp for the quantities introduced.
This chapter starts with an introduction of the Penning trap in section 2.1, beginning with an ideal Penning trap in section 2.1.1, the so-called invariance theorem in section 2.1.2 and a discussion of the effect of field inhomogeneities in section 2.1.3. The description of image current detection in section 2.2, one of the measurement methods used at LIONTRAP, is followed by an overview of different kinds of excitations and their applications in Penning traps in section 2.3. In section 2.4 I discuss the definition of the temperature of a single particle used throughout this thesis. With the techniques described in section 2.5 and section 2.6 the measurement techniques used in LIONTRAP are complete. The chapter closes with an overview of systematic frequency shifts.

2.1 The Penning Trap

In a Penning trap, particles are confined by a superposition of two static fields. A homogeneous magnetic field $\vec{B}$ confines the ion's motion in a plane perpendicular to the direction of the field, called *radial plane*. In a pure homogeneous magnetic field, the radial motion is circular with frequency

$$\omega_c = \frac{q}{m}B, \tag{2.1}$$

called the *cyclotron frequency*. Here, q and m are the ion's charge and mass. In the direction of the magnetic field, commonly referred to as *axial direction*, the ion could escape unhindered.
In a Penning trap, this escape along the magnetic field lines is prevented by a harmonic electrostatic potential, which confines the ion in the axial direction. For an overview of Penning-trap developments and applications the reader is referred to the articles by e.g. Blaum [39].

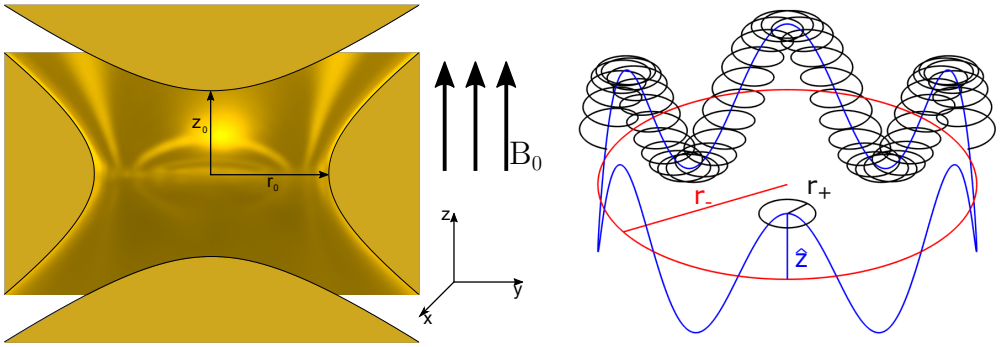

(a) Classical Penning-trap geometry (b) Penning-trap ion trajectories.

Figure 2.1: Ideal Penning trap. (a) In the classic Penning-trap geometry hyperbolically shaped electrodes with distances $r_0 = \sqrt{2}z_0$ produce an electric potential which approximates the harmonic potential of an ideal Penning trap. The geometry is symmetric with respect to rotation around the z-axis. The coordinate origin is located in the trap center, the orientation of the coordinate system is illustrated in the bottom right. (b) The motion of an ion in a Penning trap can be described as a superposition between three eigenmotions as described in the text. A fast cyclotron motion shown with amplitude r_+ (black), a slower axial motion with amplitude $\hat{z}$ (blue) and an even solower magnetron motion with amplitude r_- (red). In the sketch, $r_- > \hat{z} > r_+$, however, this generally does not have to be the case.

2.1.1 The Ideal Penning Trap

The mathematics of the ideal Penning trap have been treated extensively in the literature, see e.g. [40]. Here, the derivation and discussion of the equations of motion is shown briefly and the notation used throughout this thesis is introduced. To discuss the ideal Penning trap the system of coordinates is chosen such that the magnetic field is pointing along the z-direction,

$$\vec{B} = B_0 \hat{e_z}. \tag{2.2}$$

Here, B_0 denotes the magnitude of the magnetic field and $\hat{e}_z$ is a unit vector pointing along the z-direction of the coordinate system, see also figure 2.1a. The electrostatic quadrupolar potential has the form

$$\Phi\left(z,r\right)_{\text{ideal}} = \frac{U_r C_2}{2d_{\text{char}}^2}\left(z^2 - \frac{r^2}{2}\right), \tag{2.3}$$

where U_r is the voltage applied to the central ring electrode, $r^2 = x^2 + y^2$ and d_{char} is a *characteristic trap length*. C_2 is a dimensionless constant describing the geometry of the penning trap. While in principle only the ratio C_2/d_{char}^2 is entering the formula and the definition of both values is to some extend up to convention, this notation simplifies handling of equation (2.3) and related formulas to be introduced in section 2.1.3. For the original design of a hyperbolical Penning

trap as shown in figure 2.1a, the characteristic trap length is defined as half the distance between endcaps $d_{\text{char}} = z_0$ and $C_2 = -0.5$. Typically, even for modern traps with different designs, d_{char} is related to the physical dimensions of the trap and $C_2 \approx -0.5$.
The motion of a charged particle in these potentials can be derived analytically using non-relativistic mechanics. Relativistic corrections will be discussed in section 2.7.
From the potentials, one can derive the force acting on a particle with charge q and mass m using

$$\begin{aligned} \vec{F} &= m\ddot{\vec{x}} \\ &= -q\vec{\nabla}\Phi + q\dot{\vec{x}} \cdot \vec{B}, \end{aligned} \tag{2.4}$$

where $\vec{x}$ is the vector of coordinates, $\vec{x} = (x, y, z)$ and $\vec{\nabla}$ is the gradient operator. The dot denotes a time derivative. Explicitly, this results om

$$\ddot{x} - \omega_c \dot{y} - \frac{1}{2}\omega_z^2 x = 0, \tag{2.5a}$$

$$\ddot{y} + \omega_c \dot{x} - \frac{1}{2}\omega_z^2 y = 0, \tag{2.5b}$$

$$\ddot{z} + \omega_z^2 z = 0. \tag{2.5c}$$

Here, the *axial frequncy* ω_z has been introduced:

$$\omega_z = \sqrt{\frac{qU_r C_2}{m d_{\text{char}}^2}}. \tag{2.6}$$

The solution in the axial direction is a harmonic oscillator with frequency ω_c. The radial components can be analyzed by introducing the complex quantity $u = x + iy$. This allows combining equation (2.5a) and equation (2.5b) into

$$\ddot{u} + i\omega_c \dot{u} - \frac{1}{2}\omega_z^2 u = 0. \tag{2.7}$$

A general solution can be found using the ansatz $u = e^{-i\omega t}$, resulting in

$$\omega^2 - \omega\omega_c + \frac{1}{2}\omega_z^2 = 0. \tag{2.8}$$

The solutions for ω in equation (2.8) are the radial frequencies present in the system. These are the *modified cyclotron frequency*

$$\omega_+ = \frac{1}{2}\left(\omega_c + \sqrt{\omega_c^2 - 2\omega_z^2}\right) \tag{2.9}$$

and the *magnetron frequency*

$$\omega_- = \frac{1}{2}\left(\omega_c - \sqrt{\omega_c^2 - 2\omega_z^2}\right). \tag{2.10}$$

To obtain bound solutions, the square root term must be real valued, resulting in the *trapping condition*

$$\omega_c^2 - 2\omega_z^2 > 0. \tag{2.11}$$

The electric field is pushing the ion outwards in the radial direction, and this force cannot be greater than the force from the magnetic field trapping the ion. In typical trapping conditions, there is a strong hierachy between frequencies, $\omega_c \approx \omega_+ \gg \omega_z \gg \omega_-$.
The general solution for equation (2.7) is then

$$u(t) = u_+ e^{-i\omega_+ t} + u_- e^{-i\omega_- t}, \tag{2.12}$$

where u_+ and u_- are complex constants. Rewriting into the original coordinates yields

$$\begin{pmatrix} x \\ y \end{pmatrix} = r_+ \begin{pmatrix} \cos(\omega_+ t + \phi_+) \\ -\sin(\omega_+ t + \phi_+) \end{pmatrix} + r_- \begin{pmatrix} \cos(\omega_- t + \phi_-) \\ -\sin(\omega_- t + \phi_-) \end{pmatrix}, \tag{2.13}$$

where the starting conditions are expressed in a slightly different manner. This shows, that in the radial plane a superposition of two circular motions with radii r_+ and r_- and frequencies ω_+ and ω_- occurs. The concept of describing the radial motion of an ion in a Penning trap as superposition of two eigenmotions or modes is very fundamental and will be used throughout this thesis. The eigenmotions are sketched in figure 2.1b.
One frequently used relation between the eigenfrequencies is

$$\omega_+ \omega_z = \frac{1}{2}\omega_z^2. \tag{2.14}$$

The energy associated with these modes can be calculated [41, Appendix A] as

$$E_+ = \frac{1}{2} m\omega_+ (\omega_+ - \omega_-) r_+^2 \approx \frac{1}{2} m\omega_+^2 r_+^2, \tag{2.15a}$$

$$E_- = -\frac{1}{2} m\omega_- (\omega_+ - \omega_-) r_-^2 \approx -\frac{1}{4} m\omega_z^2 r_-^2, \tag{2.15b}$$

$$E_z = \frac{1}{2} m\omega_z^2 \hat{z}^2, \tag{2.15c}$$

where $\hat{z}$ is the maximum amplitude of the axial oscillation. The energy associated with the magnetron motion E_- is always negative. This is because for the slow magnetron motion the kinetic energy is much smaller than the potential energy in the electric field. Therefore, the magnetron motion is metastable, any kind of loss mechanism results in an increase of the magnetron radius r_- and eventually in a loss of the ion.
While for ions at typical cryogenic temperatures a classical description usually suffices, a quantum mechanical approach yields essentially the same result. The

motion is described as a superposition of three independent harmonic oscillators with energies

$$E_+ = \left(n_+ + \frac{1}{2}\right)\hbar\omega_+, \tag{2.16a}$$

$$E_- = -\left(n_- + \frac{1}{2}\right)\hbar\omega_-, \tag{2.16b}$$

$$E_z = \left(n_z + \frac{1}{2}\right)\hbar\omega_z. \tag{2.16c}$$

The quantum numbers n_+, n_-, $n_z \in \mathbb{N}_0$ are typically large, which will be discussed in section 2.4, justifying a classical treatment. However, introducing them here will turn out to be useful in the discussion of excitations in section 2.3. While the observable quantities are the eigenfrequencies, in the end one is interested in the free space cyclotron frequency ω_c, which needs to be extracted from the measured eigenfrequencies.

2.1.2 Invariance Theorem

To extract the free space cyclotron frequency ω_c from the three measurable eigenfrquencies, various approaches are possible. One obvious choice would be using the formula $\omega_c = \omega_+ + \omega_-$, which is done in various online facilities [39, 42, 43]. In FTICR trace analysis [44], just ω_+ is measured, and the effect of the trapping field is calibrated using known masses. In precision physics with stable ions, the use of a so-called invariance theorem [40] has been established. There, the free cyclotron frequency is derived using

$$\omega_c = \sqrt{\omega_+^2 + \omega_z^2 + \omega_-^2}. \tag{2.17}$$

While it is easy to check that equation (2.17) is true for an ideal trap, it also holds if there is an angle between the axes of the electric and the magnetic field and if the electric field has an ellipticity. More explicitly, it can be shown that the potential can always be written as

$$\Phi\left(x, y, z\right) \propto z^2 - \frac{1}{2}\left(x^2 + y^2\right) - \frac{1}{2}\epsilon\left(x^2 - y^2\right), \tag{2.18}$$

see e.g. [45]. The parameter ϵ describes the ellipticity of the electric field and the x- and y-axis are chosen such that they correspond to the minor and major semi-axis of the elliptical field, respectively. Such an ellipticity can easily origin in geometric imperfections of the trap electrodes in use.
In this system of coordinates, the homogeneous magnetic field can be written with two angles θ and ϕ. The angle between the magnetic field and the z-axis of the electrostatic field is described with θ, the angle ϕ describes the orientation of the magnetic field with respect to the semi-axes of the elliptical electric field,

$$\vec{B} = B_0 \begin{pmatrix} \cos(\theta) \\ \sin(\theta)\cos(\phi) \\ \sin(\theta)\sin(\phi) \end{pmatrix}. \tag{2.19}$$

For small imperfections $\theta \ll 1$ and $\epsilon \ll 1$, the eigenfrequencies shift in the following way (see appendix A.1):

$$\Delta\omega_+ = \frac{\omega_{z,0}^2}{\omega_{+,0}}\frac{3}{4}\theta^2\left(1+\frac{1}{3}\epsilon\cos(2\phi)\right) + \frac{\omega_{-,0}^2}{2\omega_{+,0}}\epsilon^2, \tag{2.20a}$$

$$\Delta\omega_z = -\frac{3}{4}\omega_{z,0}\theta^2\left(1+\frac{1}{3}\epsilon\cos(2\phi)\right), \tag{2.20b}$$

$$\Delta\omega_- = \frac{3}{4}\omega_{-,0}\theta^2\left(1+\frac{1}{3}\epsilon\cos(2\phi)\right) + \frac{1}{2}\omega_{-,0}\epsilon^2. \tag{2.20c}$$

Throughout this thesis, frequency shifts use the sign convention

$$\omega_{\text{shifted}} = \omega_{\text{unshifted}} + \Delta\omega, \tag{2.21}$$

where ω_{shifted} is the frequency measured and $\omega_{\text{unshifted}}$ is the frequency one would measure in an ideal trap. The frequencies marked with an index "0" refer to the unshifted frequency. However, when actually calculating the value of these frequency shifts one can without problems use the measured frequencies and the index is often omitted.
One way to get information on the angle is to compare the cyclotron frequency determined by the invariance theorem with the sum of the radial mode frequencies. This yields [42]

$$\omega_+ + \omega_- - \sqrt{\omega_+^2 + \omega_z^2 + \omega_-^2} = \omega_-\left(\frac{9}{4}\theta^2 - \frac{1}{2}\epsilon^2\right). \tag{2.22}$$

Usually one then assumes ϵ to be small from geometric considerations and attributes the remaining difference to the angle.

2.1.3 Field Imperfections

In real Penning traps, the electric and magnetic fields only approximate the ideal situation introduced in section 2.1.1. The effect of field imperfections is discussed for example in [46]. Here, the main results are briefly summarized.
Generally, inhomogeneities and anharmonicities lead to motional sidebands at higher harmonics of the fundamental frequency and a shift of the fundamental frequency. These effects depend on the motional amplitudes of the ion. For small perturbations, the motional sidebands can be neglected and only the frequency shifts need to be considered.

Electrostatic Imperfections

To describe the effect of electrostatic imperfections, one utilizes that the electrodes are in good approximation cylindrical-symmetric. Therefore, also the electrostatic potential has to be cylindrical-symmetric. This information can be used to write the potential as a series. Additionally, the Penning trap is usually operated with voltages symmetric with respect to a mirror transformation $z \to -z$, which allows

neglecting the odd order terms. The potential then can be written in a series expansion having the following form:

$$\begin{aligned}\Phi(r,z) = \frac{U_r}{2}\Bigg[&\frac{C_2}{d_{\text{char}}^2}\left(z^2 - \frac{r^2}{2}\right)\\ &+ \frac{C_4}{d_{\text{char}}^4}\left(z^4 - 3z^2r^2 + \frac{3}{8}r^4\right)\\ &+ \frac{C_6}{d_{\text{char}}^6}\left(z^6 - \frac{15}{2}z^4r^2 + \frac{45}{8}z^2r^4 - \frac{5}{16}r^6\right)\\ &+ ...\Bigg].\end{aligned} \tag{2.23}$$

The anharmonicity of the electric field is effectively described by the coefficients C_n, $i \in 4, 6, ...$, which will be extensively used in section 4.2.
For the leading order anharmonicity described by the coefficient C_4, the first order frequency shifts are [46]

$$\Delta\omega_z = \omega_z \frac{C_4}{C_2}\frac{3}{4d_{\text{char}}^2}\left(\hat{z}^2 - 2r_+^2 - 2r_-^2\right), \tag{2.24a}$$

$$\Delta\omega_\pm = \mp\frac{C_4}{C_2}\frac{3}{2d_{\text{char}}^2}\frac{\omega_+\omega_-}{\omega_+ - \omega_-}\left(2\hat{z}^2 - r_\pm^2 - 2r_\mp^2\right). \tag{2.24b}$$

In equation (2.24b) the upper index describes the frequency shift of ω_+, the lower index describes ω_-. The overall amplitude of the frequency shifts is determined by the ratio C_4/C_2, which is typically small ($< 10^{-5}$). The shifts scale with the motional amplitudes divided by the characteristic trap length d_{char}. For motional amplitudes approaching d_{char}, the series expansion approach is no longer valid.
The first order frequency shifts caused by the next to leading order even anharmonicity are [46]

$$\Delta\omega_z = \omega_z \frac{C_6}{C_2}\frac{15}{16d_{\text{char}}^4}\left(\hat{z}^4 + 3r_+^4 + 3r_-^4 - 6r_+^2\hat{z}^2 - 6r_-^2\hat{z}^2 + 12r_+^2r_-^2\right), \tag{2.25a}$$

$$\begin{aligned}\Delta\omega_\pm = \mp\frac{C_6}{C_2}\frac{15}{8d_{\text{char}}^4}\frac{\omega_+\omega_-}{\omega_+ - \omega_-}\Big(&3\hat{z}^4 + r_\pm^4 + 3r_\mp^4\\ &-6r_\pm\hat{z}^2 - 12r_\mp^2\hat{z}^2 + 6r_+^2r_-^2\Big).\end{aligned} \tag{2.25b}$$

Again, the ratio of the coefficient describing the inhomogeneity C_6 and C_2 determines the overall strength of the frequency shifts. However, now with the motional amplitudes going into the equation in 4^{th} order, cross-terms appear. In practical applications, it often suffices to consider only the amplitude of one of the three modes and put the others as zero. For example, the shift of the axial frequency ω_z as function of the magnetron radius r_- then becomes

$$\frac{\Delta\omega_z}{\omega_z} = -\frac{C_4}{C_2}\frac{3}{2}\left(\frac{r_-}{d_{\text{char}}}\right)^2 + \frac{C_6}{C_2}\frac{45}{16}\left(\frac{r_-}{d_{\text{char}}}\right)^4, \tag{2.26}$$

where the terms are grouped slightly different to clarify the meaning of equation (2.26). One essentially has a power series in even powers of r_-/d_{char}, with the

coefficients C_n/C_2. This equation can be used to optimize the trap potential as discussed in section 4.2.
It is noteworthy, that situations can occur where the assumption of an axially symmetric trap potential do not hold and odd orders in the potential need to be considered. This is especially the case when asymmetric voltages are intentionally applied to shift the ion position in a controlled way: adding a linear term to the harmonic potential will lead again to a harmonic potential with a shifted minimum. The first anharmonicity to be discussed is then the order corresponding to the C_3 coefficient. Using the ideas discussed above, the potential then can be written as

$$\Phi\left(z,r\right)=\frac{U_r}{2}\left[\frac{C_2}{d_{\mathrm{char}}^2}\left(z^2-\frac{r^2}{2}\right)+\frac{C_3}{d_{\mathrm{char}}^3}\left(z^3-\frac{3}{2}r^2z\right)\right]. \tag{2.27}$$

Here, only the effect on the axial frequency ω_z as function of the motional amplitudes in the axial and magnetron mode shall be discussed, as this is used for trap optimization.
When only looking at the axial dependence ($r=0$), one has an anharmonic oscillator with a potential $\Phi\propto z^2+\frac{C_3}{C_2 d_{\mathrm{char}}}z^3$. The equation of motion in such a potential can be solved analytically [47]. For small pertubations $C_3/C_2\ll 1$ and small motional amplitudes $\hat{z}\ll d_{\mathrm{char}}$, the resulting motion is essentially again a harmonic oscillation with shifted equilibrium position and frequency, $z(t)\approx\hat{z}\cos((\omega_z+\Delta\omega_z)t)+\Delta z$, with

$$\Delta z\approx-\frac{3}{4}\frac{C_3}{C_2 d_{\mathrm{char}}}\hat{z}^2, \tag{2.28}$$

$$\frac{\Delta\omega_z}{\omega_z}\approx-\frac{15}{16}\frac{C_3^2}{C_2^2 d_{\mathrm{char}}^2}\hat{z}^2. \tag{2.29}$$

A particle with significant amplitude in the magnetron motion and small axial amplitude will experience an axial confinement with potential $\Phi\propto z^2-\frac{3}{2}\frac{C_3}{C_2 d_{\mathrm{char}}}r_-^2 z$, neglecting the z^3 term. The linear term again leads to a shifted equilibrium position. A series expansion of the potential around this new equilibrium potential yields the frequency shift

$$\frac{\Delta\omega_z}{\omega_z}=\frac{9}{8}\frac{C_3^2}{C_2^2 d_{\mathrm{char}}^2}r_-^2. \tag{2.30}$$

This calculation is instructive for two reasons: First of all, it becomes clear that the leading order frequency shift from odd order coefficients is proportional to the field coefficient squared, further justifying neglecting them above. Secondly, when optimizing the trap potential, this is usually done by looking at axial frequency shifts as function of the magnetron radius r_-. Then the potential is altered, until the term proportional to r_-^2 becomes zero. In the presence of a significant C_3 this will still be possible, however, this optimization will not result in $C_4=0$ as desired, but in $C_4=\frac{3C_3^2}{4C_2}$. When reinserting this into equation (2.30) and equation (2.24a), it becomes apparent that the axial frequency ω_z is not anymore independent of the axial amplitude $\hat{z}$. If one is going to perform measurements in such a situation, this would result in significant errors.

Magnetostatic Inhomogeneities

Magnetostatic inhomogeneities can be written in a general form using similar arguments as for the electric field. For the general form, see [46], here the explicit form of the most relevant contributions is discussed. Again, only the even order contributions lead to a shift in first order.
The quadratic inhomogeneity B_2 can be written in cylindrical coordinates as

$$\vec{B}_2 = B_2 \left[\left(z^2 - \frac{1}{2} r^2 \right) \hat{e}_z - z r \hat{e}_r \right], \tag{2.31}$$

where B_2 is a parameter describing the strength of the inhomogeneity in units tesla per meter squared. This inhomogeneity leads to shifted eigenfrequencies

$$\frac{\Delta\omega_+}{\omega_+} = \frac{B_2}{2B_0} \frac{\omega_+ + \omega_-}{\omega_+ - \omega_-} \left(\hat{z}^2 - r_+^2 - \left(1 + \frac{\omega_-}{\omega_+} \right) r_-^2 \right), \tag{2.32a}$$

$$\frac{\Delta\omega_z}{\omega_z} = \frac{B_2}{4B_0} \frac{\omega_+ + \omega_-}{\omega_+ \omega_-} \left(\omega_+ r_+^2 + \omega_- r_-^2 \right), \tag{2.32b}$$

$$\frac{\Delta\omega_-}{\omega_-} = -\frac{B_2}{2B_0} \frac{\omega_+ + \omega_-}{\omega_+ - \omega_-} \left(\hat{z}^2 - \left(1 + \frac{\omega_+}{\omega_-} \right) r_+^2 - r_-^2 \right). \tag{2.32c}$$

The structure of the formulas is very similar to the frequency shifts arising from the first order electric anharmonicity C_4 described in equation (2.24). Now the magnitude of the shift is described by the ratio B_2/B_0, to be compared with C_4/C_6. However, in B_2 the unit length is already absorbed, for the electric anharmonicities this was covered by the characteristic trap length d_{char}.
The next higher order is

$$\vec{B}_4 = B_4 \left[\left(z^4 - 3z^2 r^2 + \frac{3}{8} r^4 \right) \hat{e}_z + \left(-2z^3 r + \frac{3}{2} z r^3 \right) \hat{e}_r \right], \tag{2.33}$$

leading to frequency shifts

$$\begin{aligned} \frac{\Delta\omega_+}{\omega_+} =& \frac{3B_4}{8B_0} \frac{\omega_+ + \omega_-}{\omega_+ - \omega_-} \left(r_+^4 + \hat{z}^4 + \left(1 + 2\frac{\omega_-}{\omega_+} \right) r_-^4 \right. \\ & \left. -4 r_+^2 \hat{z}^2 - 4 \left(1 + \frac{\omega_-}{\omega_+} \right) r_-^2 \hat{z}^2 + 4 \left(1 + \frac{\omega_-}{2\omega_+} \right) r_+^2 r_-^2 \right], \end{aligned} \tag{2.34a}$$

$$\begin{aligned} \frac{\Delta\omega_z}{\omega_z} =& \frac{3B_4}{8B_0} \frac{\omega_+ + \omega_-}{\omega_+ \omega_-} \left(-\omega_+ r_+^4 - \omega_- r_-^4 \right. \\ & \left. +\omega_+ r_+^2 \hat{z}^2 + \omega_- r_-^2 \hat{z}^2 - 2(\omega_+ + \omega_-) r_+^2 r_-^2 \right), \end{aligned} \tag{2.34b}$$

$$\begin{aligned} \frac{\Delta\omega_-}{\omega_-} =& -\frac{3B_4}{8B_0} \frac{\omega_+ + \omega_-}{\omega_+ - \omega_-} \left(\left(1 + 2\frac{\omega_+}{\omega_-} \right) r_+^4 + \hat{z}^4 + r_-^4 \right. \\ & \left. -4 \left(1 + \frac{\omega_+}{\omega_-} \right) r_+^2 \hat{z}^2 - 4 r_-^2 \hat{z}^2 + 4 \left(1 + \frac{\omega_+}{2\omega_-} \right) r_+^2 r_-^2 \right]. \end{aligned} \tag{2.34c}$$

Unlike for the electric imperfections, there is no argument for the odd order coefficients naturally being small. Indeed it turns out, that on the scale of typical motional amplitudes the linear imperfection is bigger than the quadratic one. Although the corresponding shift is only of order B_1^2, it still needs to be checked. The linear inhomogeneity can be written as

$$\vec{B}_1 = B_1 \left(z\hat{e}_z - \frac{r}{2}\hat{e}_r \right). \tag{2.35}$$

The dominating frequency shift from B_1 comes from the magnetic moment associated with the cyclotron motion $|\mu| = \frac{qr_+^2\omega_+}{2}$. This leads to a force in the inhomogenic magnetic field and thus a new equilibrium position shifted by $\Delta z = -\frac{B_1}{B_0}\frac{\omega_+\omega_c}{2\omega_z^2}r_+^2$. The magnetic field at this new equilibrium position is different, leading to a frequency shift

$$\frac{\Delta\omega_+}{\omega_+} \approx \frac{B_1\Delta z}{B_0} = -\left(\frac{B_1}{B_0}\right)^2 \frac{\omega_+\omega_c}{2\omega_z^2} r_+^2. \tag{2.36}$$

2.2 Image Current Detection

In the previous section I discussed the motion of a single ion in a Penning trap, how the motion can be describedy by three eigenmotions and how they are affected by field imperfections. However, we still did not discuss how we actually measure the eigenfrequencies at LIONTRAP. This section introduces the image current detection, which is used at LIONTRAP not only to measure the axial frequency ω_z, but also ω_+ and ω_- through couplings to the axial motion. The basic idea is to transform tiny image currents induced by the ion into measurable voltages using a resonator. There, the ion appears as a distinct feature called *dip* in the Fourier transformed signal of the thermal noise spectrum of the resonator. In the following sections I will explain the concepts behind this in detail.

2.2.1 Image Currents

An ion sitting above a conducting surface induces charges into this surface. For a flat surface this happens in a way that the field looks as if there was an image charge of the same size but with the opposite sign on the other side of the surface [48]. This simple principle is sketched in figure 2.2a and builds the basis on how we detect the axial motion of ions at LIONTRAP. The motion of ions induces currents in the electrodes of the Penning trap.
To calculate the currents induced by an ion in the vicinity of an electrode, we can use the Shockley-Ramo theorem [49]. It states that the electric current i_{ind} induced by an ion with charge q moving with velocity $\vec{v}$ is

$$i_{\text{ind}} = q\vec{v} \cdot \vec{E}_w(\vec{x}(t)). \tag{2.37}$$

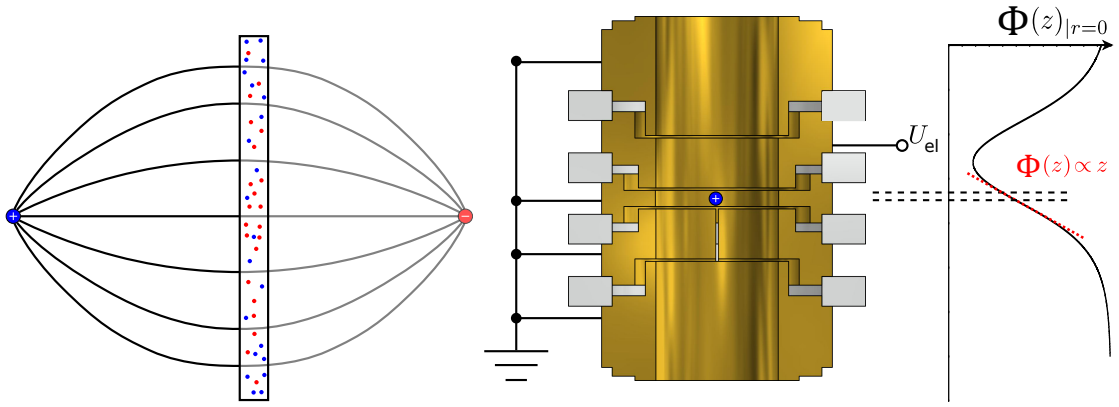

(a) (b)

Figure 2.2: (a) An ion close to a conducting surface induces a charge density in the surface, such that the electric field lines look like there is an image charge with the surface as mirror axis. (b) Illustration of the effective electrode distance. The potential from the electrode of interest is simulated with the other electrodes on ground. In the range of axial motion, this potential is linearly approximated.

Here, $\cdot$ denotes the dot product between vectors and $\vec{E}_w(\vec{x}(t)) = \vec{E}(\vec{x}(t))/U_{\text{el}}$ is the so called *weighting field*, the field produced by the electrode normalized to 1 V. This means for the axial motion, we look at the derivative in z-direction of the potential created by this electrode. For the center electrode this would be zero, that is why we have to use an off-center electrode as shown in figure 2.2b. The electric potential usually can be approximated linearly in the range of the axial motion, so the field is a constant. Often, the inverse of the weighting field, the so called *effective electrode distance*, is used,

$$D = \frac{1}{|E_{w,z}(\vec{x} = 0)|}. \tag{2.38}$$

While in this section the effective electrode distance always refers to the z-component of the weighting field $E_{w,z}$, this does not have to be the case for example for the image current detection of the radial modes or excitations as described in section 2.3. Inserting the ion's axial motion as $z(t) = \hat{z}\cos(\omega_z t)$ into equation (2.37) yields

$$\begin{aligned} i_{\text{ind}}(t) &= \frac{q}{D}\dot{z}(t) = -\frac{q\omega_z}{D}\hat{z}\sin(\omega_z t) \\ \rightarrow \langle i_{\text{ind}}(t)\rangle &= i_{\text{ind}}^{\text{rms}} = \frac{q}{D}\frac{\hat{z}}{\sqrt{2}}\omega_z. \end{aligned} \tag{2.39}$$

In our measurement trap, we have $D = 9.6\,\text{mm}$. For a deuteron with charge $q = 1\,e$, frequency $\omega_z \approx 2\pi \cdot 460\,\text{kHz}$ and a motional amplitude of about $\hat{z} \approx 10\,\mu\text{m}$, this results in a current of only 0.3 fA (femtoampere). To transform such a small current into a measurable voltage, according to Ohm's law $U = ZI$ the absolute value of the impedance Z at the axial frequency should be as high as possible. However, the capacitances between traps in the order of a few picofarad (pF)

would limit the useful range for a resistor to some kiloohms, which is by far not sufficient. Therefore, a resonant tank circuit as described in the following section is commonly used.

2.2.2 Tank Circuit

A tank circuit or resonator is essentially a coil connected to the trap electrode. Together with the capacitance of the trap, sometimes some additionally added capacitance, and the capacitance in the coil, this forms an LC-circuit as shown in figure 2.3. Usually, the coil is made from superconducting material. Effects like dielectric losses in the isolation, losses in the normal conducting connection to the trap electrode or even AC losses in normal conducting material close by limit the fidelity of the system and are modeled as a resistor parallel to the coil. In this model, the impedance of the detection system can be written in the form

$$\begin{aligned} Z &= \frac{1}{\frac{1}{i\omega L} + i\omega C + \frac{1}{R_P}} \\ &= \frac{R_P}{1 + iQ\left(\frac{\omega}{\omega_{\mathrm{res}}} - \frac{\omega_{\mathrm{res}}}{\omega}\right)}. \end{aligned} \tag{2.40}$$

The real part of this impedance as a function of frequency ω forms a resonance curve and has a maximum at the resonance frequency $\omega_{\mathrm{res}} = \frac{1}{\sqrt{LC}}$, at which the circuit acts as a pure ohmic resistor with efffective resistance R_p. The width of this resonance is described by the quality factor or Q-value, $Q = \omega_{\mathrm{res}}/\Delta\omega$, with the full width at half maximum (FWHM) $\Delta\omega$ of the real part of the impedance. In practice, one tries to minimize the losses as far as possible. How well exactly this worked, one then can estimate by measuring the Q-value with the LC-circuit installed in the experiment. The effective parallel resistance R_P can be calculated as

$$R_P = Q\omega_{\mathrm{res}}L. \tag{2.41}$$

2.2.3 Thermal Noise Spectrum

Even without any external voltage applied, the resonator described in section 2.2.2 will always produce a thermal voltage noise. The fact, that any electronic circuit produces such a voltage, has been discovered by John Johnson [50] and explained by Harry Nyquist [51], and is called *Johnson Noise* or *Johnson-Nyquist Noise*. The rms (root mean square) voltage u_n at a frequency bandwidth $\Delta\nu$ is given by

$$u_n = \sqrt{4k_B T\,\mathrm{Re}(Z)\Delta\nu}, \tag{2.42}$$

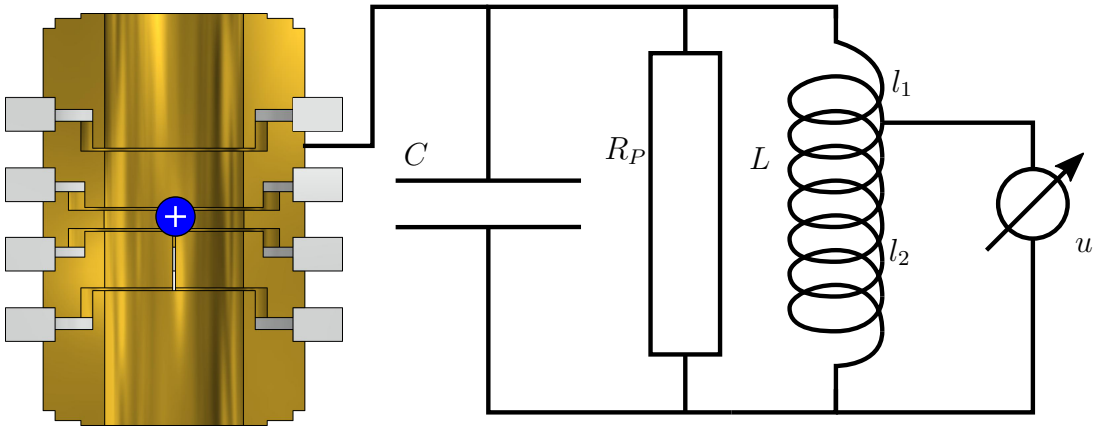

Figure 2.3: Schematic sketch of an LC- or tank circuit. The capacitance C, in which the trap capacitance and any additional capacitance are absorbed, builds together with the inductance L a resonant circuit. The losses in this circuit are modeled as a parallel resistance R_P. To limit the effect of noise from the following amplifier chain, the voltage is usually tapped towards the grounding end of the coil, at LIONTRAP $l_1 = 10l_2$.

where k_B is the Boltzmann constant and T is the temperature of the electrons in the circuit. Plugging in equation (2.40) for the impedance, one arrives at

$$u_n^{\text{res}} = \sqrt{\frac{4k_B T R_P \Delta\nu}{1 + Q^2\left(\frac{\omega}{\omega_{\text{res}}} - \frac{\omega_{\text{res}}}{\omega}\right)^2}}. \tag{2.43}$$

In practice, the frequency bandwidth $\Delta\nu$ is given by the resolution of the Fourier transform. This voltage is amplified by a low-noise cryogenic amplifier developed by Sven Sturm in our group [52]. In the room temperature section, the signal is further amplified, mixed down into the audio range and Fourier transformed. To get the finally observed lineshape, we have to include several other effects. The cryogenic amplifier adds a noise level u_n^{ampl}. This noise has several frequency components, which scale differently with the frequency. There are for example white noise components and $1/\nu$ components. However, for the relatively small frequency range of at most a few kHz we are interested in, this can be taken as white noise denoted as u_n^{ampl}. Additionally, we allow for the transfer function of the system to have a slight frequency dependence, which we approximate linearly with slope κ_{det} in the region around ω_{res}. Finally, the complete signal is amplified by a parameter A. The lineshape we get on our fast Fourier transform (FFT) device then reads

$$u_n^{\text{res,FFT}} = A\left(1 + \kappa_{\text{det}}(\omega - \omega_{\text{res}})\right)\sqrt{(u_n^{\text{res}})^2 + (u_n^{\text{ampl}})^2}. \tag{2.44}$$

This lineshape is usually displayed and fitted in logarithmic units (dBVrms). This

has the advantage, that the weights during fitting are automatically correct [1]. To get to dBVrms, one has to take the logarithm with basis 10 and multiply with 20. The lineshape in dBVrms can be rewritten as

$$20\log_{10} u_n^{\mathrm{res,FFT}} \approx 10\log_{10}\left[\tilde{A}\,\mathrm{Re}(Z)/R_P + (\tilde{u}_n^{\mathrm{ampl}})^2\right] + \tilde{\kappa}_{\mathrm{det}}(\omega-\omega_{\mathrm{res}}), \qquad (2.45)$$

using $\log_{10}(1+\kappa(\omega-\omega_{\mathrm{res}})) \approx \kappa(\omega-\omega_{\mathrm{res}})/\ln(10)$. The newly defined parameters

$$\begin{aligned} \tilde{A} &= A^2 4k_B T R_P \Delta\nu, \\ \tilde{u}_n^{\mathrm{ampl}} &= A u_n^{\mathrm{ampl}}, \\ \tilde{\kappa}_{\mathrm{det}} &= 20\kappa_{\mathrm{det}}/\ln(10), \end{aligned} \qquad (2.46)$$

are together with Q and ω_{res} fitted parameters. The resistance is kept explicitly in equation (2.45) because in this way $\mathrm{Re}(Z)/R_P$ is dimensionless.

2.2.4 Interaction between the Ion and the Tank Circuit

In this section an analysis of the interaction between the detection system introduced in section 2.2.2 and a single trapped ion will be presented. We will see, that the ion's motion is damped and thermalizes with the tank circuit. This *resistive cooling* was first demonstrated by Wineland and Dehmelt in 1975 [53]. To describe the interaction we need to find an expression which relates the ion's motion to the electric field originating in the current induced in the electrode with the resonator attached.

In equation (2.39) the current i_{ind} induced by the ion was calculated. The electric field produced by a voltage u_{ind} at the resonator electrode is $E_z = -\frac{u_{\mathrm{ind}}}{D}$ from equations (2.37) and (2.38). However, relating the induced voltage to the current by using $u_{\mathrm{ind}} = Z i_{\mathrm{ind}}$ is tricky, as the physical quantities described are real valued, but the concept of the electric impedance Z uses a complex quantity to describe phase shifts. To solve this rigorously, one needs to describe both the voltage in the LC-circuit and the motion of the ion as differential equations. The current induced by the ion acts as a source term for the LC-circuit, and the voltage in the LC-circuit acts as a drive for the ion's motion. Solving this system of coupled differential equations becomes rather lengthy. However, using the phase relation between a sinusoidal current and the resulting voltage for a complex impedance, one can convince oneself that the force acting on the ion can be written as

$$\begin{aligned} F_z = qE_z &= -q\frac{u_{\mathrm{ind}}}{D} \\ &= -\frac{q^2}{D^2}\,\mathrm{Re}(Z)\dot{z} + \frac{q^2}{D^2}\,\mathrm{Im}(Z)\omega_z z. \end{aligned} \qquad (2.47)$$

[1] As a noise quantity, the uncertainty of u_n is proportional to its value. The uncertainty of $\log u_n$ is then $\delta \log u_n = \frac{1}{u_n}\delta u_n = \mathrm{const}$.

Adding this to the differential equation 2.5c, one arrives at

$$\ddot{z} + 2\gamma\dot{z} + \tilde{\omega}_z^2 z = 0, \tag{2.48}$$

where $\gamma = \frac{q^2\,\mathrm{Re}(Z)}{2mD^2}$ and $\tilde{\omega}_z^2 = \omega_z^2 - \frac{q^2\omega_z\,\mathrm{Im}(Z)}{mD^2}$. This is the standard equation of motion for a damped harmonic oscillator, with shifted frequency

$$\tilde{\omega}_z - \omega_z \approx -\frac{q^2\,\mathrm{Im}(Z)}{2mD^2}. \tag{2.49}$$

The amplitude of the ion's motion is damped with damping constant γ. Usually, one defines the cooling time constant

$$\tau = \frac{1}{2\gamma} = \frac{mD^2}{q^2\,\mathrm{Re}(Z)}, \tag{2.50}$$

such that the energy, which is proportional to the amplitude squared, has a damping proportional to $\exp(-t/\tau)$. This timing constant depends on the involved frequencies. Since the strongest damping occurs at resonance, we define

$$\tilde{\tau} = \tau(\omega_z) = \omega_{\mathrm{res}} = \frac{mD^2}{q^2 R_p}. \tag{2.51}$$

At LIONTRAP the damping constant for a single deuteron is about $\tilde{\tau} = 0.3\,\mathrm{sec}$, much slower than the axial oscillation. Therefore, the effect of the damping on the frequency can be safely neglected, the shift described in equation (2.49) is dominant. This shift is referred to as *image current shift*.
After a few seconds, the ion will get into thermal equilibrium with the resonator, which at LIONTRAP is at 4.2 K. To describe the signal one gets from an ion which is in thermal equilibrium with a tank circuit, it is useful to develop a circuit representation of the ion. Therefore, we rewrite the equation of motion to

$$0 = \ddot{z} + \omega_z^2 + \frac{u_{\mathrm{ind}} q}{mD}. \tag{2.52}$$

Now we can solve this for u_{ind}, and substitute the coordinate z by the current induced by the ion $i_{\mathrm{ind}} = \frac{q}{D}\dot{z}$, resulting in

$$u_{\mathrm{ind}} = \underbrace{\frac{\omega_z^2 mD^2}{q^2}}_{=:C_{\mathrm{ion}}^{-1}} \int i\,\mathrm{d}t + \underbrace{\frac{mD^2}{q^2}}_{=:L_{\mathrm{ion}}} \frac{\partial i}{\partial t}. \tag{2.53}$$

This calculation shows that the ion effectively acts as a series circuit with capacity C_{ion} and inductance L_{ion}. It is noteworthy, that these values would be very uncommen in electronics, for example for a deuteron in our trap these values evaluate to $L_{\mathrm{ion}} \approx 10^7\,\mathrm{H}$ and $C_{\mathrm{ion}} \approx 10^{-20}\,\mathrm{F}$. The impedance of such a series circuit is

$$\begin{aligned} Z_{\mathrm{ion}} &= i\omega L_{\mathrm{ion}} - \frac{i}{\omega C_{\mathrm{ion}}} \\ &= i\omega R_p \tilde{\tau} \left(1 - \frac{\omega_z^2}{\omega^2}\right). \end{aligned} \tag{2.54}$$

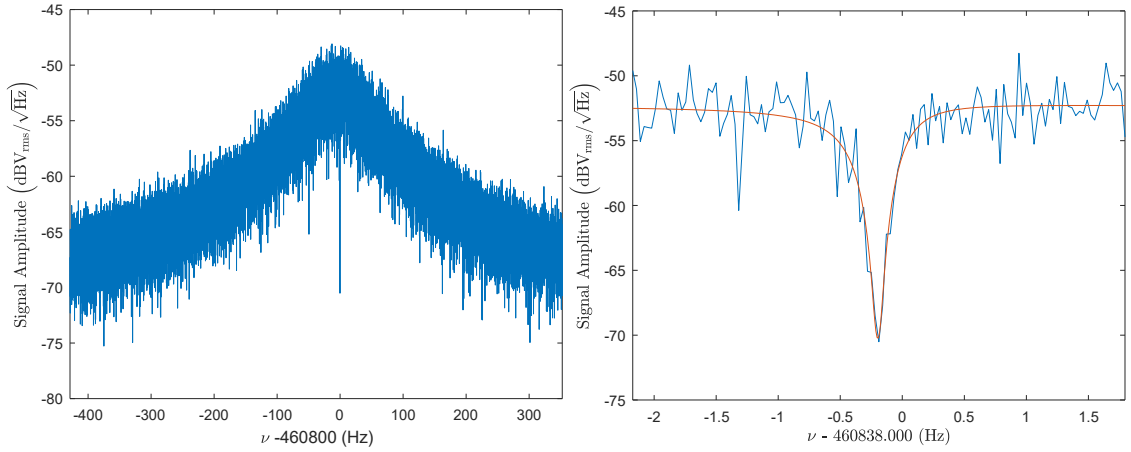

(a) Resonator spectrum with dip (b) Zoom into dip

Figure 2.4: Dipsignal of a single deuteron. In (a), the plotted frequency range is wider than the width of the resonator, the Johnson noise of the resonator is clearly visible. The zoomed in spectrum in (b) shows the dip in detail, together with a fitted lineshape. The resonator appears flat on this scale. The y-axis is scaled to $\mathrm{dbV_{rms}}/\sqrt{\mathrm{Hz}}$, which removes the dependency of the frequency resolution $\Delta\nu$.

We can use this, to calculate the total impedance of the system of ion and resonator, and then get the lineshape in the same way we got the lineshape for the resonator only outlined in section 2.2.3. The total impedance is

$$\begin{aligned} Z_{\mathrm{tot}} &= \frac{1}{\frac{1}{Z_{\mathrm{LC}}} + \frac{1}{Z_{\mathrm{ion}}}} \\ &= R_p \frac{\omega_{\mathrm{res}}\omega\left(\omega^2 - \omega_z^2\right)}{\omega_{\mathrm{res}}\omega\left(\omega^2 - \omega_z^2\right) + iQ\left(\omega^2 - \omega_{\mathrm{res}}^2\right)\left(\omega^2 - \omega_z^2\right) - i\omega_{\mathrm{res}}\omega^2/\tilde{\tau}}, \end{aligned}$$

with the real part

$$\mathrm{Re}(Z_{\mathrm{tot}}) = R_p \frac{\left(\omega_{\mathrm{res}}\omega\left(\omega^2 - \omega_z^2\right)\right)^2}{\left(\omega_{\mathrm{res}}\omega\left(\omega^2 - \omega_z^2\right)\right)^2 + \left(Q\left(\omega^2 - \omega_{\mathrm{res}}^2\right)\left(\omega^2 - \omega_z^2\right) - \omega_{\mathrm{res}}\omega^2/\tilde{\tau}\right)^2}. \quad (2.55)$$

The resulting noise density is calculated from equation (2.42). After transforming into logarithmic units and considering the same effects as in section 2.2.3, the lineshape reads

$$20\log_{10} u_n^{\mathrm{dip,FFT}} = 10\log_{10}\left[\tilde{A}\,\mathrm{Re}(Z_{\mathrm{tot}})/R_P + (\tilde{u}_n^{\mathrm{ampl}})^2\right] + \tilde{\kappa}_{\mathrm{det}}(\omega - \omega_{\mathrm{res}}). \quad (2.56)$$

This lineshape is typically referred to as a *dip*. At the ion's axial frequency, the ion effectively shortens the thermal noise of the resonator, resulting in a dip in the noise spectrum. One example for such a dip signal is shown in figure 2.4
When having multiple ions of the same species in the trap, above analysis holds for the common motion, but the dip signal is widened. For N ions, the -3dB width of the dip $\Delta\nu_z$ is

$$\Delta\nu_z = \frac{N}{2\pi}\frac{1}{\tau}. \quad (2.57)$$

From this, one can verify that there indeed is a single ion in the trap.
In this model, the dip always reaches to the noise floor given by the amplifier. However, in practice this is not always the case due to instabilities in the axial frequency. To factor such instabilities in, the lineshape in equation (2.56) can be convoluted with a Gaussian distribution for the axial frequency ω_z, resulting in a slightly wider and less deep dip signal.

2.3 Excitations

In a Penning trap, several kinds of excitations are used to manipulate the motion of the ions. These excitations are driven by applying an AC-voltage to an electrode or to a split electrode. Since the motional frequencies are in the order of $< 30\,\mathrm{MHz}$, the corresponding wavelengths are much larger than the dimensions of the trap. Therefore, it suffices to threat these excitations quasi static in a near field approximation.

2.3.1 Dipolar Excitation

The dipole excitation is used to directly and coherently excite one motional mode. For the axial mode, the field component which is associated with a dipole excitation is given by a potential

$$\Phi \propto U_{\mathrm{exc}} \sin(\omega_{\mathrm{rf}} t + \phi_0) z, \tag{2.58}$$

where ω_{rf} is the frequency of the excitation and ϕ_0 an arbitrary phase. The voltage used for the excitation is denoted as U_{exc}. Such an oscillating potential can be achieved by applying the oscillating voltage to any off-center electrode. Adding the force resulting from such a field to the equation of motion (2.5c) results in a driven harmonic oscillator. Usually, this excitation is applied for a short time T and $\omega_{\mathrm{rf}} \approx \omega_z$. This results in an amplitude depends linearly on the excitation time. However, the initial phase relation between the ion and the excitation plays a role. If the amplitude before the dipole excitation was z_0, the amplitude z_{exc} after excitation is [54]

$$z_{\mathrm{exc}}^2 = (\kappa_z T U_{\mathrm{exc}})^2 + z_0^2 + (2\kappa_z T U_{\mathrm{exc}} z_0 \cos(\Delta\phi)). \tag{2.59}$$

Here, κ_z is a constant which has to be calibrated, and $\Delta\phi$ is the phase difference between the excitation and the inital phase of the ion. Usually, this phase difference is random. Note, that this is only true for excitations, where $\omega_{\mathrm{rf}} - \omega_z \ll 1/T$. Otherwise the excitation strength decreases with $\frac{\sin(\omega_{\mathrm{rf}} - \omega_z)}{\omega_{\mathrm{rf}} - \omega_z}$, and even has minima at $\omega_{\mathrm{rf}} - \omega_z = \pm\frac{2\pi N}{T}$, with $N \in \mathbb{N}$.
These results also hold for the radial modes. There, one has to use a potential $\Phi \propto x$ or $\Phi \propto y$. At LIONTRAP, this is done by applying the oscillating voltage to one half of a split electrode.

2.3.2 Quadrupolar Excitation

The quadrupolar excitation is used to couple the motional modes. Coupling between both radial modes can be achieved by using a potential $\Phi \propto xy$. To effectively generate such a potential, one can again use a split electrode. However, the mirror symmetry of a half-split electrode does not allow this excitation. For example, one can use an electrode which is split in a way that the voltage can be applied to one quarter of the electrode. Such an electrode is not available at LIONTRAP at the moment.
To couple one radial mode with an axial mode, one needs a potential $\Phi \propto xz$ (or yz), which can be achieved by using an off-center electrode, which is split in half. For now I focus on coupling between the modified cyclotron motion and the axial motion. There are two important cases to be distinguished:

1. A coupling with frequency $\omega_{\mathrm{rf}} \approx \omega_+ - \omega_z$ leads to a coherent exchange of energy between the modes. This can be used for the coherent measurement technique PnP (see also section 2.6), and also in the incoherent detection technique called *double dip* (see also section 2.5).

2. When coupling with frequency $\omega_{\mathrm{rf}} \approx \omega_+ + \omega_z$, this results in an amplification of both modes. Simply put, the amplitude in one mode determines the drive strength in the other mode. This is used in the coherent measurement technique PnA, which is discussed in section 2.6.

Coupling the magnetron motion to the axial motion works in the same way. However, the exchange of energy occurs at the coupling frequency $\omega_{\mathrm{rf}} \approx \omega_z + \omega_-$, which is a non-trivial consequence from the fact that the energy associated with the magnetron motion is negative. It is important to note, that the field generated by an off-center split electrode is of course not a pure quadrupolar field. Especially dipole excitations of both radial and axial modes are also possible. In fact, the same electrode is used for both quadrupolar and dipolar excitation through a wide range of measurements performed at LIONTRAP.

2.3.3 Electronic Feedback

Electronic Feedback is a form of excitation, which is not applied directly to the ion, but to a resonator as introduced in section 2.2.2. The Johnson noise of the resonator is amplified, phase shifted and fed back capacitively to the resonator. Without going too much into details, which are extensively described in [52, 54], there are three cases to be distinguished, depending on the phase:

1. So called *90 degree feedback*, where the phase is $\pm 90°$, shifts the apparent resonance frequency of the resonator. This form of feedback is currently not used at LIONTRAP.

2. At a phase shift of $0°$, the Q-value and the effective temperature of the resonator increase. This is called *positive feedback*. Positive feedback is currently also not used at LIONTRAP.

3. For a phase shift of 180°, *negative feedback* occurs. The Q-value of the resonator decreases, together with the effective temperature of the resonator. This is used routinely at LIONTRAP to decrease the temperature of the ions below the environment temperature of about 4.2 K.

2.4 Temperatures

Usually, *temperature* describes the distribution of energies for a sample of particles. So what is meant by the temperature of a single ion? If there is a damping mechanism, for example through a tank circuit as described in section 2.2.4, after a few cooling time constants τ, the ion can be considered in thermal equilibrium with the tank circuit. If one measures the ion's energy, then waits for a few cooling time constants and repeats this process several times, the resulting energy distribution will be the one expected from the temperature of the tank circuit.
In principle, this is an application of the ergodic hypothesis: The temperature is not measured as an average over an ensemble, but as a time average over a single particle in thermal equilibrium with that ensemble. For an ion in thermal equilibrium with a tank circuit, the ensemble would be the combination of the electron gas in the tank circuit and the ion in the Penning trap.
At LIONTRAP, typically the axial motion is in thermal equilibrium with a tank circuit. The temperature of the circuit is at the environmental temperature of $T = 4.2\,\mathrm{K}$, or slightly lower by means of electronic feedback. The average axial energy is then

$$\begin{aligned} < E_z > &= k_B T \\ &=: k_B T_z, \end{aligned} \tag{2.60}$$

where T_z is defined as the *axial temperature*. Comparing this with the quantum mechanical expression for the axial energy in equation (2.16), one sees that the mean quantum number is $\langle n \rangle \approx 2 \cdot 10^5$, justifying a classical treatment. At LIONTRAP, we cool the radial modes by coupling them to the axial mode using the resonant exchange of energy described in section 2.3.2. This results in equal quantum numbers [54]. The temperatures are then given by the axial temperature times the frequency ratio,

$$T_+ = \frac{\omega_+}{\omega_z} T_z =: < E_+ > \tag{2.61a}$$

$$T_- = -\frac{\omega_-}{\omega_z} T_z =: < E_- > . \tag{2.61b}$$

If the axial temperatures during the coupling of magnetron and cyclotron motion were equal, this means especially, that the modified cyclotron radius r_+ and the magnetron radius r_- are equally distributed, see equation (2.15). I define the temperature of the magnetron motion as negative, $T_- < 0$. Since the energy associated with the magnetron motion is also negative, this allows the Boltzmann factor to be written in the usual manner, $\exp(\frac{E_-}{k_b T_-})$. However, this should not be

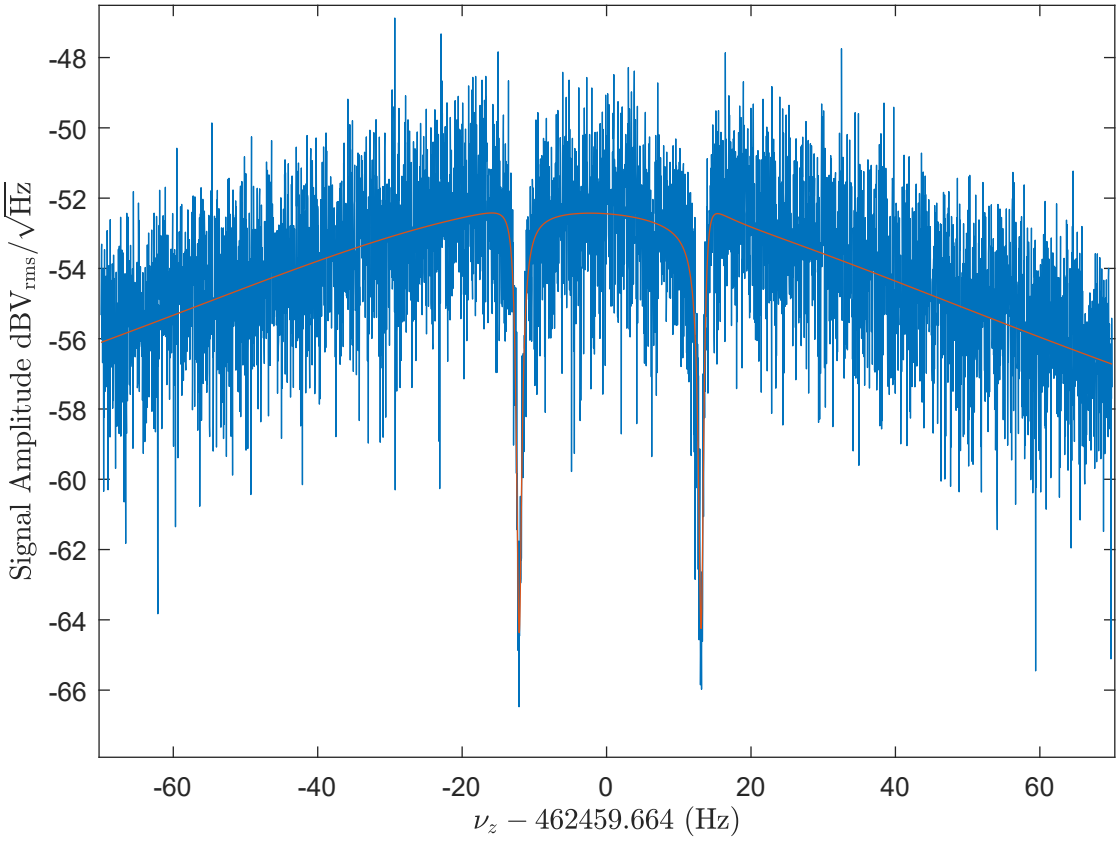

Figure 2.5: Example of a double dip of a single deuteron (blue), together with a fitted lineshape model (red). The signal amplitude as function of the frequency is shown.

confused with other mentions of negative temperature in the literature [55], where the term negative energy describes a situation where the probability for a given kinetic energy is higher for higher energies, up to a cut-off energy.

2.5 Incoherent Detection Techniques

At LIONTRAP, two incoherent detection techniques are used: The dip as described in section 2.2.4 and the double dip already mentioned in section 2.3.2. Here I describe the technique of the double dip in more detail. The basic idea of this technique was found by later Nobel laureate Eric Cornell [56] in 1990, however, there he was looking at a double peak signal, not a double dip.
As previously mentioned, the coupling drive with frequency $\omega_{rf} \approx \omega_+ - \omega_z$ leads to a coherent exchange of energy between the axial and the modified cyclotron mode. This can be seen as analogous to a driven quantum mechanical two level system. The cyclotron mode and the axial mode correspond to the excited and ground state, the energy in the modes corresponds to the probability of the states. The corresponding Hamiltonian can be diagonalized and the eigenvalues can be

identified, see for example [57].
In the laboratory frame, the axial frequencies of the dressed system are

$$\omega_{r,l} = \omega_z - \frac{\delta}{2} \pm \frac{1}{2}\sqrt{\delta^2 + \Omega^2}, \tag{2.62}$$

often denoted with indices l and r for left and right. Here, δ is the detuning of the radio-frequency drive, defined as

$$\delta = \omega_{\mathrm{rf}} - (\omega_+ - \omega_z)\,. \tag{2.63}$$

The coupling strength is described through the Rabi-frequency Ω. The dip splits into two dips with frequencies given by equation (2.62). From a fit to this lineshape, the axial frequency typically measured beforehand using the dip technique and the known coupling frequency, one can deduce the modified cyclotron frequency using

$$\omega_+ = \omega_{\mathrm{rf}} + \omega_l + \omega_r - \omega_z. \tag{2.64}$$

For small detunings $\delta \approx 0$, the left and right dip are symmetrical with respect to the position of the dip without coupling, and they are split by the Rabi-frequency Ω. This allows a calibration of the strength of the quadrupolar excitation and a cross-check with the excitation strength expected from the technical setup, by using [56]

$$\Omega = \frac{qE_0}{2m\sqrt{\omega_z\omega_+}}, \tag{2.65}$$

where E_0 is the electric field used for the excitation $\vec{E} = E_0 \cos(\omega_{\mathrm{rf}} t)\,(x\hat{z} + z\hat{x})$. This field can be related to the applied voltage by a simulation of the trap geometry. An example for such a double-dip measurement with a Rabi-frequency of about $\Omega = 2\pi \cdot 25\,\mathrm{Hz}$ and a fitted lineshape is shown in figure 2.5. The lineshape is very similar to the dip lineshape derived in section 2.2.4, for more details see e.g. [58]. The width of these dips can also be derived from the quantum mechanical analogy [41]. The amplitudes of the states are given in terms of a mixing angle θ, which fulfills

$$\tan(2\theta) = -\frac{\Omega}{\delta}. \tag{2.66}$$

The width of the left and right dip, expressed as a time constant in the same manner as the dip, can then be evaluated to

$$\begin{aligned} \tau_l &= \frac{\tau}{\sin(\theta)} \\ \tau_r &= \frac{\tau}{\cos(\theta)}, \end{aligned} \tag{2.67}$$

with

$$\begin{aligned} \sin(\theta) &= \frac{1}{2}\left(1 + \frac{\delta}{\sqrt{\Omega^2 + \delta^2}}\right) \\ \cos(\theta) &= \frac{1}{2}\left(1 - \frac{\delta}{\sqrt{\Omega^2 + \delta^2}}\right). \end{aligned} \tag{2.68}$$

The same principle can be transferred to a measurement of the magnetron frequency ω_-. However, a few subtleties have to be considered. There, one needs to use the other sideband $\omega_{\mathrm{rf}} \approx \omega_z + \omega_-$ because of the negative energy associated with the magnetron motion. Therefore, the magnetron frequency needs to be extracted using

$$\omega_- = \omega_{\mathrm{rf}} - \omega_l - \omega_r + \omega_z. \tag{2.69}$$

For typical frequencies, the drive frequency is relatively close to axial frequency, resulting in three complications. First of all, the dipolar portion of the driving field will drive the axial motion directly, giving effectively an increased temperature. Secondly, the excitation can saturate the amplifiers, and thirdly, the excitation can introduce noise to the resonator. Therefore, one typically needs to take several double dip spectra with decreasing coupling strength and to extrapolate the resulting magnetron frequency to zero coupling strength.
The double-dip method has been used for a variety of great results in different groups using Penning traps, for example the proton/antiproton charge-to-mass comparison [59], the proton/antiproton g-factor measurements [60, 61] and various g-factor measurements on highly-charged ions [58, 62]. One major advantage is, that as the ion is in thermal equilibrium during the measurement, one has to deal with low energy dependent systematic shifts. However, especially when trying to compare ions with different charges and masses, the understanding of the lineshape model becomes a critical and potentially limiting factor. This is one reason for using coherent detection techniques as described in the next section.

2.6 Coherent Detection Techniques

The principle of coherent detection techniques is to measure a phase, rather than just the frequency. This can be done with any of the motional modes. For mass measurements, the measurement of the modified cyclotron frequency is of the highest importance. Therefore, I focus on the phase-sensitive measurement techniques of this mode in this section.
All phase-sensitive techniques follow the following steps:

1. Imprint a starting phase to the ion's motion. Usually this is done by a dipolar excitation.

2. Wait a well-defined time period, called *evolution time* T_{evol}.

3. Read out the phase of the ion. Here the techniques differ.

For very high-excitation radii the phase could in principle be read-out directly using a cyclotron resistor. However, the systematic uncertainties associated with such a high excitation make this approach unfeasible for the level of precision we are aiming at.
Another approach is to transfer the phase to the modified cyclotron amplitude by a second dipolar pulse and read out the amplitude by deliberately introducing

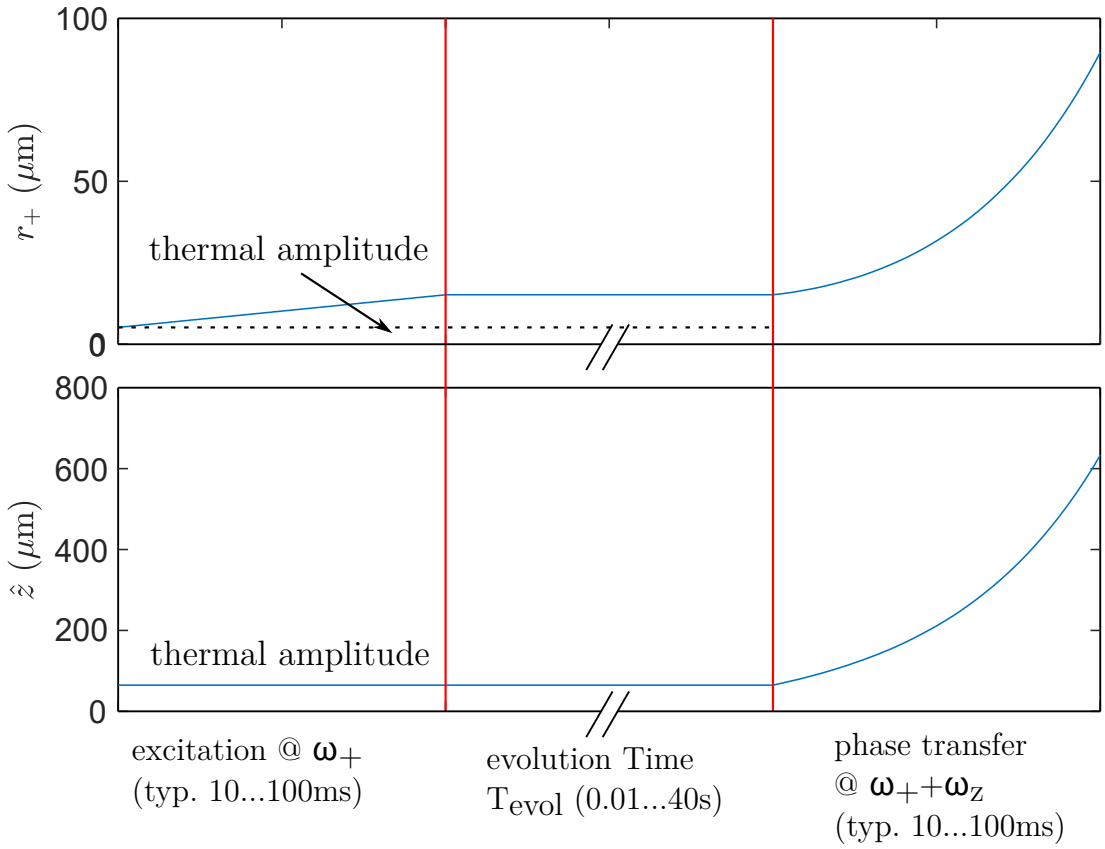

Figure 2.6: Principle of the PnA technique. The modified cyclotron mode is excited slightly above its thermal amplitude by a diploar excitation at frequency $\omega \approx \omega_+$. The phase evolves freely for a phase evolution time T_{evol}, which varies between 10 ms to 40 sec. The phase of the cyclotron mode is transferred to the axial mode by a pulse at $\omega \approx \omega_+ + \omega_z$, which also amplifies both the cyclotron mode as well as the axial mode.

anharmonicities. This approach has been used for the magnetron frequency at LIONTRAP [63]. However, for the cyclotron mode one would need relatively large amplitudes, making this method less suited.

The approach used at LIONTRAP is to transfer the phase of the cyclotron mode to the phase of the axial mode. This idea was first realized in the group of David E. Pritchard at the Massachusetts Institute of Technology (MIT). There, they used a π-pulse with frequency $\omega_{\text{rf}} \approx \omega_+ - \omega_z$ to coherently transfer the energy and the phase of the cyclotron mode to the axial mode. This technique is called PnP for *Pulse aNd Phase* [56].

In our group, this approach was slightly altered by using a parametric amplification with frequency $\omega_{\text{rf}} \approx \omega_+ + \omega_z$ instead of the π-pulse. This technique is called PnA for Pulse and Amplify [64]. Such an amplification can also transfer the phase of the modified cyclotron motion to the axial motion, if the following condition is

fulfilled:

$$\begin{aligned} \gamma r_{+,0} &\gg z_0, \\ \gamma &= \sqrt{\frac{\omega_+ - \omega_-}{\omega_z}} \approx \sqrt{\frac{\omega_+}{\omega_z}}. \end{aligned} \tag{2.70}$$

Here, $r_{+,0}$ and z_0 denote the motional amplitudes of the modified cyclotron and axial mode before parametric amplification, respectively. Note, that the factor γ matches the factor between the thermal radii of an ion, whose modified cyclotron mode has been thermalized by coupling it to the axial mode. In this case, the condition in equation (2.70) is automatically fulfilled as long as one excites significantly above the thermal radius, which one in any case needs to do in order to reliably imprint a phase. The principle of this technique is sketched in figure 2.6. This method has the big advantage, that the amplitude of the axial signal, where the phase is read-out, is adjustable independently from the dipolar excitation amplitude which imprints the phase. This allows to vary the excitation amplitudes to a much higher degree than in the PnP method, extending the range accessible to account for the dipolar excitation amplitude as a source of systematic shifts.

2.7 Additional Systematic Shifts

In this section, I introduce various further systematic shifts which also play an important role for precision measurements in Penning traps. These are relativistic shifts, the image charge shift and polarization shifts.

2.7.1 Relativistic Shifts

The ion's motion leads to a relativistic mass increase, which influences the motional frequencies. For LIONTRAP, this is especially important, as the lighter the ions are, the bigger are these shifts. While a detailed analysis on the relativistic frequency shift can be found in [65] it turns out, that only the energy in the modified cyclotron motion plays a role.
Neglecting the energy in the axial and magnetron modes, the modified cyclotron frequency shifts as

$$\begin{aligned} \frac{\Delta\omega_+}{\omega_+} &= -\frac{\omega_+^2 E_+}{mc^2(\omega_+ - \omega_-)^2} \\ &\approx -\frac{E_+}{mc^2} \\ &= -\frac{\omega_+^2 r_+^2}{2c^2}. \end{aligned} \tag{2.71}$$

The shifts of the other modes can be neglected. The energy of deuteron at a modified cyclotron radius of $r_+ = 100\,\mu\text{m}$, the highest excitation radius used during the deuteron measurement campaign, is about $E_+ \approx 3.4\,\text{eV}$. This is to be compared with the rest mass, which is $m_d c^2 \approx 1.9\,\text{GeV}$. In this scenario, the shift is in

the range of $1.9 \cdot 10^{-9}$ and thus very relevant. How this is treated in the mass measurement is shown in section 5.3.1. In section 4.3.2, this shift is used to calibrate the excitation strength in the modified cyclotron mode.

2.7.2 Image Charge Shift

In section 2.2, I described how the image charges the ion induces in the trap surfaces can be used to detect its axial frequency. However, there is also a quasi-static effect related to these image charges. In our cylindrical traps, this effect occurs mostly in the radial direction. An ion on its radial motion induces image charges in the surfaces, which create an outward electrical force. This effectively lowers the modified cyclotron frequency and increases the magnetron frequency by the same amount.
For measurements utilizing the $\omega_c = \omega_+ + \omega_-$ to deduce the free space cyclotron frequency, this effect hence does not play a role. When using the invariance theorem however, one needs to correct for this effect. This can be done by simulations of the trap geometry. Such simulations have been performed for our setup and checked to a relative precision of 5% with measurements of the magnetron frequency difference of a proton and a $^{12}C^{6+}$ ion as reported in [63]. Since this effect scales with the number of ions in the trap, this gives another method of measuring it. This was done in [66].
While for the analyses done in this work I used the value $\Delta\nu_c = -475.4\,\mathrm{Hz}\,e^{-1}$, it is still instructive to see how this scales with the involved quantities. Generally speaking, the relative shift of the cyclotron motion scales as

$$\frac{\Delta\omega_c}{\omega_c} \approx -1.95\frac{m}{8\pi\epsilon_0 r^3 B_0^2}, \tag{2.72}$$

where r is the trap radius. A bigger trap thus reduces this shift, but it also reduces the signal for image current detection, making measurements more difficult. For the electron mass measurement performed at the predecessor of LIONTRAP, this image charge shift was the leading systematic uncertainty at 14 ppt. To reach the 10^{-12} range we decided at LIONTRAP to increase the trap radius from $r_{\mathrm{old}} = 3.5\,\mathrm{mm}$ to $r_{\mathrm{new}} = 5\,\mathrm{mm}$. This pushes the uncertainty of the image charge shift to about $5 \cdot 10^{-12}$, while still giving enough signal strength even for the lightest ions as the proton, the deuteron and the HD^+ molecular ion.

2.7.3 Polarization Shift

The polarization shift in a Penning trap was first observed in the MIT group [67]. This effect occurs when measuring the cyclotron frequency of a particle with a significant polarizability, like a molecular ion. The motional electric field induces an electric dipole pointing towards the trap center of the cyclotron motion. This dipole has an energy in the motional electric field, which leads to an effective mass

increase, but only in the radial direction. This shift can be calculated to

$$\frac{\Delta\omega_c}{\omega_c} = -\alpha_{\mathrm{pol}}\frac{B_0^2}{m}, \tag{2.73}$$

where α_{pol} is the polarizability of the electronic state of the (molecular) ion of interest [68]. Since the polarizability is often given in atomic units and the mass in atomic mass units, equation (2.73) can be rewritten to

$$\frac{\Delta\omega_c}{\omega_c} = -9.929 \cdot 10^{-15}\alpha_{\mathrm{pol}}/[a.u.]\frac{(B_0/[T])^2}{m/[u]}. \tag{2.74}$$

For the HD^+ molecular ion used in this work, the ground-state polarizability is $\alpha_{\mathrm{pol}} = 395.30\,a.u.$ [69], leading to a shift of $\Delta\omega_c/\omega_c = -1.84 \cdot 10^{-11}$ compared to a hypothetical particle with the same charge and mass, but no polarizability, making it a relevant shift. Since α_{pol} is calculated with sufficient precision, this effect can be corrected for on a level which is much better than our current level of precision.

3 The LIONTRAP-Setup

In this chapter, I describe the LIONTRAP-setup. Parts of the setup are based on the former g-factor experiment on highly-charged ions located in Mainz [70, 52, 54]. There, the setup was continuously improved, resulting in a range of excellent results. The g-factor measurements demanded heavier and more highly charged ions, which were increasingly difficult to provide in the relatively small setup in Mainz. Therefore, it was decided to shift focus to mass measurements. To achieve this, large parts of the setup were replaced in 2016 prior to the first mass measurement campaign on the proton's atomic mass [8, 7]. A brief overview of the setup and a detailed description of further improvements carried out in the framework of this thesis are given in the following.

3.1 Overview

An overview of the experiment is shown in figure 3.1. The heart of the experiment is a stack of Penning-trap electrodes. These electrodes make up in total five traps. These are two storage traps ST1 and ST2, the precision trap PT, in which the mass measurements are performed, a trap which is intended to monitor the magnetic field called magnetometer trap MT, and a trap used for the production of ions called creation trap CT. I give more details on the traps in section 3.4. The traps are located in a so-called *trap chamber*. This is a vacuum vessel, which is pumped to $\approx 10^{-7}$ mbar and hermetically sealed at room temperature. In the experiment, the trap chamber is at a temperature of 4.2 K, lowering the pressure to $< 10^{-17}$ mbar, measurable only by the lack of charge exchange losses.
Located above the trap chamber is a cryogenic electronics section. The cryogenic amplifiers are located here, as well as filter boards for DC voltages and switches for excitations. These parts are cryocooled to liquid helium temperature by a LHe tank. The transition to the room temperature region works through the helium filling tube. There, a so-called *20K-shield* cooled by the boil-off helium gas is attached, wich covers the lower part of the setup against thermal radiation. This shield is designed to be at 20 K, however, it turned out to be at a much lower temperature only slightly above liquid helium temperature.
On top of all of this, there is a so-called *hat*, consisting of further electronics and the necessary electronic feedthroughs.
This central part of the setup is lowered into the bore of a 3.8 T superconducting magnet, with a maximum field strength of 6 T. The magnet bore and the hat build a vacuum vessel for an isolation vacuum. Our magnet was charged in 1995 and since then the current is untouched.

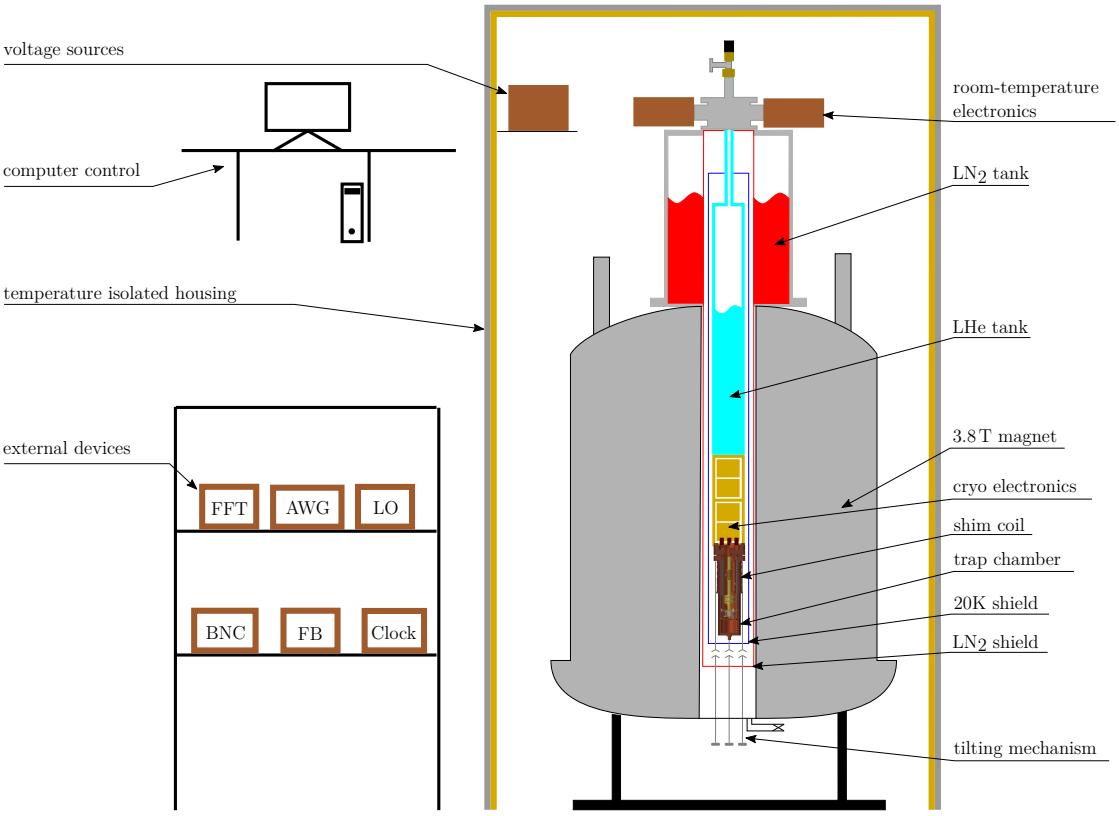

Figure 3.1: Overview of the setup. The setup consists of an elongated central part, which is lowered into the warm bore of a 3.8 T magnet. Several external devices produce the voltages and signals necessary to operate the experiment. They are remotely controlled by a computer with a labview control system. For details see text.

Already implemented in the warm bore is a liquid nitrogen shield, which is connected to a liquid nitrogen tank on top of the magnet. Its thermal connection to the setup happens at the helium filling tube, above the connection of the 20K-shield. Further details on the cryosetup can be found in [71]. The magnet is housed in a thermally insulated box. The box is temperature stabilized to a temperature a few degrees above room temperature, for the deuteron measurement campaign at 30 °C. Fans produce a constant airflow, reducing temperature gradients.

The voltage sources are also located in the temperature stabilized region. For the trap voltages, we use two UM1-14 voltage sources by Stahl-Electronics. Other voltages, for example for the biasing of the cryo-amplifiers, are provided by self-built voltage sources.

Outside of the temperature stabilized region, there is a rack with a multitude of external devices. These devices are:

- AWG. An arbitrary waveform generator, to produce arbitrary excitations, connected to a quadrupolar excitation line.

- FFT. An SR1 audio analyzer by Stanford Research, which is providing a fast Fourier transformation of the ion signals.
- LO. A function generator which we call *local oscillator*. It is used to mix down the axial frequency signals ($\approx 500\,\mathrm{kHz}$) into the audio region ($\approx 15\,\mathrm{kHz}$).
- BNC. A pulse generator BNC555 from Berkeley Nucleonics used to trigger time-critical measurements.
- FB. Another function generator used for the application of electronic feedback.
- Clock. A 10 MHz rubidium frequency standard FS725 by Stanford Research Systems. All devices are locked to this frequency standard.
- For specific situations, several other devices where used. For example additional function generators for dipolar excitations or a spectrum analyzer to take wide range mass spectra during ion production.

All external devices are controlled from a computer, on which control programs written in labview are executed.

3.2 Pressure Stabilization

The boiling temperature of liquid helium and liquid nitrogen is pressure dependent. Temperature changes can influence the magnetic field and thus our measurement, since the magnetic susceptibility of all materials is temperature dependend. The materials used in our setup have been chosen to have as little as possible susceptibility, however, some susceptibility, which then also depends on the temperature, remains.
In the past, the temperature in the range around the boil-off point of liquid helium was even defined by its pressure dependency. While this *International Temperature Scale of 1990 ITS-90* [72] has officially been replaced in the context of the new SI [73], the scale still provides a convenient way to measure the temperature around 4 K. In the atmospheric pressure range, the scale can be linearly approximated. The temperature T as a function of the pressure P then reads

$$T = 4.20814\,\mathrm{K} + 1.06\,(P - 1000\,\mathrm{mbar})\,\mathrm{mK\,mbar^{-1}}. \tag{3.1}$$

Without further measures, the pressure in the LN_2 tank follows the ambient pressure. The LHe tank is connected to a recovery line. There, the helium is collected in a ballon to be re-liquified. The pressure in this recovery line is usually slightly above ambient pressure. However, situations like filling of other experiments also connected to the recovery line or work at the liquifier can lead to significant pressure fluctuations.
The ambient pressure can vary significantly in the range of $\approx 980\,\mathrm{mbar}$ to $\approx 1030\,\mathrm{mbar}$, resulting in temperature changes of up to $\approx 50\,\mathrm{mK}$. While this does not

seem like a lot, significant effects on the motional frequencies have been observed in the past [54].

At LIONTRAP, there is an additional complication, since the experiment is mechanically supported only by the helium filling tube. This tube is at room temperature at the top of the experiment, and at 4 K when it enters the helium tank. The temperature profile along the tube is largely determined by the boil-off rate of liquid helium, which mostly reacts to pressure changes. Therefore, changes in the boil-off rate will lead to the tube expanding or contracting, effectively changing the position of the trap in the magnet.

All these considerations in mind, we decided to implement a pressure stabilization for our cryo reservoirs. Here, I present the setup, its effect on the ions is evaluated in section 4.6.

3.2.1 Design Requirements

When evaluating, how stable the pressure actually has to be, the dependency of the modified cyclotron frequency ν_+ on the pressure is the quantity of interest. In [54], this quantity has been measured for all four reservoirs of the predecessor experiment of LIONTRAP. There, the measured coefficients were between $\approx 4\,\mathrm{ppb/mbar}$ and $< 40\,\mathrm{ppt/mbar}$. For the deuteron campaign, we were aiming at a statistical precision better than 10 ppt. In order to not significantly contribute to the statistical uncertainty, the pressure thus needs to be stable in the range of a few µbar, assuming that these coefficients are in the same order of magnitude despite significant changes in the setup.

One should note, that this is absolute pressure, and measuring an absolute pressure to a relative precision of 10^{-6} is challenging. At other experiments this problem was tackled by building a pressure reference cell and measuring the pressure difference [74, 75, 20]. However, this translates the difficulty in measuring absolute pressure to a difficulty in keeping the pressure in the reference cell stable. Therefore, we decided to use absolute pressure sensors and stabilize to a pressure slightly above ambient pressure, usually 1050 mbar.

The pressure should be regulated by regulating the flow through a controlled valve. At LIONTRAP, we have a LHe consumption of about 900 sccm (standard cubic centimeters) for the apparatus and about 750 sccm for the magnet. For LN_2, we have about 3200 sccm for the apparatus and 2500 sccm for the magnet. We decided to connect the exhausts of apparatus and magnet and stabilize these together, so that in total only two instead of four stabilization systems will be needed. The controlled valve thus needs to be able to effectively regulate a flow of 1650 sccm (LHe) or 5700 sccm (LN_2) with a pressure difference between 30 to 70 mbar at about 1000 mbar absolute pressure.

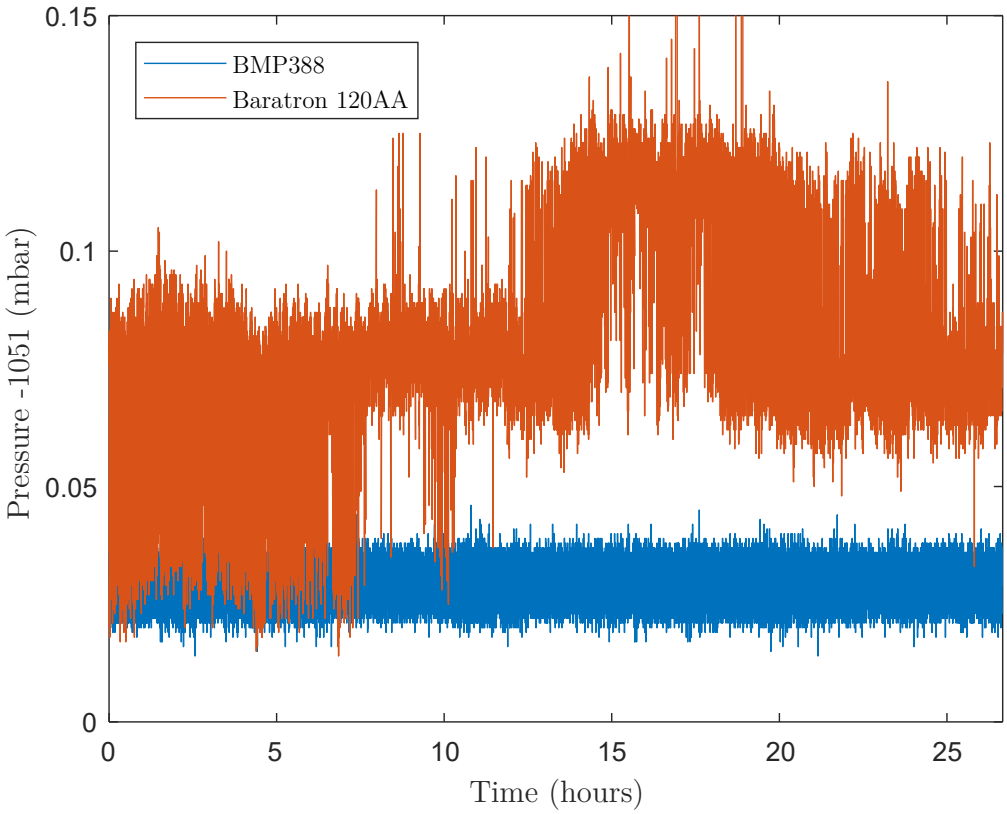

Figure 3.2: Pressure sensor comparison BMP388/Baratron 120AA. Shown is a comparison between the sensors BMP388 and the Baratron 120AA, while both sensors are connected to the LHe reservoir stabilized with the BMP388. The Baratron 120AA shows digital steps corresponding to 40 µbar. On a time scale of several hours, drifts between sensors are on the order of one digital step of the Baratron and thus on an acceptable level.

3.2.2 Pressure Sensors and Regulated Valves

The first attempts were done using the pressure sensor Baratron 120AA by MKS Instruments. This sensor has a pressure range of 1 torr $\approx$ 1.33 mbar and is specified to have an accuracy of 0.12 % and a resolution of $1 \cdot 10^{-6}$. The pressure is indicated by an analog voltage. However, while comparing with a second pressure sensor we noticed that the voltage shows digital steps corresponding to pressure changes of about 40 µbar, making regulations below this threshold impossible, see figure 3.2. The second pressure sensor we used is the BMP388 by Bosch Sensortec. This sensor is usually meant to be used as a pressure altimeter in drones, and is as a mass product very cheap. We used the version supplied by *adafruit*, which includes a board containing electronics for digital communication and only costs about 10 €. To use the BMP388 at our experiment, we needed to enclose it in a vacuum vessel with the necessary feedthroughs. The read-out is done by an Arduino controller. At the highest resolution setting, this pressure sensor has a specified resolution of 85 µbar and a specified absolute accuracy of only 50 mbar. However, the absolute

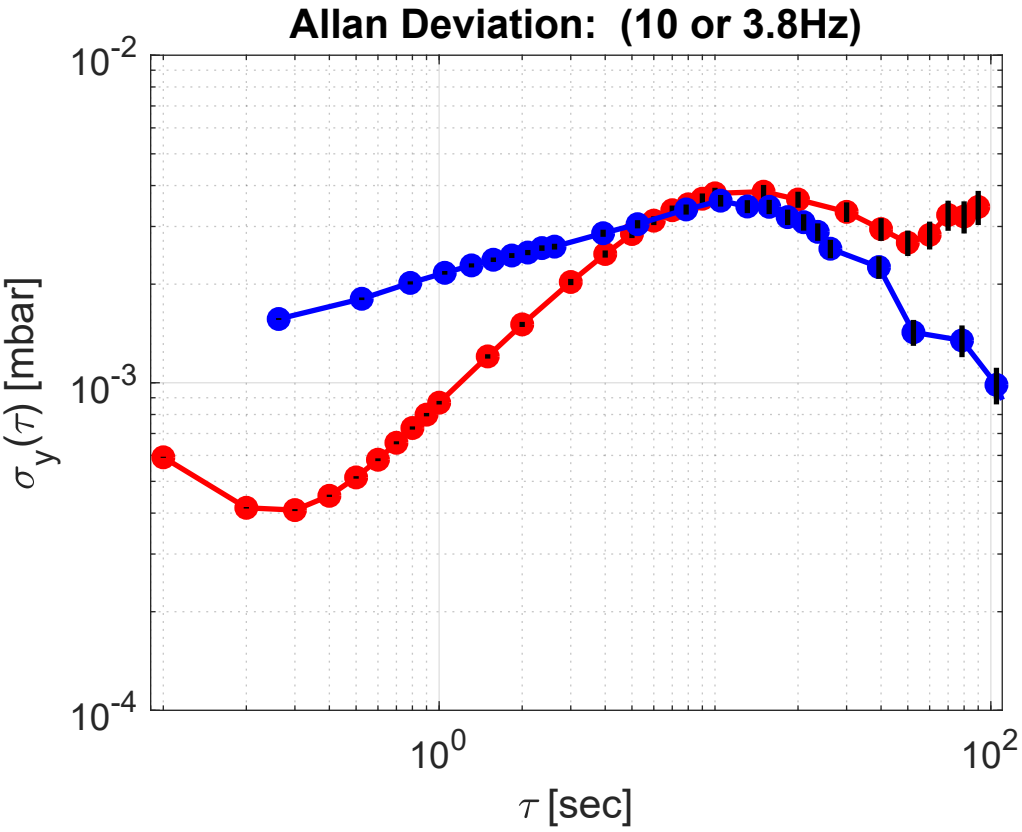

Figure 3.3: Pressure sensor comparison BMP388/6000-23A. Allan Deviation Plot of the pressure read-out by the BMP388 (blue) and the 6000-23A (red). Both sensors were connected to the stabilized LHe reservoir, the stabilization was using the BMP388 as sensor. On timescales above a few seconds, the regulated sensor's allan deviation has a maximum of about 4 µbar. The 6000-23A confirmes this value. On shorter timescales, the passive stability of the reservoir becomes significant. One longer timescales, the comparison of both sensors confirms that the drift between sensors is below 10 µbar for 100 s.

accuracy is not very important for a pressure regulation and can be improved easily by a calibration measurement. The resolution performed much better than specified and at least better than 4 µbar as one can see from figure 3.3. Giving an exact number is hard however, since one would need a reservoir which is more stable than the resolution of the sensor, which was not available. A possible problem would be a drift of the sensor with time. To check for this we performed a measurement where the Baratron 120AA and the BMP388 were connected to the same stabilized pressure reservoir. On the time scale of three days, drifts could be excluded up to the level of one digital step of the Baratron. The high resolution, the absence of drifts on relevant time scales, the easy digital read-out and the low cost make the BMP388 a good choice for a pressure stabilization sensor.
For the LHe stabilzation we additionally bought a 6000-23A pressure sensor by Paroscientific. This pressure sensor has a specified accuracy of 80 µbar, a long-

term stability better than 0.1 mbar per year and a resolution in the parts-per-billion range, significantly outperforming the previous two sensors (see figure 3.3). It has a range of about 1600 mbar and is easily damaged by over-pressure, which needs to be considered when filling the reservoirs. Since this sensor was only delivered after the data taking for the measurement of the deuteron's atomic mass was started and the BMP388 was performing good enough for us to not expect an additional benefit by a better stabilization, we decided against replacing the sensor at that time.
As regulated valves we used devices by Bronkhorst. These can be addressed digitally and are available for the flow and pressure ranges stated in section 3.2.1.

3.2.3 Implementation

For the implementation of the pressure stabilization we used an Arduino controller. This Arduino reads the pressure of the BMP388 sensor with a frequency of 3.8 Hz. A PID control loop operates the opening of the bronkhorst regulated valve. For manual control, adjustment of the setpoint and PID parameters and logging of the pressure, the Arduino controller can be connected to a computer. To increase the short-term passive stability of the system, we connected buffer volumes to the cryo reservoirs. For these, we used old cans for cryo-liquids, as these are thermally well insulated. The performance of this system was validated with the 6000-23A, the result is shown in figure 3.3.

3.3 Tilting Mechanism

At the measurement campaign on the Image Charge Shift (ICS) [63], one limiting factor was the limited knowledge of the angle θ and the trap ellipticity ϵ. The usual approach to get θ is the use of equation (2.22), where ϵ is assumed to be small from geometric considerations. However, this is associated with relatively large uncertainties, and one would like to verify these geometric considerations in the experiment. One way to do this would be to vary the angle θ during the experiment.
A tilting mechanism allows such an adjustment of the angle θ. After adjusting the angle to $\theta = 0$, equation (2.22) can be used to gain access to the ellipticity ϵ.
During the ICS measurement, the ellipticity was estimated to be $\epsilon < 0.015$ and the angle was measured to be $\theta = 0.56(8)°$. It is noteworthy, that such an angle cannot come from an overall tilt of the experiment, since over the length of the experiment (≈ 1.5 m) such an angle would amount to several centimeters of horizontal displacement, much more than the clearance in the magnet's bore. Possible sources of such an angle can be a missalignment between the magnetic field and the magnet's bore, or when our trap tower is not totally straight, but more shaped like a banana.
The basic idea of the tilting mechanism is to tilt the whole trap chamber using a mechanical feedthrough. The feedthroughs are placed at the bottom side of the

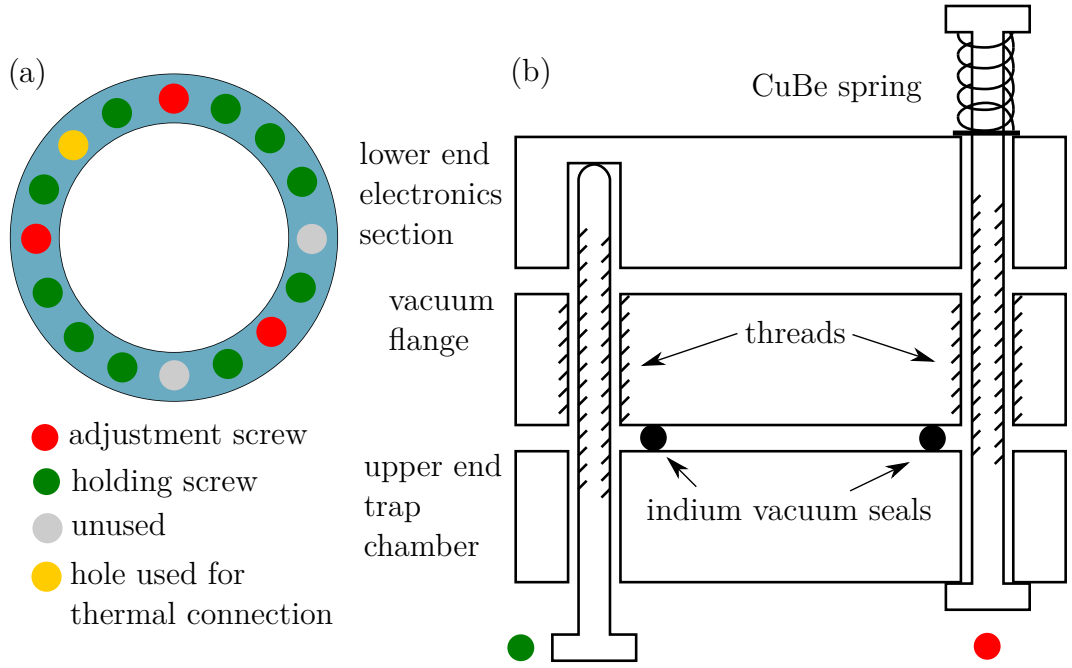

Figure 3.4: Principle of the tilting mechanism. There are two types of screws needed for the tilting mechanism. In (a), their distribution is shown as seen from the cryogenic electronic section. In (b), the functionality of both types of screws is sketched. The vacuum flange and the body of the trap chamber are held together by holding screws. These holding screws also hold the trap chamber to the lower end of the electronics section. There, a spring pushes the trap chamber up. Adjustment screws use the thread in the vacuum flange and a blunt end pressing in a sink hole to push the trap chamber and the lower part of the electronics section apart. One screw whole is used to create a thermal connection from the cryogenic electronics section to the trap chamber.

magnet, since in this direction there is more space available. The LN_2- and the 20K-shield need to be passed. Between the LN_2- and the 20K-shield there is a separable connection, as also shown in figure 3.1. When the tilting mechanism is not in use, this connection is separated to limit the heat transfer from the room temperature to the 4K section. The connection is realized as a ball-point hexagonal head and a hexagonal socket with a guiding system. The elongated parts of the mechanism are made from fiberglass.

The mechanical feedthroughs are used to operate screws which press the trap chamber away from the bottom part of the cryogenic electronic section. In total, three mechanical feedthroughs are implemented to allow moving the trap at an arbitrary angle, see also figure 3.4(a). When one loosens the adjustment screws, springs supporting the holding screws in the cryogenic electronic section reverse the tilting process. This is sketched in figure 3.4(b).

In figure 3.5, photos of the implementation of the tilting mechanism are shown.

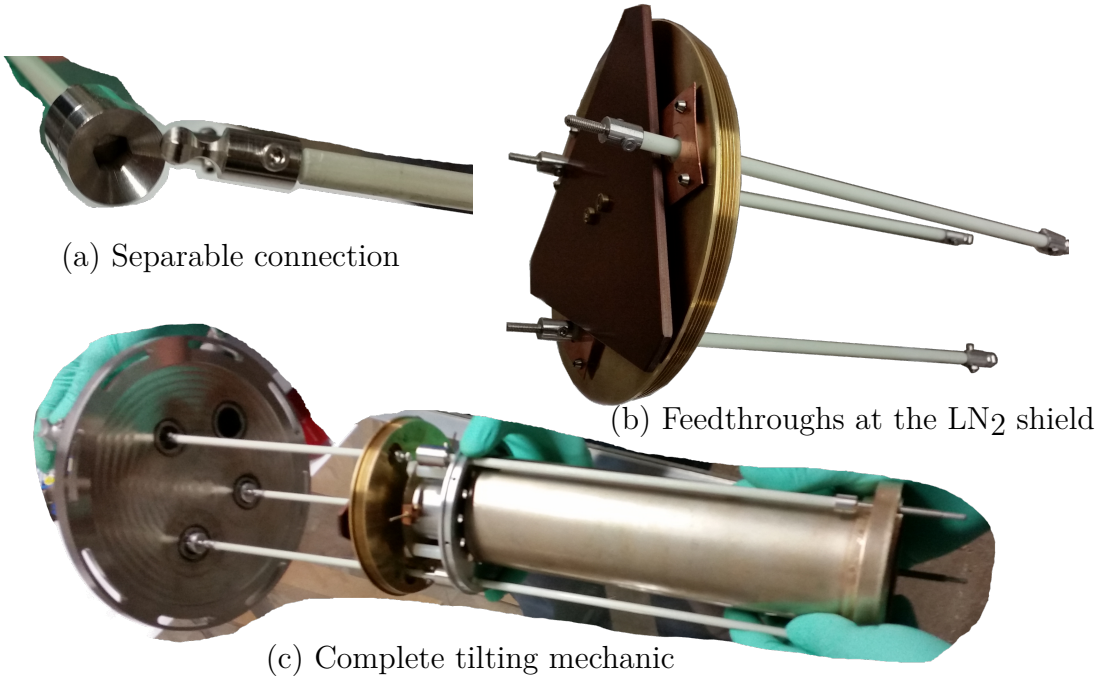

(a) Separable connection

(b) Feedthroughs at the LN_2 shield

(c) Complete tilting mechanic

Figure 3.5: Photos of the tilting mechanism in a test assembly outside of the magnet. In (a) one can see the ballpoint hexagonal head and the corresponding socket of the separable connection. In (b) the bottom end of the LN_2 shield is shown. The visible screws are to be connected with the mechanical feedthroughs in the bottom flange of the experiment. The complete mechanism put together is shown in (c).

3.4 Trap Tower

The heart of the experiment is the trap tower, which consists of in total seven sections. From top to bottom, these are the cone section, a first storage trap (ST1), the precision trap (PT), a second storage trap (ST2), the magnetometer Trap (MT), a third storage trap (ST3) and the creation section (mEBIS). An overview of the complete trap tower is shown in figure 3.6.
The cone section was intended as a novel method to prepare single particles. However, this did not work as intented while the established methods described in section 4.1 led to sufficient results. Therefore, this section was not used for the measurements described in this thesis.
The storage traps, the magnetometer trap and the creation section are reused from the former bound electron g-factor experiment.

3.4.1 Precision Trap

The precision trap was newly designed for LIONTRAP, for details see [54, 7]. It has an increased trap diameter of $r = 5\,\mathrm{mm}$ compared to $r = 3.5\,\mathrm{mm}$ for the reused electrodes, to reduce the image charge shift and improve the harmonicity.

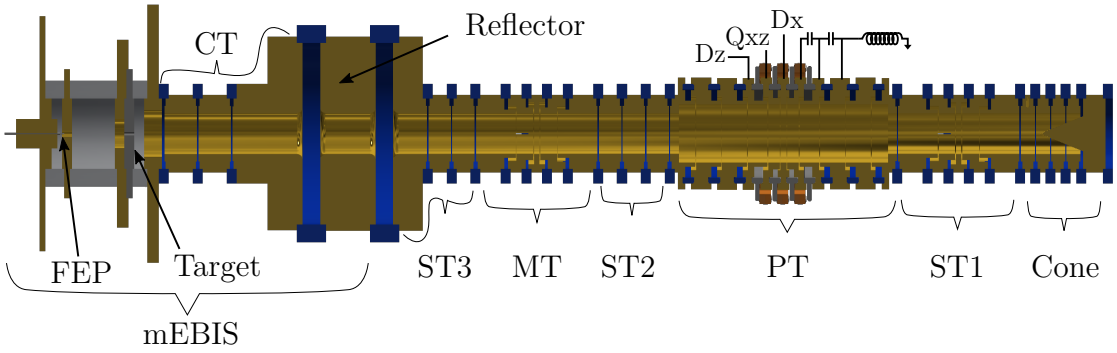

Figure 3.6: Overview of the trap tower. The tower is oriented vertically in our setup with the cone on top. For details and explanations of the acronyms see text.

To further improve the harmonicity, this trap has a second pair of correction electrodes. This allows tuning the coefficients C_4 and C_6 to zero by adjusting the voltage of the correction electrodes. The next order coefficients C_8 and C_{10} are nominally zeroed through the optimized length of the electrodes. The endcaps are segmented into three parts to allow for easier transport. The most outer part provides the transition from $r = 5\,\text{mm}$ to $r = 3.5\,\text{mm}$. This trap configuration is referred to as seven-electrode trap, counting two pairs of correction electrodes, the central ring and a pair of endcaps.
To our knowledge, this is the first seven-electrode trap used as a precision trap, although a seven-electrode trap was used as "preparation trap" in the ISOLTRAP experiment [43]. Connected to this trap are three excitation lines:

1. Dx: This excitation line is connected to one half of the split ring-electrode. It is intended for strong dipolar excitations in the radial direction and used during ion preparation. For the deuteron mass measurement, this excitation line was grounded.

2. Dz: This excitation line is connected to the outer upper correction electrode. It is intended for strong dipolar excitations in the axial direction and also used during ion preparation. This excitation line was also grounded during the deuteron mass measurement.

3. Qxz: This excitation line is connected to one half of the inner upper correction electrode. It is intended for quadrupolar excitations, which couple the axial and radial directions. It has dipolar components in both the radial and axial direction and can hence be used universally. This excitation line has been used exclusively during the deuteron mass measurement.

As detection system, one axial resonator is connected to this trap. This axial resonator has an inductance of $L = 3.363\,\text{mH}$. Its resonance frequency can be tuned by applying a voltage to a built-in varactor diode in the range of $\frac{\omega_\text{res}}{2\pi} \approx 3\,\text{kHz}$. The Q-value is $Q \approx 4000$. The resonator is connected directly to the first lower endcap electrode, and the outer lower correction electrode as well as one half

of the inner lower correction electrode are connected capacitively. This results in an effective electrode distance of $D = 9.6\,\mathrm{mm}$. All other electrodes are grounded AC-wise.
The DC voltages are supplied by two UM1-14 voltage sources by Stahl-electronics. There, the outer correction electrodes share a precision mode channel, however, these can be set asymmetric by voltage mixing. The voltages are filtered, once in the room temperature region, once in the 4 K section.

3.4.2 Magnetometer Trap

The magnetometer trap (MT) is intended to monitor magnetic field changes. If these field changes are uniform over the distance between the MT and the PT, which is about 4.2 cm, one can use this monitoring to potentially improve the statistical precision of mass measurements as outlined in [7].
This trap is a five-electrode trap and the reused analysis trap of the LIONTRAP predecessor experiment, with the ferromagnetic ring replaced.
The upper correction electrode is split and has an excitation line connected to one half of it. Connected to the trap are in total three axial resonators. Two of these resonators are intended as axial resonators for ions connected to the lower correction electrode and the lower endcap, respectively. One resonator connected to the upper endcap is intended as axial resonator for trapped electrons, see section 6.2 for details. The DC-voltages are supplied by UM1-14 precision channels, with the correction electrodes sharing one precision mode channel as in the MT.

3.4.3 Storage Trap One

While the other storage traps only consist of three electrodes and have no optimized harmonicity, the storage trap 1 (ST1) is different in that regard. It is a five-electrode trap and the reused precision trap of the LIONTRAP predecessor experiment. The trap has an excitation line connected to one half of a split correction electrode. The resonator connected to the lower endcap of the MT is capacitively connected to the lower correction electrode of the ST1, which allows this trap to be operated with ions as well. Additionally, an amplifier and a feedback line intended to be used with trapped electrons are connected to this trap, for details see section 6.2.
In this trap, we tested an idea to potentially increase the stability of the DC voltage. To this end, the DC voltage supplied by the fast mode channels of an UM1-14 passes through a transistor of type BF545B. This transistor is based on silicon and as such it becomes essentially insulating at 4 K. However, for this specific transistor the transition temperature is only slightly above 4 K. The idea is to heat the board of the transistor, apply a voltage to the trap, and then let the transistor freeze out. In this manner, the voltage is "frozen-in", and potentially more stable than before. The performance of this system is evaluated in section 4.7.

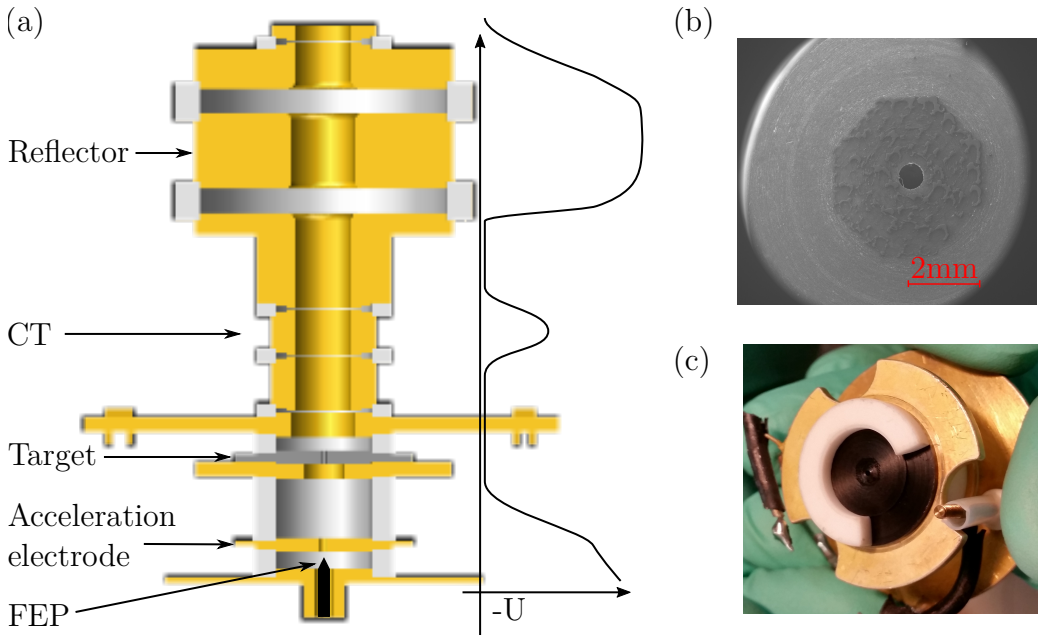

Figure 3.7: Production section. In (a) a sketch of the mEBIS is shown, together with a qualitative plot of the voltages used for ion production. An electron microscope image of the target with the printed layer of deuterated molecules visible is shown in (b), a photo of it in (c).

3.4.4 Production Section

The bottom part of the trap tower is the section used to produce ions. This is done using a *miniature electron beam ion source* (mEBIS) [76, 77]. There, a field emission point (FEP) emits electrons. These electrons are accelerated and reflected multiple times by a high voltage, until they hit a target, get reabsorbed and ablate atoms. The atoms are ionized by the electron beam and captured in the capture trap (CT), see also figure 3.7(a). This method has already been used at the predecessor experiment of LIONTRAP and is able to reliably produce ions in charge states with ionization energies of up to $\approx 1\,\mathrm{keV}$ [54].

The available ion species depend on the target material. Therefore, the target material needs to contain the elements of interest. Additionally, it has to be machinable and it has to be electrically conducting, otherwise the electrons would build up electric charges interfering with the function of the mEBIS. For the proton mass measurement campaign, we used a target made from carbon-nanotube-filled PEEK called TECAPEEK [78]. PEEK (polyether ether ketone) is a polymer, as an organic compound it contains plenty of carbon and hydrogen. It is machinable, and the carbon-nanotubes ensure electrical conductivity.

For deuterium however, the natural abundance on earth is only about 0.015% [79] making a production from the bulk material of the target unlikely. To improve the odds of getting deuteron into our trap, we printed a layer of deuterated molecules on top of the target surface using a Drop-on-Demand inkjet printing system in

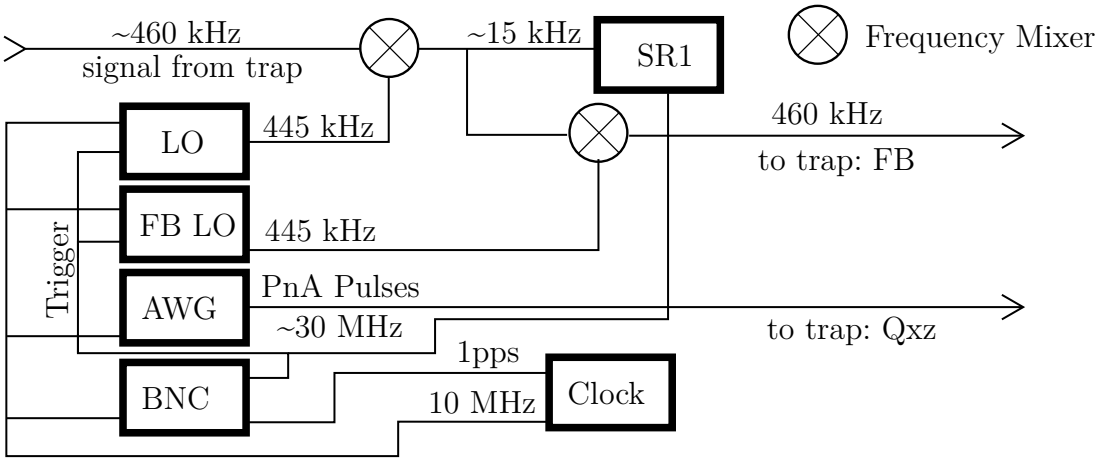

Figure 3.8: Timing System. All devices are locked to an rubidium frequency standard FS725 by Stanford Research Systems and triggered by the BNC. For details see text.

cooperation with the Institute for Nuclear Chemistry [80]. This target is shown in figure 3.7(b) and figure 3.7(c).

3.5 Timing System

For the phase-sensitive measurements, a precise timing system is necessary. This system is sketched in figure 3.8.
All devices are locked to a 10 MHz rubidium frequency standard FS725 by Stanford Research Systems. This clock also provides a 1 pulse per second (pps) reference. Trigger pulses given by a pulse generator BNC555 from Berkeley Nucleonics are synchronized with the 1 pps reference. Since the local oscillator (LO) and the Oscillator used for Feedback (LO FB) produce a sinusoidal signal with a frequency, which is a multiple of 1 Hz, their phase is constant relative to the 1 pps pulse. Therefore, the local oscillators can be triggered independently from the rest of the system.
Signals from the trap are in the axial frequency range of about 460 kHz. They are mixed with a sinusoidal signal of the local oscillator into the audio frequency range of about 15 kHz, which is then analyzed on the FFT device, an SR1 audio analyzer. This has the advantage, that the triggering of the FFT device is much less critical than it would have been without the down-mixing process.
The only signal in the frequency range of the modified cyclotron motion ($\approx$ 30 MHz), is the excitation used in the PnA technique. There, a dual channel arbitrary waveform generator (AWG) is used. The two pulses including the delay T_{evol} are programmed as arbitrary waveforms for the two channels of the AWG, and the AWG is triggered only once. In this manner, the timing of the pulses only depends on the internal timing of the AWG, avoiding problems with trigger accuracy entirely.

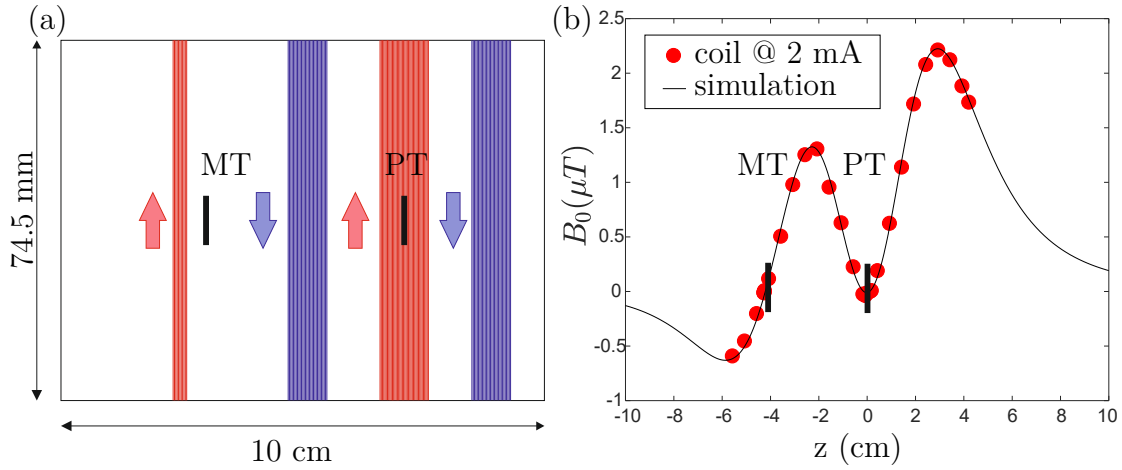

Figure 3.9: In-situ shim coil. In (a) the number, direction and position of the windings is shown. They produce the field shown in (b), once simulated, once measured in a test setup using a hall probe. The black bars indicate the positions of the MT and the PT. There, the magnetic field from the coil is designed to be close to zero.

3.6 In-Situ Shim Coil

For the proton mass measurement campaign, the limiting uncertainty was caused by the quadratic component of the magnetic field inhomogeneity B_2. As discussed in section 2.1.3, the modified cyclotron frequency shifts proportional to $B_2\hat{z}^2$. Since $\hat{z}$ is thermally distributed during the PnA measurement, this leads to a shift $\Delta\nu_+ \propto B_2 T_z$. The uncertainty of this shift is thus

$$\delta\Delta\nu_+ \propto \sqrt{(\delta B_2 T_z)^2 + (B_2 \delta T_z)^2}, \tag{3.2}$$

where δ denotes the uncertainty of a quantity and assuming both quantities are measured independently. In the Proton campaign, there first term in equation (3.2), $B_2\Delta T_z$ was dominant. Since a significant improvement of the measurement of the ions temperature was not expected, in order to improve the uncertainty of this systematic shift it was necessary to reduce the magnetic inhomogeneity by implementing a superconducting shim coil.
Originally, such a shim coil was already planned and implemented for the proton mass measurement, many details on the coil can also be found in [7, Appendix F]. However, it turned out, that the current necessary to compensate for the B_2 in the trap would quench the shim coil, making it impossible to use the coil in the measurement campaign. Additionally, we noticed that attaching a current supply to the coil introduced noise to our detection system. Therefore, we decided to implement a superconducting connection. In this way, the coil can be charged, the power supply disconnected and the inhomogeneity stays compensated without the need of a power connection. To this end, the coil has to supply connections, and the short part in between is wound around a heating resistor. To charge

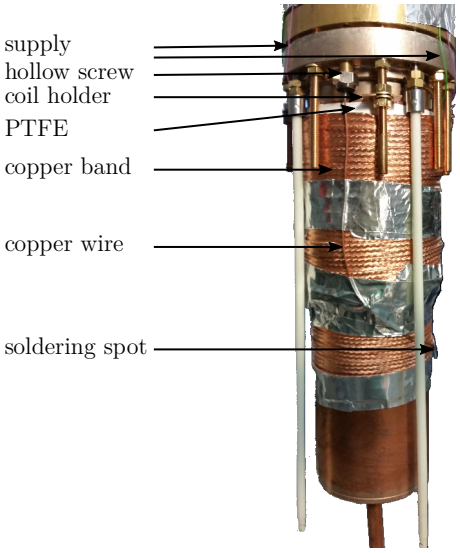

Figure 3.10: Photo of the shim coil. The coil is wound on a coil holder, which is placed around the trap chamber. It is fixed by a layer of PTFE. A copper band ensures that heat can be dissipated efficiently. The connection to the 4K section is done by a thick copper wire, which is soldered to the 4K section as well as the copper band.

the coil, a current is fed through the heating resistor, heating the part of the coil wound around the resistor and breaking the superconductivity there. The current is applied through the supply connections and gets increased slowly, until the desired current is reached. Then, one stops the heating and waits for a few seconds. Afterwards, the supply is disconnected, and one can check if the process worked by measuring the magnetic field.
The field produced by this coil is shown in figure 3.9. It has nominally zero field at the positions of the PT and the MT (black lines). In this way, the cyclotron frequency does not change too much after charging the coil, which simplifies handling. Also, slight changes in the current in the superconducting coil have their influence on the cyclotron frequency suppressed. Such changes can occur, since the coil is closed superconducting, and therefore, the magnetic flux in the coil stays constant.
A series expansion of the simulated field of the coil around the minimum where the PT is to be placed yields:

$$\begin{aligned} B(z) &\approx (B_{0,I} + B_{2,I} z^2 + B_{3,I} z^3) I_{\text{coil}}, \qquad \text{where} \\ B_{0,I} &\approx 5\,\text{nT}\,\text{mA}^{-1} \\ B_{2,I} &\approx 3.6\,\text{nT}\,\text{mA}^{-1}\,\text{mm}^{-2} \\ B_{3,I} &\approx 19\,\text{pT}\,\text{mA}^{-1}\,\text{mm}^{-3}. \end{aligned} \tag{3.3}$$

The biggest source of error in these coefficients is the alignment of the coil with respect to the trap. If one assumes that the coil is displaced by an amount of

$z_0 = \pm 2\,\mathrm{mm}$, this results in coefficients:

$$\begin{aligned} \tilde{B}_{0,I} &= B_{0,I} + B_{2,I} z_0^2 + B_{3,I} z_0^3 && \approx \pm 20\,\mathrm{nT\,mA^{-1}} \\ \tilde{B}_{2,I} &= B_{2,I} + 3 B_{3,I} z_0 && \approx 3.6 \pm 0.1\,\mathrm{nT\,mA^{-1}\,mm^{-2}}. \end{aligned} \tag{3.4}$$

During the proton mass measurement campaign, the residual magnetic inhomogeneity B_2 was measured to $B_2 = 0.270(15)\,\mu\mathrm{T\,mm^{-2}}$. To compensate such an inhomogeneity with this shim coil one would need a current of 75 mA. The coil was tested in a cold-head to sustain a current of up to 200 mA, which we deemed sufficient. In figure 3.10, a photo of the built-in coil is shown.

4 Trap Characterization and Preparatory Measurements

In this chapter, I describe measurements and operations performed in preparation of the deuteron mass measurement. This starts with the production of ions in section 4.1.

4.1 Ion Production

The ions of interest have been produced in the mEBIS introduced in section 3.4.4. To create ions with different ionization energies, the FEP voltage was set accordingly. The electron beam energies were chosen to be $-100\,\mathrm{V}$ for deuteron or HD^+, $-350\,\mathrm{V}$ for $^{12}C^{4+}$ and $-1000\,\mathrm{V}$ for $^{12}C^{6+}$. The reflector voltage was always set to a voltage about 1.15 times the FEP voltage.
The ions are captured in the CT, which after charge breeding is set to $-100\,\mathrm{V}$ for a few seconds. This makes all ions with a mass-to-charge ratio of $m/q \gtrsim 16\,\mathrm{u}\,e^{-1}$ unstable, see equation (2.11). Especially large, singly charged molecules are removed in this way, which would otherwise potentially form a hard to detect contamination.
The ions are transported into the PT, where a single ion of interest needs to be prepared. To this end, different techniques can be used:

1. Axial cleaning: Here, a strong broadband excitation through the axial dipolar excitation line Dz strongly excites the axial motion of unwanted ions. The trap potential is subsequently lowered, which allows a large portion of the excited ions to escape.

2. Magnetron cleaning: A broadband noise in the frequency region of the magnetron motion is applied to the radial dipolar excitation line Dx. This heats the magnetron motion of unwanted ions until they are lost eventually. At the same time, the magnetron motion of the ion of interest is cooled by continuous sweeps in the frequency range $\omega \approx \omega_z + \omega_-$.

In practice, we mostly used axial cleaning, since using the Dx excitation line introduced significant noise into our detection system. This makes it hard to quantify whether the cooling works properly.
The particle composition in the trap can to some degree be analyzed by taking mass spectra. For this, the trap voltage is swept over the accessible range while simultaneously monitoring the voltage in a frequency window around the resonator.

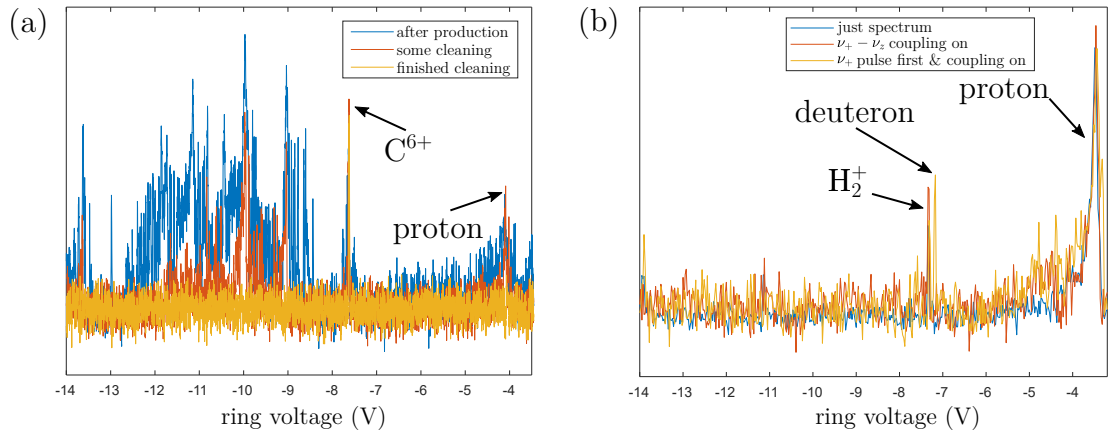

Figure 4.1: Mass Spectra. In (a) three mass spectra illustrate the cleaning process after the production of $^{12}C^{6+}$. The difference in the baseline is artificially introduced for better visibility. In (b) the visibility of deuteron in the mass spectrum is enhanced by applying a pulse on ν_+ and adiabatically transfering this excitation to the axial mode.

If an ion comes into resonance with the tank circuit, it dumps part of its axial energy into the circuit leading to an increased voltage. To increase the axial energy, an excitation slightly above (when sweeping from high to low voltage) the frequency of the axial resonator can be applied. In figure 4.1(a) three mass spectra documenting the cleaning process after the production of $^{12}C^{6+}$ are shown. When one wants to be sensitive to a particle species with low abundance like in our case deuterium, one can also apply a pulse at the modified cyclotron frequency of the ion of interest prior to taking the mass spectrum. During the mass spectrum, a sinusoidal excitation with frequency slightly above $\nu_+ + \nu_{\text{res}}$ is applied. When the axial frequency of the ions is swept from high to low, the excitation will be resonant with the sideband $\nu_+ + \nu_z$ shortly before the ion of interest is resonant with the tank circuit. For sufficiently strong excitations, this results in an adiabatic transfer of the energy in the cyclotron mode to the axial mode, and thus to an increased signal for only the ion species, whose modified cyclotron motion has been excited.

In figure 4.1(b), a sequence of mass spectra visualizing this process in the production of deuteron is shown. In the axial mode, deuteron is hard to distinguish from H_2^+, the axial frequencies are only $\approx 180\,\text{Hz}$ apart, which is not much in a trap loaded with clouds of ions. However, the modified cyclotron frequencies are $\approx 22\,\text{kHz}$ apart, which is easily distinguishable.

In this way, it was possible to produce and isolate single deuterons without too much effort. Whether the observed deuteron ions actually originate from the deuterated material placed on the target is unfortunately hard to say, since there are no comparable data without the target built-in available. Using the same method, a single HD^+ molecular ion was also produced and isolated during the deuteron measurement campaign.

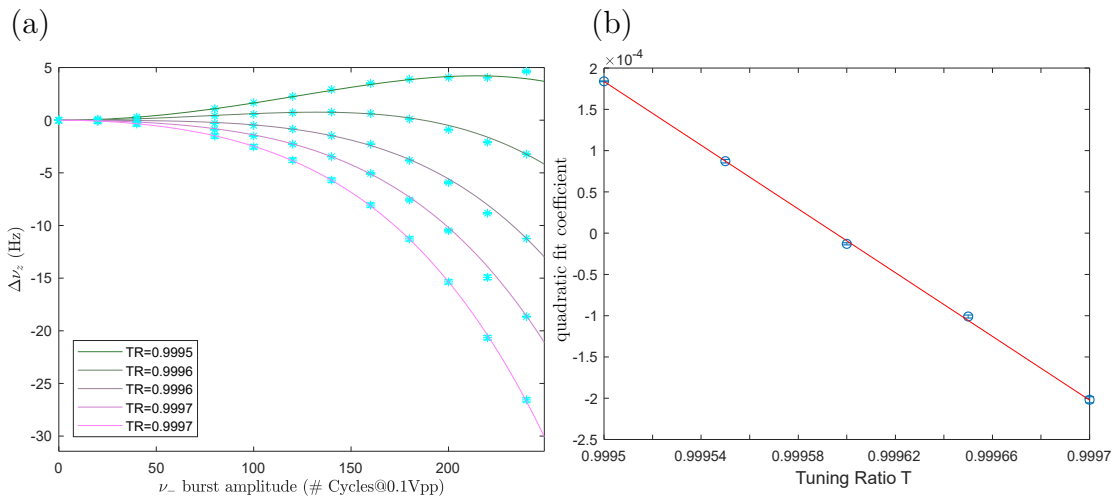

Figure 4.2: Electric field optimization. In (a), the axial frequency shift $\Delta\nu_z$ is taken as a function of the magnetron excitation strength and fitted with a function $f(x) = ax^2 + bx^4$ for different tuning ratios. In (b), the coefficient a is plotted versus the tuning ratio T. The intersection of the resulting linear function with zero gives the tuning ratio where $C_4 = 0$, and the slope gives a calibration of the excitation strength.

4.2 Electrostatic Field Optimization

The optimization of the electrostatic field is of great importance. Anharmonicities do not only lead to frequency dependent shift as described in section 2.1.3, but also to difficulties when reading out the phase in a PnA measurement. For the optimization, axial frequency shifts are measured as a function of the magnetron excitation. This process needs to be repeated after every particle production, since the electron beam or ions removed from the trap can potentially charge up non-conducting patches on the electrode surfaces. This can be described as so called patch potentials and has been evaluated in our trap to be in the order of $U_{\text{patch}} < 10\,\text{mV}$ [7].
In this section, I present one exemplary optimization process and give an overview over the electrostatic inhomogeneities during the deuteron mass measurement campaign.
In the seven-electrode trap, there are two parameters which can be used to adjust the harmonicity of the trap. These are the voltage of both pairs of correction electrodes (U_{C1} and U_{C2}), often expressed as tuning ratio T_1 and T_2,

$$\begin{aligned} T_1 &= \frac{U_{C1}}{U_{\text{ring}}} &&=: T\,T_{1,\text{start}} \\ T_2 &= \frac{U_{C2}}{U_{\text{ring}}} &&=: T\,T_{2,\text{start}}. \end{aligned} \tag{4.1}$$

Here, U_{ring} is the voltage applied to the ring electrode. For easier handling, the combined tuning ratio T is used, since the axial frequency ν_z is in first order inde-

pendent of this parameter. One expects the first order anharmonicity to depend on the tuning ratio in the following way:

$$\begin{aligned} C_4 &= E_4 + T_1 D_{4,1} + T_2 D_{4,2} \\ &:= E_4 + D_2 T. \end{aligned} \tag{4.2}$$

For our PT, the value for D_2 can be taken from a simulation of the trap geometry, which yields $D_2 = 0.79$ [54, 7]. From the manufacturing precision of the trap, this value has an uncertainty of about 10%. However, I will omit this uncertainty here, as it will be discussed in section 4.4.
The optimization process then works in the following way:

1. Measure the axial frequency shift as a function of the magnetron excitation energy, for different combined tuning ratios.

2. Fit a low order polynomial with only even orders to the data. The coefficients in this polynomial are proportional to the coefficients of the anharmonicity, see also equation (2.24a).

3. Plot the coefficient proportional to the quadratic term of the polynomial as a function of the combined tuning ratio. This gives a linear function as expected from equation (4.2). The slope of this function can be compared with theory to give a calibration of the excitation strength. The intersection with zero corresponds to the tuning ratio where $C_4 = 0$.

4. Evaluate higher order terms, especially C_6, by looking at the higher order coefficients of the polynomial. If these are too large, change either $T_{1,\text{start}}$ or $T_{2,\text{start}}$ and repeat the optimization process.

One example of this process is shown in figure 4.2. There, the optimal tuning ratio coming from the fit was $T = 0.999595$, the uncertainty on the leading order anharmonicity $\delta C_4 \approx 1 \cdot 10^{-6}$, and the C_6 value at the optimal tuning ratio $C_6 = 3.2(1.6) \cdot 10^{-4}$. Using the theory value for the slope given above, one can derive the calibration constant

$$\kappa_- = 74 \, \frac{\mu\text{m}}{\#\text{cycle}\,\text{Vpp}}. \tag{4.3}$$

While the uncertainties of the values for C_4 and C_6 are relatively small, this treatment is, of course, incomplete. It is not clear, how many orders of the polynomial should be considered, or how far one should excite the particle to be as sensitive as possible to the coefficients C_4 and C_6, which are relevant to the systematic effects in the mass measurement. An analysis on this topic is shown in figure 4.3.
There, the tuning ratio was fixed to the value determined to be optimal in the manner described above. Then, the frequency shift once again was measured as a function of the magnetron excitation strength expressed as the numbers of cycles $n \propto r_-$ used for the excitation, as shown in figure 4.3(a). Analogously to the proceeding above, these frequency shits are fitted with a polynomial with only even

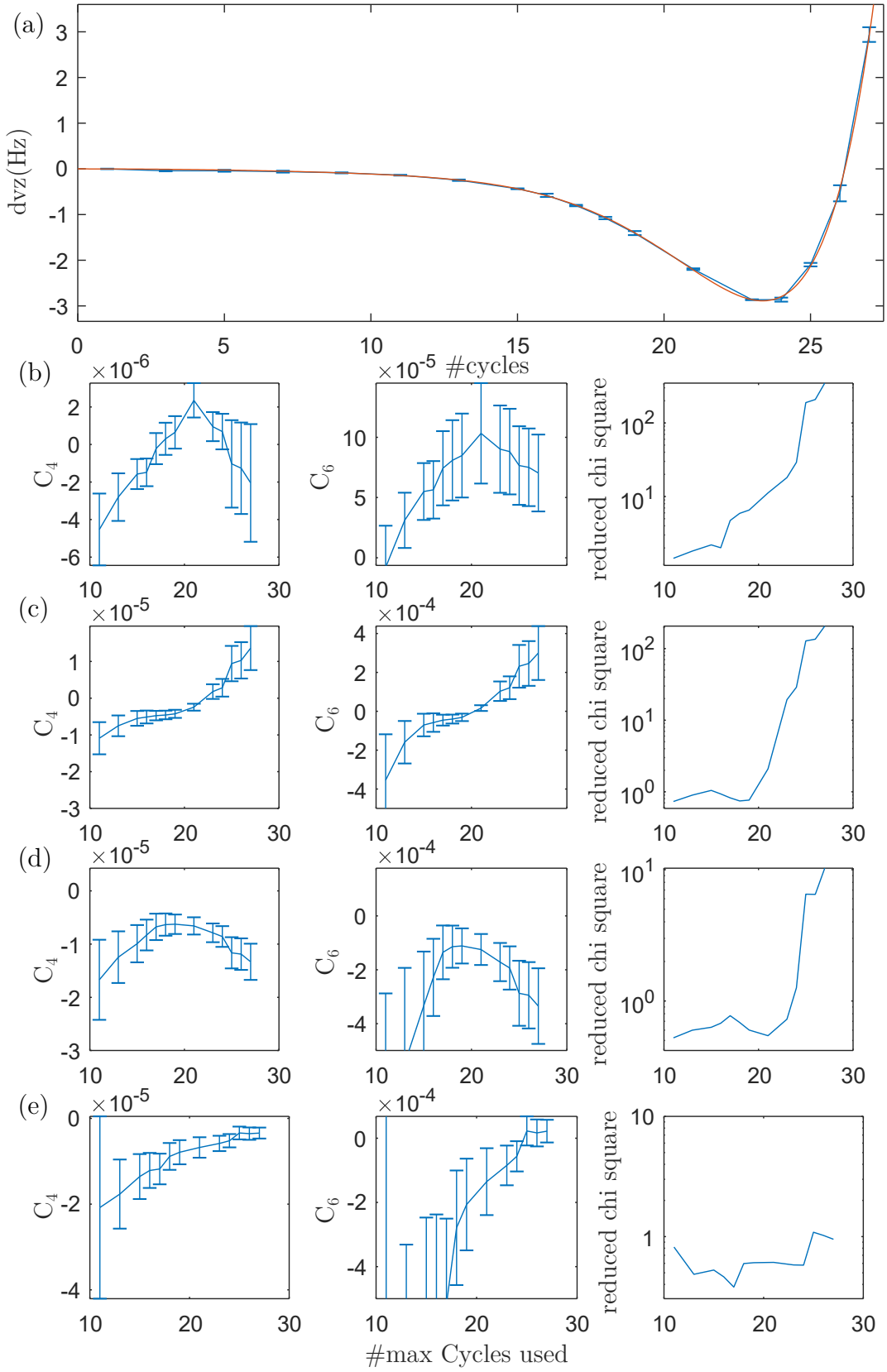

Figure 4.3: Electric field optimization II. Dependence of C_4, C_6 and the reduced χ^2 on the fitrange and the order of the used polynomial. For details see text.

orders, but with the maximum order of the polynomial and the fitrange varied. This is shown in figure 4.3(b-e). In figure 4.3(b-e), polynomials up to order r_-^4, r_-^6, r_-^8 and r_-^{10} have been used, respectively. For each order, the extracted values for C_4 and C_6 and the reduced χ^2 of the fit are shown as a function of the fitrange. For polynomial fits up to r_-^8, the reduced χ^2 starts to increase significantly at about 20 cycles $\widehat{\approx}$ 1.6 mm. In our PT, the series expansion parameter r_-/d_{char} is then in the order of ≈ 0.3, making it hard to use this series expansion approach, where only contributions up to a certain order of r_-/d_{char} are considered. When looking at the C_4 and C_6 coefficients, a clear dependency on the fitrange is visible for all the used models.
Such measurements were repeated for all the ions used in the deuteron measurement campaign. The resulting C_4 values were in the range of $\pm 1 \cdot 10^{-5}$, with the measurement shown here being closer to $-1 \cdot 10^{-5}$. For the analysis of the deuteron and HD^+ data, we wanted to use one value for each C_4 and C_6 for the whole campaign. Therefore, we used the following values:

$$\begin{aligned} C_4 &= 0 \pm 1 \cdot 10^{-5} \\ C_6 &= 1(1) \cdot 10^{-4}. \end{aligned} \tag{4.4}$$

As shown in section 5.3.2, these values are more than sufficient to not limit mass measurements. However, they will play a role in the optimization of the magnetic field homogeneity presented in the next section 4.3.

4.3 Magnetostatic Field Optimization

In this section, I describe how the in-situ shim coil was used to optimize the magnetic field homogeneity.
The probe to measure the magnetic field homogeneity is the axial frequency ν_z as a function of the modified cyclotron radius r_+. Taking into account the quadratic magnetic inhomogeneity B_2, the leading order electric anharmonicty C_4 and relativistic shifts, this shift is given by

$$\frac{\Delta\nu_z}{\nu_z} = \left[\underbrace{\frac{B_2}{4B_0}\frac{\nu_+ + \nu_-}{\nu_-}}_{\text{magnetic}} \underbrace{-\frac{C_4}{C_2}\frac{3}{2d_{\text{char}}^2}}_{\text{electric}} \underbrace{-\frac{\omega_+^2}{4c^2}}_{\text{relativistic}} \right] r_+^2. \tag{4.5}$$

It is instructive to insert numbers to get a feeling for the orders of magnitude involved here. For the $B_2 = 0.27\,\mu\text{T}\,\text{mm}^{-2}$ during the proton mass campaign, the first term of equation (4.5) evaluates to a frequency shift of 16 Hz at an excitation amplitude of $r_+ = 500\,\mu\text{m}$. In an optimized trap with $C_4 < 10^{-5}$ the corresponding shift evaluates to < 60 mHz. This is small enough to not play an important role while adjusting the current in the coil. However, from this evaluation it already becomes clear that this will limit the precision, with which B_2 can be measured in the end. The relativistic shifts are even smaller and about 10 mHz for this scenario.

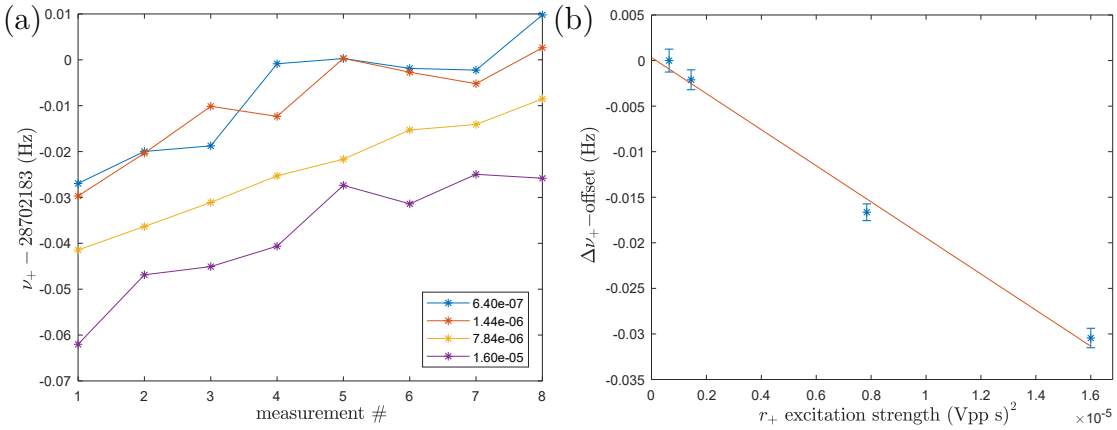

Figure 4.4: Cyclotron radius calibration. To calibrate the cyclotron radius, shifts of the cyclotron frequency ν_+ of a single deuteron as a function of the cyclotron radius r_+ are evaluated with the PnA method. In (a), the data for different excitation strengths are shown. The data exhibit a linear drift, which is removed by a moving average. The resulting dependency on the cyclotron radius is shown in (b). In this mode, relativistic shifts are dominant, which allows to calibrate the excitation strength $r_+^2 = \kappa_+^2 (Ut)^2$ from the fitted slope. In this measurement, the result is $\kappa_+ = 0.01904(62)\,\mathrm{m/Vpp/s}$.

4.3.1 First Operation

The first attempt of charging the shim coil was also done at a time, where we did not have a calibration for the excitation in the modified cyclotron motion. There, the modified cyclotron motion was excited such that a shift of $\Delta\nu_z = -9.8\,\mathrm{Hz}$ was observed. Then the coil was charged to 51 mA, which changed the shift to $\Delta\nu_z = 10.9\,\mathrm{Hz}$, demonstrating that the coil was working. Despite the still lacking calibration, we were already able to see, that the current necessary to compensate our B_2 was about 25 mA. Together with equation (3.4), this hints at an uncompensated $B_2 \approx -0.09\,\mu\mathrm{T\,mm^{-2}}$, significantly lower than measured during the proton mass campaign.

Charging the coil to this value also shifted the modified cyclotron frequency by $-7.4\,\mathrm{Hz} \mathrel{\widehat{=}} 260\,\mathrm{nT}$, suggesting that the accuracy goal of 2 mm was fulfilled.

A later measurement with the B_2 coil quenched shortly before the measurement confirmed an uncompensated value of $B_{2,\mathrm{uncomp}} = -0.122(11)\,\mu\mathrm{T\,mm^{-2}}$. It is not obvious that the B_2 produced by the coil in a test-setup matches the B_2 produced in the magnet. The magnetic flux produced by the coil will, of course, also induce currents in the various shim coils of the magnet. Their exact geometry is a corporate secret of the magnet's manufacturer, which makes it hard to estimate such an effect.

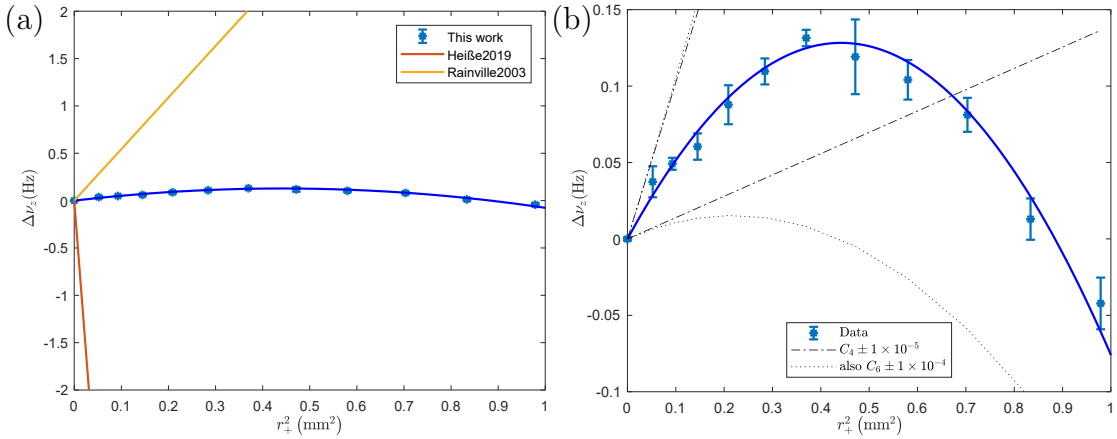

Figure 4.5: Magnetic field optimization. The magnetic field homogeneity is evaluated by measuring axial frequency shifts as a function of the radius in the modified cyclotron motion. In a plot with the modified cyclotron motion squared as the x-axis, a B_2-term corresponds to a linear dependency. In (a), a measurement with deuteron in our trap is shown together with two other systems: Our setup during the proton mass campaign, and the Penning trap at the MIT, where in-situ shimming using the coils of the magnet was performed [81]. In (b), a zoom-in into our data is shown. The remaining dependency can be easily explained by residual electric anharmonicities shown as grey lines.

4.3.2 Calibrating the Cyclotron Radius

To further quantify the residual value of B_2, one needs to calibrate the modified cyclotron radius r_+. To this end, the modified cyclotron frequency ν_+ is measured as a function of the excitation strength, which is a product of the excitation amplitude U and the excitation time t. In this motional mode, relativistic shifts are completely dominant, especially for a B_2 close to zero, see also equation (2.71) and equation (2.32).
This can be achieved by varying the strength of the dipolar excitation in the PnA method. Such a measurement for a single deuteron is shown in figure 4.4. There, the ν_+ frequency is measured with four different excitation settings, and this is repeated eight times as shown in figure 4.4(a). To account for the slow drift of the magnetic field, a moving average was used. After preparing the data in this manner, the frequency shifts can be plotted as a function of the excitation radius squared, as shown in figure 4.4(b). There, one expects a linear dependency, and from the fitted slope and equation (2.71) one can deduce the calibration constant. If the fitted slope is denoted as k in units $\mathrm{Hz\,Vpp^{-2}\,s^{-2}}$, the calibration constant κ_+ is given by

$$\kappa_+ = \sqrt{-\frac{2kc^2}{\omega_+^2 \nu_+}}. \tag{4.6}$$

The cyclotron radius can then be easily calculated as $r_+ = \kappa_+ U t =: \kappa_+ A$, where

U is the used excitation voltage and t the excitation time. The product of both is abbreviated as A and will become especially important in section 5.3.1. In this particular measurement, the resulting value for κ_+ was $\kappa_+ = 0.01904(62)\,\mathrm{m/Vpp/s}$.

4.3.3 Estimating the Residual B_2

With an exact calibration of the cyclotron radius at hand, one can now estimate the remaining B_2. Such a measurement is shown in figure 4.5. There, the cyclotron radius squared is shown on the x-axis. In this way, a linear dependency corresponds to B_2 and a quadratic dependency to B_4. Even for excessively large excitation amplitudes of about 1 mm, the frequency shifts are still well below 1 Hz. From a polynomial fit to the data, the value for B_2 can be extracted using equation (4.5) and assuming $C_4 = 0$. This yields for this measurement $B_2 = 0.0026(3)\,\mu\mathrm{T\,mm^{-2}}$. In figure 4.5(a), this measurement is compared to two reference values. One is the $B_2 = 0.27\,\mu\mathrm{T\,mm^{-2}}$ in our trap during the proton mass campaign. Compared to this value, the shimmed B_2 is smaller by about a factor of 100. The other reference value is a measurement by the Penning trap group at the MIT [81]. There, in-situ shimming using the shim coils of the magnet has been attempted. However, inserting the charging rod led to significant drifts in the coils, limiting the resulting magnetic inhomogeneity to the shown value[1].
In figure 4.5(b), a zoom-in on the data is shown. A linear dependency is still remaining. However, the gray lines illustrating the contribution of a residual electric anharmonicity C_4 and C_6 show, that further optimization of the magnetic field homogeneity is only possible, if the uncertainty in the electric anharmonicity is reduced.
During the deuteron mass campaign, several measurements of κ_+ and B_2 were repeated, showing consistent results. To evaluate the systematic shifts as shown in section 5.3.2 and section 5.4.2, we used a global value of

$$B_2 = 0.0024(24)\,\mu\mathrm{T\,mm^{-2}}. \tag{4.7}$$

For a small B_2, the shift of the axial frequency as function of the modified cyclotron radius r_+ is no longer dominated by magnetic inhomogeneities, rather electric anharmonicities become relevant. One then can measure the axial frequency shifts as a function of the cyclotron radius at a well defined tuning ratio. Since the modified cyclotron radius r_+ can be independently calibrated as described above, this allows to check the simulated value for D_2 used in the calibration of the constant for the magnetron excitation κ_-, which is is presented in section 4.4. The linear magnetic field gradient was not minimized. With the B_2 coil charged, it was measured to be $B_1 = 0.00234(12)\,\mathrm{mT\,mm^{-1}}$ by applying asymmetric voltages. The corresponding effect on the cyclotron frequency is negligible.

[1] To compare the MIT inhomogeneity to ours, the relevant parameter is the ratio of B_2 to B_0. For the curve shown in figure 4.5(a), the value of B_2/B_0 reported by the MIT [81] was used.

4.4 Temperature Measurement

The basic idea of how we measure an ion's temperature at LIONTRAP is to amplify temperature related frequency shifts. In equation (2.59) it is shown, that the amplitude of an ion's motion after a dipolar excitation depends on the phase relation between the excitation pulse and the ion's motion. For the cyclotron motion, this can be written as

$$r_+^2 = r_{\text{exc}}^2 + r_{\text{thermal}}^2 + 2r_{\text{exc}}r_{\text{thermal}}\cos(\Delta\phi), \tag{4.8}$$

where $\Delta\phi$ is typically random for repeated excitations, r_{exc} is the excitation amplitude expressed as a radius. The thermal motional amplitude r_{thermal} is a random variable distributed according to a Boltzmann distribution, with probability density

$$\begin{aligned} p(E_+)\mathrm{d}E_+ &= \frac{1}{k_B T_+} e^{-\frac{E_+}{k_B T_+}} \mathrm{d}E_+ \\ p(r_+)\mathrm{d}r_+ &= \frac{m\omega_+^2 r_+}{k_B T_+} e^{\frac{-m\omega_+^2 r_+^2}{2k_B T}} \mathrm{d}r_+ \end{aligned} \tag{4.9}$$

where E_+ is the energy in the modified cyclotron mode, $E_+ = m\omega_+ r_+^2/2$ and T_+ the corresponding temperature. One can examine the expectation value and the standard deviation of the frequency shifts $\Delta\nu_z$ arising from such an excitation. These are typically proportional to r_+^2, the constant of proportionality is denoted as P_1. The expectation value is then given by

$$\begin{aligned} < \Delta\nu_z > &= P_1 < r_+^2 > \\ &= P_1(< r_{\text{exc}}^2 > + \underbrace{2 < r_{\text{exc}} r_{\text{thermal}} \cos(\Delta\phi) >}_{=0} + \underbrace{< r_{\text{thermal}}^2 >}_{\text{negligible}}) \\ &\approx P_1 r_{\text{exc}}^2, \end{aligned} \tag{4.10}$$

and the standard deviation (denoted as δ):

$$\begin{aligned} \delta(\Delta\nu_z) &= P_1 \delta(r_+^2) \\ &= P_1(\underbrace{\delta(r_{\text{exc}}^2 >)}_{=0} + 2r_{\text{exc}}\delta(r_{\text{thermal}}\cos(\Delta\phi)) + \underbrace{\delta(r_{\text{thermal}}^2)}_{\text{negligible}}) \\ &\approx 2P_1 r_{\text{exc}} \sqrt{\frac{< r_{\text{thermal}} >^2}{2} + \frac{1}{2}(\delta(r_{\text{thermal}}))^2} \\ &= 2P_1 r_{\text{exc}} \sqrt{\frac{\pi k_B T_+}{2m\omega_+^2}} \underbrace{\sqrt{\frac{4}{\pi} - \frac{1}{2}}}_{\approx 0.88} := P_2 r_{\text{exc}}. \end{aligned} \tag{4.11}$$

For the expression in the last line, the probability density given in equation (4.9) was evaluated. The constants P_1 and P_2 can be measured in the experiment. For this, the axial frequency shift $\Delta\nu_z$ is measured as a function of the modified cyclotron radius r_+, but for every setting the measurement is repeated multiple

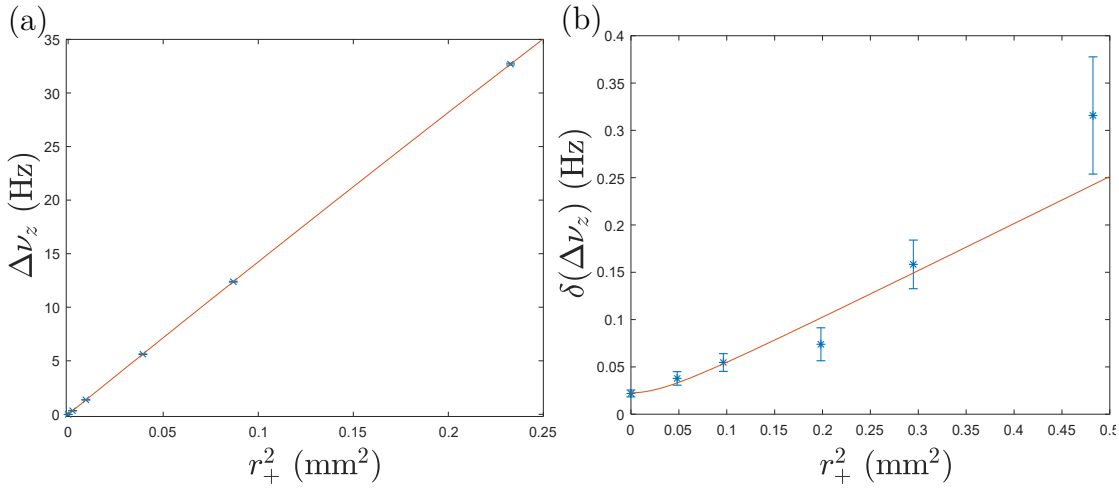

Figure 4.6: Temperature Measurement with a $^{12}C^{4+}$ ion. For this measurement, the trap tuning ratio was detuned by about $3 \cdot 10^{-3}$, resulting in a large C_4. This results in a frequency shift which was measured and is plotted as a function of the modified cyclotron radius squared r_+ in (a). From the fitted slope, the parameter P_1 can be extracted. In (b), the standard deviations of the frequencies for each excitation are plotted together with the fitted function described in the text. This gives the parameter P_2. From both, one can derive an equivalent axial temperature, resulting in $T_z = 1.3(3)\,\mathrm{K}$ for this measurement.

times to be able to extract the spread of measured axial frequencies. This spread or frequency jitter is determined by two parts. A technical part originating in for example voltage fluctuations or the precision of the dip measurement, which is independent[2] from the excitation amplitude and a part originating in the thermal distribution of the ion proportional to the excitation amplitude. Both contributions add quadratically, and one can fit the measured frequency jitter using a function $\delta(\Delta\nu_z) = \sqrt{(P_2 r_{\mathrm{exc}})^2 + P_0^2}$. The frequency shift is fitted with a function $\Delta\nu_z = P_1 r_{\mathrm{exc}}^2 + P_3 r_{\mathrm{exc}}^4$, and the parameter P_1 is extracted. For this method, the excitation and the tuning ratio are chosen such, that the frequency shift described with P_3 is small compared to the one from P_1. From equation (4.11) one can then deduce the temperature using

$$T_+ = \frac{2m\omega_+^2}{\pi k_B} \frac{1}{\frac{4}{\pi} - \frac{1}{2}} \frac{P_2^2}{4P_1^2}. \tag{4.12}$$

Usually, the temperature is given as an equivalent axial temperature, $T_z = \frac{\omega_z}{\omega_+} T_+$. This approach has the advantage, that the physical origin of the frequency shift does not play a role for the determination of the temperature, only the scaling

[2]In principle, large excitation amplitudes can reduce the precision of the dip measurement. For example, the dip can "wash-out" in a large C_4, and a C_4 can be mimicked by a C_6 together with an excited radius, see equation (2.23). However, such effects become significant only at much larger excitation amplitudes than the ones used during temperature measurements.

with r_+^2. However, one can, of course, compare with the values one would expect from the measured field parameters B_2 and C_4.
In figure 4.6, such a temperature measurement with a $^{12}C^{4+}$ ion is shown, resulting in $T_z = 1.3(3)\,\mathrm{K}$. For this measurement, the trap tuning ratio was detuned. Using the simulated value for $D_2 = 0.79$ for the used tuning ratio and the chosen detuning one expects an anharmonicity of $C_4 = 3.43 \cdot 10^{-4}$. Considering this and evaluating equation (4.5), one expects a slope of $152(2)\,\mathrm{Hz\,mm^{-2}}$, where the uncertainty originates in the uncertainty assigned to the compensated value for B_2. The slope in figure 4.6(a) is fitted to $P_1 = 144(1)\,\mathrm{Hz\,mm^{-2}}$. Both values differ by about 5 %. Since an uncertainty of about 10 % for D_2 can be expected [7], the comparison of both values is in good agreement. This crosscheck further strengthens our trust in our model of systematics.
Such temperature measurements were performed at various times during the measurement campaign, with all involved particles and both with and without electronic feedback. One expects the same temperature for all the ions, since the same detection system is used. The measurements scatter slightly more than statistical in the range between 0.7 K and 1.7 K. Such a scatter can in principle occur when electric noise increases the effective temperature of the detection system. Since this scatter was not significant enough to justify assigning different temperatures to different stages of the measurement campaign, we decided to assign a conservative uncertainty to the temperature, which covers this scatter. The final value for the temperatures with and without feedback are then:

$$\begin{aligned} T_{z,\mathrm{FB}} &= 1.2(5)\,\mathrm{K} \\ T_{z,\text{no FB}} &= 3.7(5)\,\mathrm{K}. \end{aligned} \tag{4.13}$$

For the temperature without feedback one expects in principle the ambient temperature of 4.2 K. However, the cryogenic amplifier used intrinsically has some weak negative feedback, which can result in a temperature slightly lower than ambient temperature [52].
Another way to crosscheck the temperature is to compare the resonator parameters with and without feedback. Example spectra for both are shown in figure 4.7. There, the signal-to-noise ratio (SNR) is 19.1 dB without feedback, and 4.3 dB with feedback. If one assumes the temperature without feedback in equation (4.13) as given, the feedback temperature expected from these SNR levels is $T_{z,\mathrm{FB}} = 0.7\,\mathrm{K}$, which is compatible with the direct measurement.

4.5 Aligning the Trap

Prior to the measurement campaign, we used the tilting mechanism to adjust the trap alignment with the magnetic field. To this end, all the available adjustment screws were tightened to maximize the axial frequency. During this process, the following points became clear:

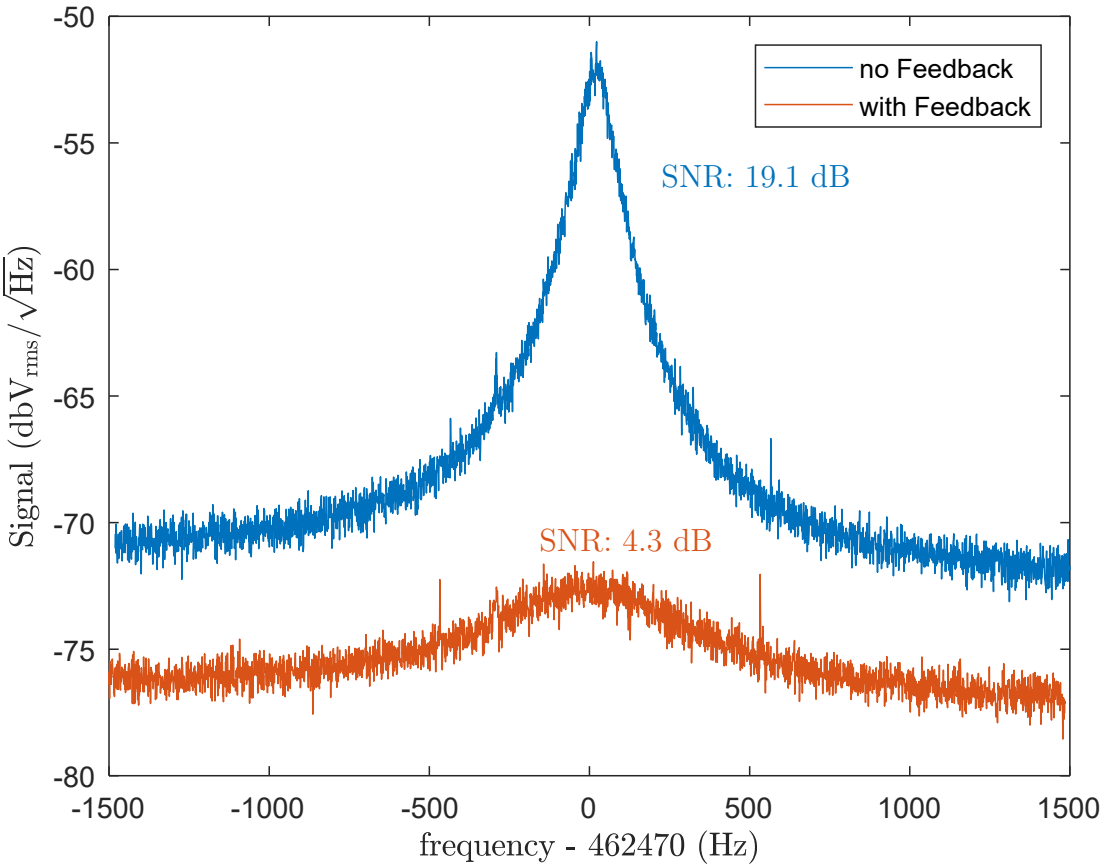

Figure 4.7: Resonator spectrum with and without feedback. Shown are two example spectra of the resonator during the deuteron measurement campaign. The overall level of the signal is decreased by 6 dB when feedback is applied, since the mixer used for the feedback changes impedance depending if there is a local oscillator connected or not. Without feedback, the signal-to-noise ratio (SNR) is about 19.1 dB, with feedback this decreases to 4.3 dB. For a temperature of $T_{z,\text{no FB}} = 3.7\,\text{K}$ one expects from these spectra a feedback temperature of $T_{z,\text{FB}} = 0.7\,\text{K}$, compatible with the direct measurement.

1. Using the tilting mechanism results in significant noise on the detection system. Even after disconnecting the joints, the resonator is shifted to an apparantly random position, up to a few 100 Hz from the original position. This can be explained by changes of the capacitance in the resonator. There, a change of only 0.1 pF relates to a shift of the resonator frequency of about 300 Hz. Since a significant contribution to this capacitance comes from the surfaces of the trap electrodes, such a small change in capacity is expecteded when moving the trap. To measure the axial frequency after using the tilting mechanism, one has to disconnect the joint and adjust the resonator frequency using the varactor.

2. Due to the limited stiffness of the used fiberglass, one can turn the room temperature handles for the adjustment screws by about 90°, before the adjustment screws in the 4 K section start turning. However, one can feel this process fairly well, roughly estimated up to about 30°. Since the adjustment screws have a pitch of 0.8 mm and the distance between the adjustment screws' pressure point and the opposite side of the lower part of the electronic section is 90 mm, this translates into a precision limit of about 0.08°.

3. When trying to loose the adjustment screws, there is a lot of hysteresis involved. The push-back of the springs does not occur smoothly. Therefore, it was best to start in a position with all the screws relaxed, and then only tighten the screws.

In the tilting process before the deuteron measurement campaign, the axial frequency of a $^{12}C^{6+}$ ion shifted by +29.3 Hz out of 461 kHz. Inserting this into equation (2.20b), this corresponds to an angle of $\theta = 0.53°$. During the ICS measurement campaign, an angle of $\theta = 0.56(7)$ was measured [63], in agreement with the value from the axial frequency shift during angle adjustment. Although large portions of the experiment were reworked, this agreement was expected: The most likely sources for this tilt, a misalignment between the magnet's field and bore, or a bending of the stack of Penning-trap electrodes were unchanged. From the measurements taken during the adjustment process we estimate that the maximum of the axial frequency was hit to about 1 Hz. Since the frequency shift scales quadratically with θ, a shift of 1 Hz still corresponds to an angle of about 0.1°, relatable to the limit from the stiffness given above.
To evaluate the situation after the adjustment more closely, one can use equation (2.22), and solve for the trap parameters, which yields

$$\frac{9}{4}\theta^2 - \frac{1}{2}\epsilon^2 = \frac{1}{\omega_-}\left(\omega_+ + \omega_- - \sqrt{\omega_+^2 + \omega_z^2 + \omega_-^2}\right). \tag{4.14}$$

The uncertainty of this expression is dominated by the measurement absolute uncertainty of the magnetron frequency. Therefore, the magnetron frequency was measured using the phase-sensitive method described in [63]. This yields

$$\frac{9}{4}\theta^2 - \frac{1}{2}\epsilon^2 = -4.30(17) \cdot 10^{-5}. \tag{4.15}$$

The value is negative, indicating that the angle θ is at least so small that the contribution by an ellipticity ϵ is dominant. Solving this for ϵ and assuming an angle of 0.05(5)°, one arrives at

$$\epsilon = 9.46(18)^{+0.53}_{-0.18} \cdot 10^{-3}, \tag{4.16}$$

where the uncertainty in brackets comes from the frequency measurement and the asymmetric uncertainty from the uncertainty of the angle.
This is larger than what one would expect from the manufacturing precision of our trap, which is about 10 µm. Compared to the trap diameter of 10 mm, one expects

an ellipticity of $\epsilon \approx 1 \cdot 10^{-3}$. One possible explanation is the fact that the inner electrodes were split in half. With ϵ measured to this level of precision, this will not give a limitation for future measurements of the image charge shift anymore.

4.6 Evaluating Pressure Dependencies

In this section, I present measurements on the impact of pressure changes in the cryo-reservoirs. The measurements are shown in figure 4.8. They were taken with the final pressure stabilization systems as described in section 3.2 operational. For both the LHe and the LN_2 reservoirs, the magnet and the apparatus are connected and stabilized together. To measure the impact on the magnetic field as fast as possible, repeated PnA measurements with an evolution time of $T_{\mathrm{evol}} = 15\,\mathrm{s}$ were performed. Every 10 cycles, a PnA measurement with $T_{\mathrm{evol}} = 10\,\mathrm{ms}$ was performed to exclude a possible impact of voltage fluctuations on the measurement. In this way, one can potentially measure relatively fast and with a high resolution. However, the absolute frequency is not resolved, and for fast changes it is possible to make mistakes of multiples of 360°.
In figure 4.8(a), a relatively small change of 0.5 mbar resulted in a change of the modified cyclotron frequency of about −50 mHz. Note, that at this measurement time, a frequency jump of 67 mHz corresponds to a phase shift of 360°. Therefore, it would also be possible that the frequency jump is in reality only +17 mHz. If one assumes the worse case of −50 mHz, this translates into a pressure dependency of $\approx 100\,\mathrm{mHz/mbar}$. For the pressure fluctuations evaluated in section 3.2 of 4 µbar, one arrives at a frequency jitter of $\delta\nu_+/\nu_+ = 1.4 \cdot 10^{-11}$. With this stability, pressure fluctuations in the LHe reservoir do not play a role for the statistical resolution of mass measurements anymore.
When changing the pressure by a larger amount as in figure 4.8(b) or even more extreme in (c), one cannot rely on the absolute value of the frequency anymore, as errors of multiples of 360° become increasingly probable. However, it becomes clear that not only the frequency changes as a function of the pressure, but that also drifts after changing the pressure value occur. A possible explanation would be that the changed helium boil-off rate changes the temperature of the helium filling tube, which also mechanically supports the experiment. This can result in a changed position of the trap and thus a changed magnetic field. As the boil-off rate is in first order independent of the pressure, one mostly expects the derivative of the pressure to play a role for this effect. When one goes to a higher set point for the pressure, the valve closes, no helium can boil off. When going for a lower set point, the valve opens and a lot of helium starts to boil. Therefore, one expects large pressure changes, where the boil-off rate changes significantly, to behave differently than small pressure changes. However, one should keep in mind that the level of LHe in the magnet might also alter the temperature gradient in the boil-off tube. As the level is not stabilized at the moment, this might also lead to drifts in the magnetic field, which needs to be investigated in the future.
In the position marked as (I) in figure 4.8(b), an automatic measurement of the liq-

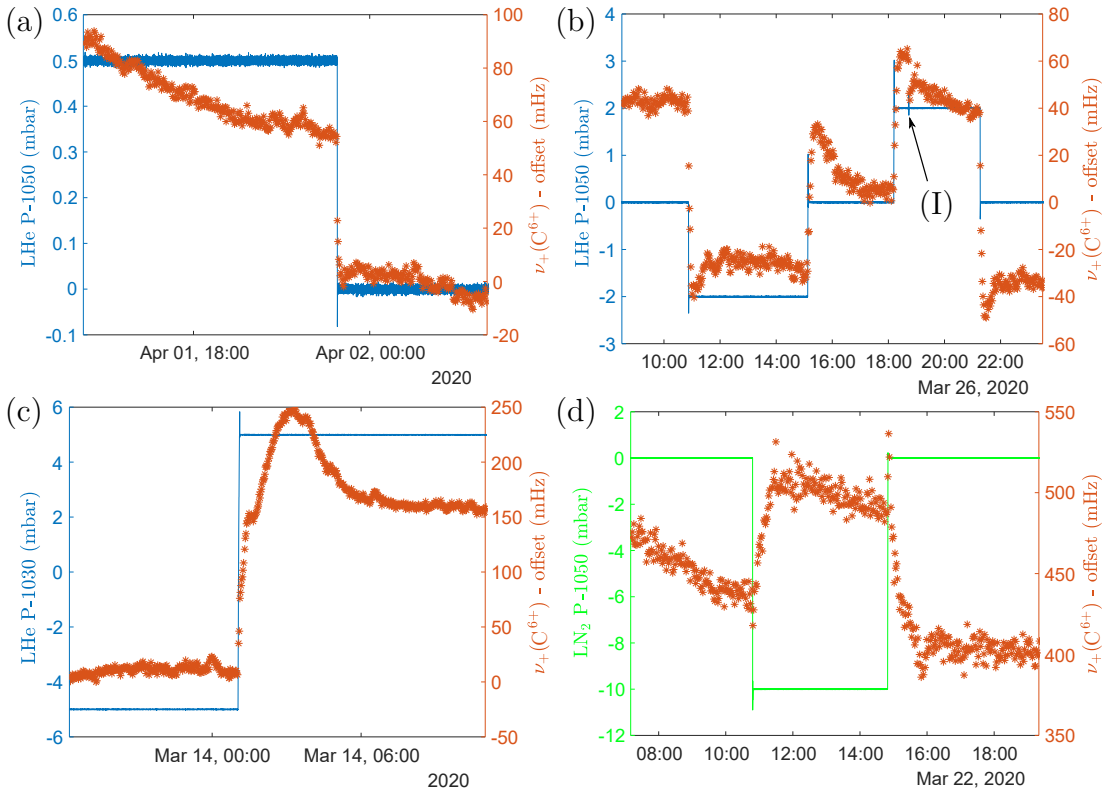

Figure 4.8: Pressure dependencies measured with $^{12}C^{6+}$. On the left y-axis, the absolute pressure in (mbar) for the LHe reservoir (a-c) or the LN_2 reservoir (d) is given. The frequency shift is measured by subsequent PnA measurements with $T_{\mathrm{evol}} = 15\,\mathrm{s}$, therefore, the offset on the right y-axis is not resolved, and 360° errors can occur. In the spot marked as (I) in (b), an automatic measurement of the LHe reservoir took place, clearly resulting in a frequency response. For details, see text.

uid helium level in the magnet reservoir took place, clearly resulting in a frequency jump and a subsequent drift back. These measurements occur approximately once a day and are at the moment not controlled by our control system. They potentially constitute a form of non Gaussian frequency jitter and need to be taken care of in the future.

In figure 4.8(d), a similar measurement with the LN_2 reservoir is shown, during which the LHe reservoir was stabilized as well. There, a pressure change of $-10\,\mathrm{mbar}$ leads to a frequency change of 85 mHz. The impact of pressure fluctuations in the LN_2 reservoir with $\approx 8.5\,\mathrm{mHz/mBar}$ is much smaller than for the LHe reservoir. Therefore, one does not expect pressure fluctuations in the LN_2 reservoir to pose a limit for the statistical precision of mass measurements, as long as the reservoir is stabilized. However, the stabilization is needed, as atmospheric pressure changes over several mbar can occur.

4.7 Transistor Board

The transistor board introduced in section 3.4.3 is supposed to use the freeze-out of silicon based transistors to separate the voltage supply from the ST1 electrodes in order to improve the voltage stability. To significantly beat the stability of the currently used UM1-14, one would need a voltage stability of better than $1 \cdot 10^{-7}$.

In order to test this, the transistor board was heated first. In this manner, the voltages applied to the electrodes are not hindered by the transistors, in this state they have a resistance of about 150 Ω. Then, a single $^{12}C^{6+}$ ion was transported into this trap. It was in resonance with the detection circuit at a voltage of −5.43 V at a resonance frequency of $\nu_z \approx 600.9$ kHz. While the transistor board was heated, the dip was only barely visible, because fast mode channels of the UM1-14 with insufficient voltage stability were used to bias the electrodes in the ST1. We stopped heating the transistor board and after a few minutes the dip became visible much more clearly, indicating that the transistor board works to some degree. We proceeded to do a long time measurement of the axial frequency, which is shown in figure 4.9. There are large drifts in particular in the first few hours after the measurement started. These drifts could be a result of the heating, which was only removed shortly before, or be a result of leakage currents.

The linear drift in the first two hours of the measurement corresponds to a voltage drift of the ring electrode of about $1.6 \cdot 10^{-7}\,\mathrm{V\,s^{-1}}$, if one would assume the other voltages to be constant. Since the capacitance after the transistor is about 22 nF, this corresponds to a leakage current in the order of 3.5 fA, or a leakage resistance of $R = 1.5 \cdot 10^{15}\,\Omega$. In a test setup, the resistance of the frozen-out transistor was measured to be $> 500\,\mathrm{G\Omega}$, which proved to be true also in the trap. It should be noted, that such a leakage could realistically come from the 22 nF capacitance. The capacitance's insulation resistance is rated for room temperature to be $> 3\,\mathrm{G\Omega}$ [82], which one expects to increase significantly at cryogenic temperatures.

In figure 4.9, three spots are marked where the trap voltage was changed. For small voltage changes in the mV range as in (I) and (II), no frequency shift was observed, although a change of 1 mV corresponds to an expected frequency shift of 55 Hz. The transistor board shields the voltage change from the electrode as intended. Since there is no change in the axial frequency drift visible, leakage currents through the transistor are at least much smaller than the other leakage currents described above. At the position marked as (III), the ring voltage was changed by 0.5 V, which should change the axial frequency by 27 kHz. However, the observed frequency jump is only about 2.5 Hz, corresponding to a voltage change at the electrode of $4.5 \cdot 10^{-5}$ V. This can be explained by modeling the transistor as a very small parasitic capacity of about 17 fF. Again, no change in the drift was observed, confirming the lack of leakage currents through the transistor seen before.

In conclusion, the transistor board works as intended. However, the intended use as a voltage stabilization is prohibited by leakage currents in the capacitance or the electrode. In the future, this might be solved by using capacitors with less

leakage, for example by using vacuum gap capacitors, for which leakage currents corresponding to a resistance $> 10^{19}\,\Omega$ were reported [83]. Because of these too large leakage currents, the transistor board was not used during the deuteron measurement campaign. To avoid undefined voltages, the transistors were heated constantly. While the intended use of the transistor board is at the moment not possible, the successful test of the transistor as a switch opens up further applications like the use as a high fidelity switch to add capacitance to a resonator will be investigated.

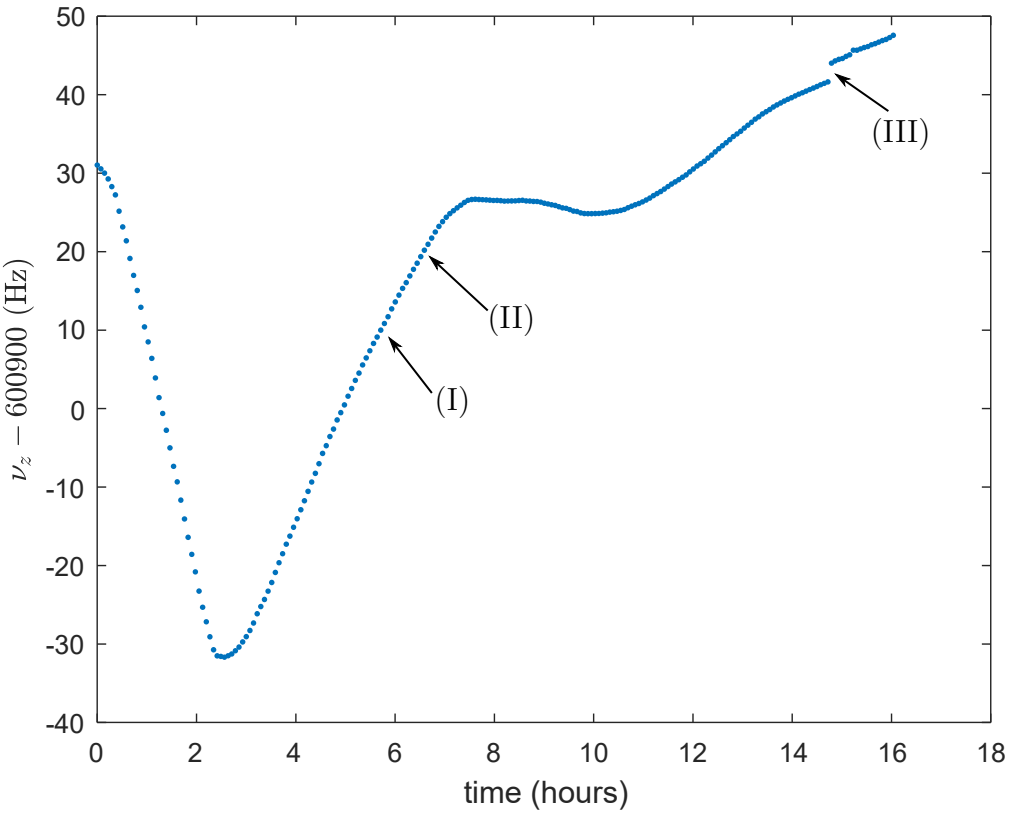

Figure 4.9: Performance of the transistor board. The axial frequency of a $^{12}C^{6+}$ ion, after heating of the transistor board was stopped, is plotted as a function of time. The frequency drifts significantly, more towards the start of the measurement. At the position marked with (I), the voltage channels connected to the inner trap electrodes were changed by $\approx 7\,\mathrm{mV}$. For this voltage change, one expects a frequency shift of $\approx 390\,\mathrm{Hz}$. At (II), the voltage source was switched into "shutdown" mode, resulting in a voltage change of similar order to the channels connected to the endcaps. For both changes, there was no jump in the axial frequency visible. At (III), the voltage of the channel connected to the ring electrode was changed from $-5.423\,\mathrm{V}$ to $-5.923\,\mathrm{V}$, resulting in a frequency jump of $\approx 2.5\,\mathrm{Hz}$. For details see text.

5 Deuteron Measurement Campaign

In this chapter, I describe the measurement campaign on the deuteron's atomic mass in detail. The results of this campaign are also published in [6]. In the following I start with an explanation of the measurement principle, followed by a description of the measurement cycle in section 5.2.

5.1 Measurement Principle

The measurement principle of mass measurements in Penning traps is based on a comparison of the cyclotron frequency $\omega_c = \frac{q}{m}B$. Building the ratio of the cyclotron frequencies of the ion of interest and a reference ion and solving for the mass of the ion of interest yields

$$m(d) = \frac{1}{6}\underbrace{\frac{\omega_{c,d}}{\omega_{c,^{12}\mathrm{C}^{6+}}}}_{=:R} m(^{12}\mathrm{C}^{6+}). \tag{5.1}$$

Here I give this formula for the deuteron as the ion of interest, and a $^{12}\mathrm{C}^{6+}$ ion as a reference, with cyclotron frequencies $\omega_{c,d}$ and $\omega_{c,^{12}\mathrm{C}^{6+}}$, respectively. The charges give a ratio of integers, in this case 1/6. The reference ion is chosen such that its mass m in atomic mass units is well known, see also section 5.3. The frequency ratio R is the quantity which needs to be measured in the experiment.
It is important to note that in order to get equation (5.1), one has to assume that both ions are measured in the same magnetic field B. This ideal measurement condition is very hard to fulfill in practice, since the ions will interact via Coulomb interaction, which results in large systematic shifts. One measurement where this difficulty was overcome was performed at the MIT [81, 84, 67], where two ions in the same trap were prepared in a common magnetron orbit. However, this technique only works for ion pairs with very similar charge-to-mass ratios. The difference between deuteron and $^{12}\mathrm{C}^{6+}$ in charge to mass ratio makes the use this technique very tricky, which is why we decided against using it for now.
At LIONTRAP, we approximate the ideal measurement condition by preparing the ion of interest and the reference ion at the same time in our trap tower, but in separated traps. In this manner, the ions can be measured one after the other in the PT. The measurement cycle is optimized such that the ν_+ measurements, which are most susceptible to magnetic field drifts, are measured as close by as possible, see section 5.2. In principle it is not necessary to keep the electric potential identical for both ions, because it drops out in the invariance theorem. Measurements, where

the electric potential was altered to bring the axial frequency of ions with different charge-to-mass ratio in resonance with the same resonator have been performed in the past [20, 18]. However, a change of the electric potential typically leads to shifts of the ion's equilibrium position due to patch potentials, which causes the ion to probe a different magnetic field. Such a shift is very hard to control, since even very small changes of 20 nm can lead to relative magnetic field shifts in the order of $1 \cdot 10^{-11}$. Therefore, we have decided to keep the trapping potential constant for both ions, and to shift the resonator's frequency using a varactor diode.

5.2 Measurement Cycle

The measurement cycle is essentially unchanged from the one used in the proton mass campaign [7, 8] and the same for both the measurements of the deuteron and the HD^+, respectively. The data is taken in *runs*. For each run, the settings, such as the used trap voltages or the excitation amplitudes during the PnA, are kept fixed. In the beginning of the run, the resonator spectra are taken and the precision voltages as well as all the bias voltages are set. The ion to be measured first is chosen randomly. If the chosen ion is not already in the PT, it is transported there and the other ion is stored in its storage trap. In the PT, the first ion's motional modes are thermalized with the tank circuit (precooling) and its frequencies are measured. This starts with a measurement of the modified cyclotron frequency ν_+ with the double-dip method. While the result of this measurement does not enter the final mass value due to its large systematic uncertainties, the resulting value for ν_+ is used as a starting point for the PnA measurement. After the double dip measurement, the axial frequency ν_z is measured with the dip method, followed by a ν_+ measurement with the PnA method. There, the measurements with a shorter evolution time T_{evol} are performed first, since they are less prone to magnetic field drifts. Afterwards, the ions are exchanged, i.e. the first ion is transported into a storage trap and the second ion is transported into the PT, where the measurements are repeated in inverse order. For the next cycle, the starting ion is again chosen randomly, and a transport occurs only if the chosen ion is not already in the PT. This measurement cycle is visualized in figure 5.1. A run typically contains 27 frequency ratios and spans the time between two fillings of the liquid Helium reservoir, which is typically $2 - 3$ days.
The length of the longest evolution time during the PnA was varied between 20 and 30 seconds. Both for this maximum evolution time and for the starting phase taken at an evolution time of 10 ms, six measurements each were taken. To unwrap the phases, measurements at evolution times of 0.5 s, 1 s, 2 s, 5 s and 10 s were performed. For the double dip and dip measurements, the average times were between 205 s and 270 s, respectively. There, FFT spectra with a length of 32.8 s were used, corresponding to a bin-width of ≈ 30 mHz. Between 6 to 8 of these were averaged to improve the visibility of the dip. The precooling times were chosen to be relatively long, 30 s for the magnetron motion and 60 s for the modified cyclotron motion. This is because they also served as a settling time for

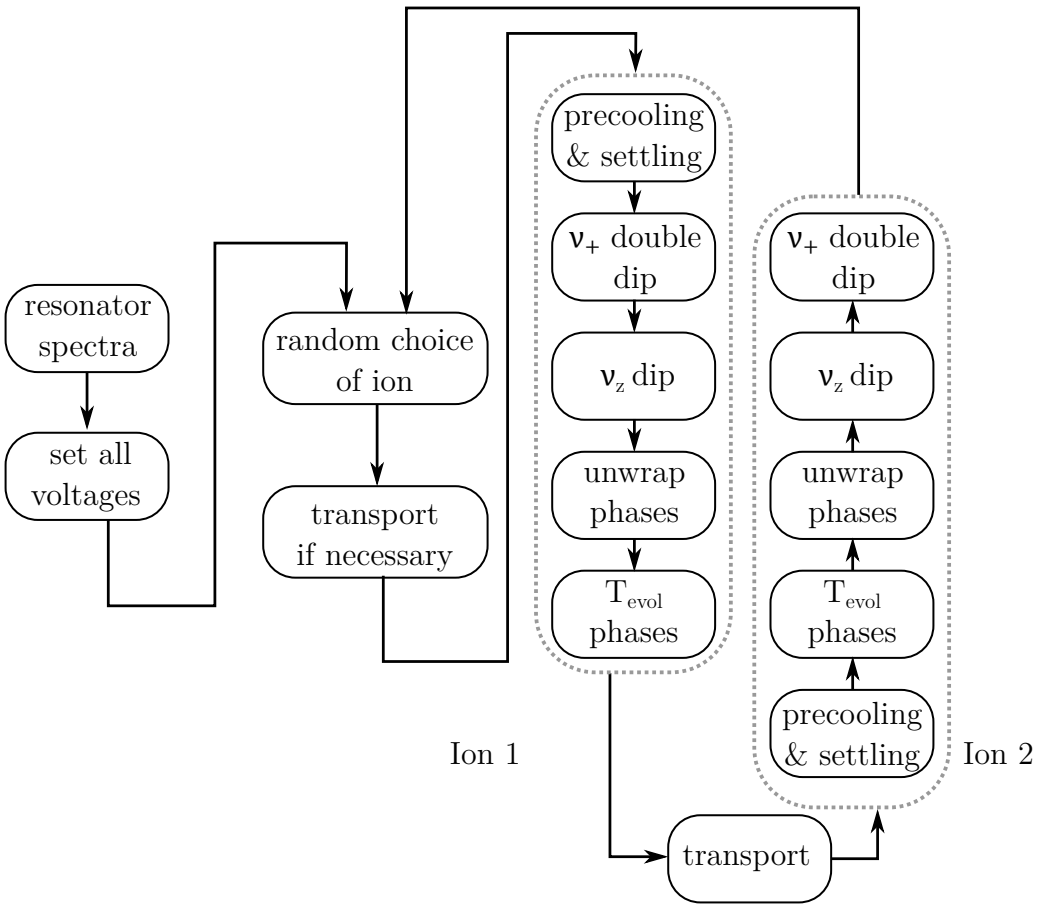

Figure 5.1: Illustration of the measurement cycle. In the beginning of each run, the spectra of the empty resonators are taken and the trap parameters such as the used voltages are set. The first ion is chosen randomly and transported into the PT, where its frequencies are measured after precooling its motional modes and waiting for the voltage to settle after transport. Afterwards, the other ion is transported into the PT, and the measurements are performed in reversed order, such that the most critical ν_+ measurements are close together and thus the impact of magnetic field drifts is minimized. This cycle is repeated typically until the liquid helium reservoir needs to be filled, which occurs every $2-3$ days. For further details see text.

Table 5.1: Ionization energies of carbon. The values are given in eV and are taken from [86].

Ionization energy	Value in eV
I	11.260 2880 (11)
II	24.383 154 (16)
III	47.887 78 (25)
IV	64.493 52 (19)
V	392.090 515 (25)
VI	489.993 194 (7)

the voltages to settle again after transport. For the last pair of particles used in the deuteron campaign, these cooling times were reduced to both 5 s to explicitly search for effects of the voltage settling.

5.3 Deuteron Mass

For the deuteron measurement campaign, a $^{12}C^{6+}$ ion was used as a reference mass. The mass of this ion can be given in atomic mass units using the formula

$$\begin{aligned} m(^{12}C^{6+}) &= 12 - m_e + \sum_{i=1}^{6} B_i \\ &= 11.996\,709\,626\,412\,46\,(35)\,\text{u}. \end{aligned} \tag{5.2}$$

Here, $m_e = 5.485\,799\,090\,65\,(16) \cdot 10^{-4}$ u is the electron mass in atomic mass units [85], and B_i is the atomic binding energy of the electron with index i [86]. The binding energies are summarized in table 5.1. The fractional uncertainty of the mass of $^{12}C^{6+}$ in atomic mass units is only 0.03 ppt and thus does not limit the precision of the deuteron mass given in atomic mass units.
The data set consists of four pairs of ions. For the first pair of ions, the deuteron was above the $^{12}C^{6+}$ ion, for the other ion pairs this was reversed in order to check for systematic effects. For the first two ion pairs, the excitations were generated by a dual channel arbitrary waveform generator Keysight 33600A 80 MHz (AWG1). For the second pair of ions, an Agilent 33522A 30 MHz (AWG2) was used. Both data sets were statistically evaluated separately.

5.3.1 Statistical Evaluation

For the statistical analysis, for each run the resonator parameters were fitted. These fixed resonator parameters were used for a fit of the dip and double dip. The phases in the PnA measurement are unwrapped and analyzed. Where this is not unambiguously possible or the fit does not converge properly, the cycle is excluded from the analysis.

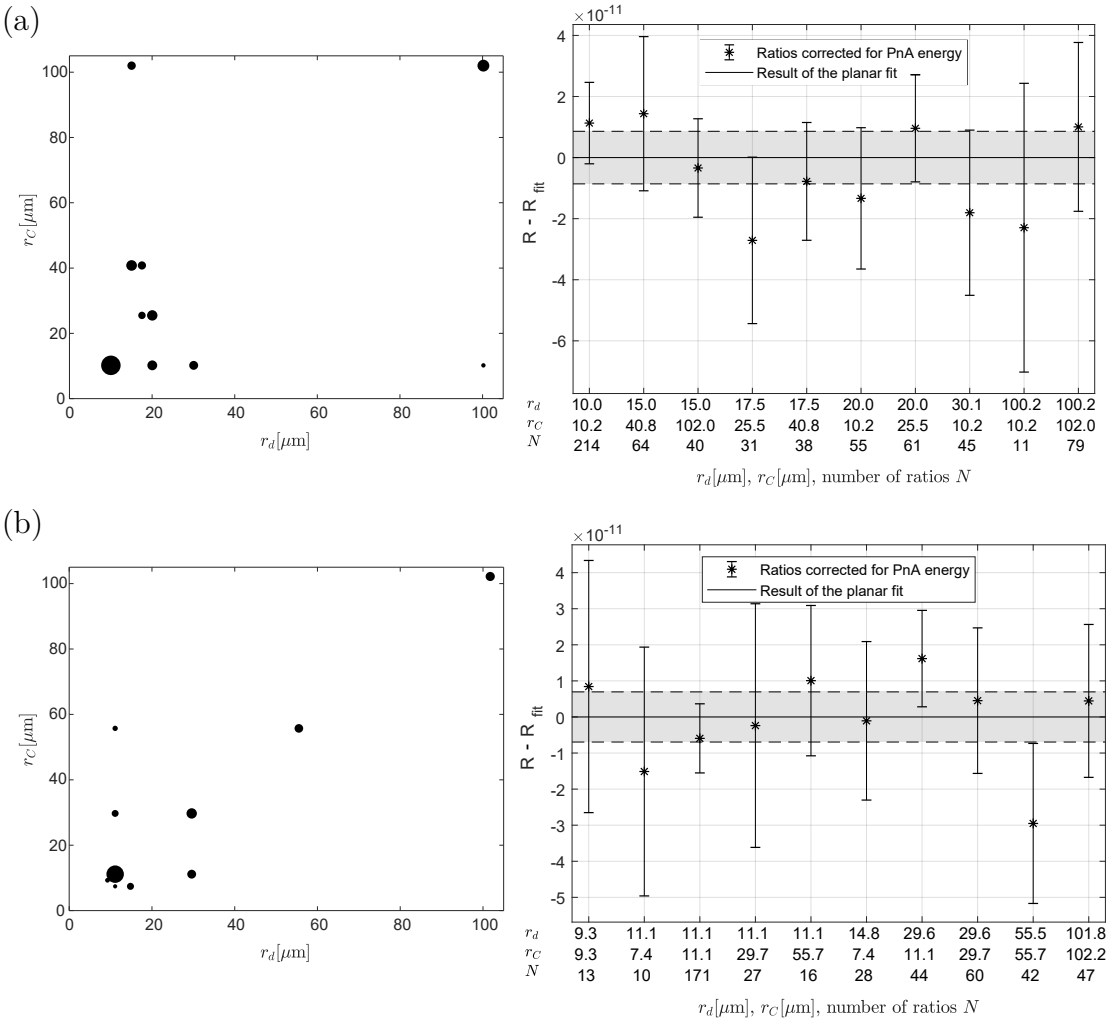

Figure 5.2: Surface fit for deuteron measurement campaign. In (a), data for the AWG1 is shown, in (b) for AWG2. The scatter plot on the left indicates the excitation radii used. The area of the circles is proportional to the number of cycles N taken at this excitation. This number, together with the corresponding excitation radii, is also given on the x-axis of the plot on the right side. There, the residuals of the surface fit are shown. The gray band corresponds to the 1σ confidence level of R_0 extracted from the fit.

In the measurement campaign, different excitation energies during the PnA measurement and thus different motional amplitudes of the ion were probed, resulting in a variation of the relativistic shift during the PnA measurement. Rather than treating this as a systematic uncertainty, we used a method we call *surface fit*, already employed during the proton mass campaign [7]. To this end, runs with equal excitation settings were grouped. For each of these groups, a value for the frequency ratio $R = \nu_c(^{12}\mathrm{C}^{6+})/\nu_c(d)$ was generated by taking the mean $\bar{R}$ over the individual ratios R_i. The associated uncertainty was estimated by building the standard error of the mean,

$$\delta R = \sqrt{\frac{1}{n-1}\sum_{i=1}^{n}(R_i - \bar{R})}, \tag{5.3}$$

where n is the number of ratios in this group. Since the relativistic shift scales with the energy in the modified cyclotron mode, the expected frequency ratio is a linear function of both the squared excitation strength of the deuteron and the $^{12}\mathrm{C}^{6+}$, as can be seen from the following calculation:

$$\begin{aligned}
R &= \frac{\nu_c(^{12}\mathrm{C}^{6+})}{\nu_c(d)} \\
&= \frac{\nu_{c,0}(^{12}\mathrm{C}^{6+}) + \Delta\nu_c(^{12}\mathrm{C}^{6+})}{\nu_{c,0}(d) + \Delta\nu_c(d)} \\
&\approx \frac{\nu_{c,0}(^{12}\mathrm{C}^{6+})}{\nu_{c,0}(d)}\left(1 + \frac{\Delta\nu_c(^{12}\mathrm{C}^{6+})}{\nu_{c,0}(^{12}\mathrm{C}^{6+})} - \frac{\Delta\nu_c(d)}{\nu_{c,0}(d)}\right) \\
&= R_0 - R_0\frac{\omega_{+,C}^4 r_+^2(^{12}\mathrm{C}^{6+})}{2c^2(\omega_{+,C} - \omega_{-,C})^2} + R_0\frac{\omega_{+,\mathrm{d}}^4 r_+^2(d)}{2c^2(\omega_{+,d} - \omega_{-,d})^2} \\
&= R_0 + aA^2(^{12}\mathrm{C}^{6+}) + bA^2(d).
\end{aligned} \tag{5.4}$$

Here, A is the dipolar excitation strength during the PnA measurement, where $r_+ = \kappa_+ A$, see also section 4.3.2. For the frequency shift $\delta\nu_c$, the expression for the relativistic frequency shift in equation (2.71) was used, which is dominant for excitations in r_+, and $\delta\nu_c/\nu_c \approx \delta\nu_+/\nu_+$. For the highest used excitations amplitudes of $r_+ \approx 100\,\mu\mathrm{m}$, the shift is in the order of $1.9 \cdot 10^{-9}$, which justifies neglecting higher orders. One can fit a plane to the tuples $(A_i(^{12}\mathrm{C}^{6+}), A_i(d), R_i)$, where i denotes the grouped runs mentioned above. From this planar fit, one can extract the frequency ratio extrapolated to zero excitation energy R_0. Additionally, the coefficients a and b can be used as a cross check by comparing them to the dedicated κ_+ measurements performed prior to the measurement campaign. This surface fit has to be performed for the data with the two arbitrary waveform generators separately. In figure 5.2, the residuals of this surface fit for both data sets are shown, together with a scatter plot indicating the excitation radii used. The resulting frequency ratios are:

$$\begin{aligned}
R_{\mathrm{AWG1}} &= 1.007\,052\,737\,831\,3\,(86) \\
R_{\mathrm{AWG2}} &= 1.007\,052\,737\,831\,8\,(70).
\end{aligned} \tag{5.5}$$

Table 5.2: Calibrations of the excitation strength from the surface fits.

	slope ($1/\mathrm{Vpp}^2/\mathrm{sec}^2$)	κ_+ surface fit (m/Vpp/sec)	κ_+ direct (m/Vpp/sec)
AWG1, $^{12}C^{6+}$	$-1.198\,(12)\cdot 10^{-4}$	$2.547\,(13)\cdot 10^{-2}$	$2.515\,(62)\cdot 10^{-2}$
AWG1, d	$1.155\,(18)\cdot 10^{-4}$	$2.518\,(20)\cdot 10^{-2}$	
AWG2, $^{12}C^{6+}$	$-6.38\,(24)\cdot 10^{-5}$	$1.858(37)\cdot 10^{-2}$	
AWG2, d	$6.24\,(25)\cdot 10^{-5}$	$1.850(35)\cdot 10^{-2}$	$1.904\,(62)\cdot 10^{-2}$

Both values agree well within their uncertainties. Since one also does not expect a systematic difference here, we averaged both values, resulting in our statistical ratio

$$R_{\mathrm{stat}} = 1.007\,052\,737\,8316\,(54). \tag{5.6}$$

Using the slopes taken from the surface fit and equation (5.4) results in new values for κ_+. These are summarized in table 5.2 and compared with direct measurements, of which one was presented in more detail in section 4.3.2. Since the frequencies of deuteron and $^{12}C^{6+}$ are relatively close together and the excitation lines at LIONTRAP are designed such that there are no sharp resonances in the transfer function, one expects the κ_+ to be very similar for both deuteron and $^{12}C^{6+}$. This is the reason, why the direct measurement was for each arbitrary waveform generator performed only for one ion species. Indeed, the κ_+ values resulting from the surface fit are very similar for both ions. For AWG1, the difference between the values is about 0.6% corresponding to $1.2\,\sigma$. Both values agree with the less precise direct measurement on a $1\,\sigma$ level. For AWG2, the uncertainties are slightly larger, since no points with very asymmetric radii were taken (see figure 5.2(b)). Within the uncertainties, both values agree with each other and with the direct measurement on a $1\,\sigma$ level. Between both arbitrary waveform generators, the values differ significantly. This is an effect of a lower sampling rate of the AWG2, which resulted in the actual output voltage being smaller than the nominal value. The observed difference stresses the importance of treating the data sets separately.

5.3.2 Evaluation of Systematic Shifts

The frequency ratio R_{stat}, derived in the way described above, is the extrapolation of the ratio measured with PnA to zero cyclotron excitation energy. This extrapolation contains any (known and unknown) shifts that are linear in the excitation energy. However, there are still a number of relevant systematic shifts which need to be accounted for. These shifts are, together with their respective uncertainties, summarized in table 5.3.
The by far biggest shift is the image charge shift, which is treated in section 2.7.2. However, this shift can be corrected for with an uncertainty of 5 % of the absolute

value of the shift, resulting in a relative uncertainty of the frequency ratio $\delta R/R = 4.1 \cdot 10^{-12}$. The entry *Special relativity (thermal)* corresponds to the thermal energy in the modified cyclotron mode before excitation. While the excitation radius is accounted for with the surface fit, the thermal radius still leads to a residual relativistic shift. Due to the inverse scaling with mass, this effect affects mostly the deuteron, rather than the heavier carbon ion. With the temperature given in section 2.4, this evaluates to a shift of the frequency ratio of −2.9 ppt, and an uncertainty of 1.2 ppt.

The term associated with *Magnetic inhomogeneity* was the dominating uncertainty in the measurement of the proton's atomic mass. As described in section 3.6, the finite axial amplitude due to the ion's thermal energy, combined with a magnetic inhomogeneity B_2, leads to a frequency shift. By using the newly developed shim coil, it was possible to reduce this shift and the corresponding uncertainty to 0.3(6) ppt. It is thus small enough to not play a significant role in the systematic evaluation of this measurement. The electrostatic anharmonicity represents the uncertainty coming from the residual C_4 and C_6 terms evaluated in section 4.2. The uncertainty of 0.4 ppt is negligible compared to other systematic uncertainties. This small value also justifies taking one global value for C_4 and C_6 rather than individual measurements for each ion pair, since the expected dependency of the frequency ratio is much smaller than the statistical variation between measurements. In the analysis, the contributions special relativity, magnetic inhomogeneity and electrostatic anharmonicity were considered taking correlations into account.

The main contribution to the systematic uncertainty of the dip measurement originates from the uncertainty of the resonance frequency of the resonator. The transfer function of the amplifier chain is in section 2.2.2 approximated to have a linear frequency dependence. In reality this is more complex. Therefore, varying the range included in the fit leads to a variation of the LC circuits fitted resonance frequency. By varying the fitted range between 500 Hz, where the noise floor is not yet completely reached, and 2000 Hz, where a significant part of the spectrum consists of the noise floor, we found a conservatively estimated uncertainty of 2 Hz on the resonator frequency ν_{res}. Evaluating the dependency of the dip fitting result on this parameter for a number of example spectra throughout the campaign led to a dependency of

$$\begin{aligned} \Delta\nu_{z,\mathrm{C}} &= -3.2\,\mathrm{mHz\,Hz^{-1}}\ \Delta\nu_{\mathrm{res}} \\ \Delta\nu_{z,d} &= -1.0\,\mathrm{mHz\,Hz^{-1}}\ \Delta\nu_{\mathrm{res}} \end{aligned} \tag{5.7}$$

for $^{12}\mathrm{C}^{6+}$ and deuteron, respectively. Here, $\Delta\nu_{\mathrm{res}}$ is the difference between the resonator frequency entered as parameter of the fitting routine and the resonator frequency taken from the resonator spectrum. The relevant quantity for the dip width is q^2/m, which is $e^2/(2\mathrm{u})$ for the deuteron and $6\,e^2/\mathrm{u}$ for $^{12}\mathrm{C}^{6+}$, leading to this asymmetry. While in principle the uncertainty of this shift should cancel, because the sign in equation (5.7) is equal for both particles, we decided against including this correlation into our analysis. Although the resonator at both the varactor settings for $^{12}\mathrm{C}^{6+}$ and deuteron is fitted with the same frequency range

Table 5.3: Systematic shifts and their uncertainties after extrapolation to zero excitation amplitude. All values are relative and in parts-per-trillion. For details see text.

Effect	Shift of ν_c for d	Shift of ν_c for $^{12}C^{6+}$	Correction to R^{CF}	Uncertainty
Image charge	−16.6	−98.7	82.1	4.1
Special relativity (thermal)	−3.4	−0.6	−2.9	1.2
Magnetic inhomogeneity	0.4	0.1	0.3	0.6
Electrostatic anharmonicity	0	0	< 0.1	0.3
Dip lineshape	0	0	0	4.7
Magnetron frequency	0	0	0	0.4
Total	−19.6	−99.2	79.6	6.5

and the frequencies are relatively close together, there is no guarantee for the transfer functions to be equal, and we wanted to give a conservative estimate of this uncertainty. The relative uncertainty for the cyclotron frequency was then calculated as

$$\frac{\delta\nu_c}{\nu_c} = \frac{\nu_z \delta\nu_z}{\nu_c^2} \tag{5.8}$$

for both ions, where $\delta\nu_z$ is taken as the full shift one would expect according to equation (5.7) for a fit with a resonator frequency parameter, which is 2 Hz off the correct value. Then, the absolute values of the two respective uncertainties are summed linearly. This systematic effect does not lead to any shift, however, using the calculations outlined above it results in a systematic uncertainty on the frequency ratio of 4.7 ppt. The dip lineshape together with the image charge shift give the dominating systematic uncertainties of the deuteron measurement campaign.

The last systematic effect listed in table 5.3 is the magnetron frequency. The magnetron frequency was not measured every cycle, but at various points during the measurement campaign using the double-dip method. Since the magnetron frequency is only $\nu_- \approx 3.7\,\mathrm{kHz}$, the corresponding sideband frequency $\nu_z + \nu_-$ is very close to the axial frequency. The coupling can thus potentially heat the axial motion and influence the amplifier chain. This made it necessary to measure the magnetron frequency at different coupling strengths and to linearly extrapolate to zero excitation energy. It is important to notice that fluctuations of the magnetron frequency affect both ions, and thus drop out in the cyclotron frequency ratio to a large extend, which is why the magnetron frequency does not need to be monitored constantly. It turns out, that the difference between the magnetron frequencies of both ions is much more relevant for the cyclotron frequency ratio than the magnetron frequencies themselves. In the ICS campaign, the difference between the magnetron frequencies of a single proton and a single $^{12}C^{6+}$ ion were measured

and compared with theory on a sub mHz level [63]. Utilizing such a measurement or a theory value for the magnetron frequency would eliminate the magnetron frequency as a systematic effect for the deuteron measurement campaign. Such data were taken after the deuteron measurement campaign and were partly used in this thesis in section 4.5. However, for the deuteron measurement campaign, these data were not available yet. We decided against using a theory value and stuck to the double dip measurement. The measurement of the magnetron frequency using the double dip resulted in a conservatively estimated uncertainty on the difference of the magnetron frequencies of 0.1 Hz, which translates into an uncertainty of the cyclotron frequency ratio of 0.4 ppt.
When applying all these systematic corrections, one arrives at the final frequency ratio

$$R_{\text{final}} = 1.007\,052\,737\,9117\,(54)_{\text{stat}}(65)_{\text{sys}}(85)_{\text{tot}}, \tag{5.9}$$

where the brackets denote the statistical, systematic and combined uncertainty, respectively.

5.3.3 Final Mass Value

This frequency ratio can be used together with equation (5.1) to obtain the atomic mass of deuteron m_d, resulting in

$$m_d = 2.013\,553\,212\,535\,(11)_{\text{stat}}(13)_{\text{sys}}(17)_{\text{tot}}\,\text{u}. \tag{5.10}$$

With a relative precision of 8.5 ppt, this is to my knowledge the most precise mass measurement in atomic mass units. In figure 5.3, this value is compared with other high-precision values available for the deuteron's atomic mass. The previous most precise value for the deuteron's atomic mass was reported by the University of Washington (UW) [18], with a relative precision of 20 ppt. The value reported in this work is a factor of 2.4 more precise and deviates by $4.8\,\sigma$ or $210\,(43)$ pu (combined uncertainty) from the value reported by the UW, which was also giving the CODATA literature value since the 2014 adjustment [85, 88]. The deuteron mass can also be obtained by combining a recent deuteron-to-proton mass ratio reported by the Florida State University [87] with a proton mass value. If one uses the LIONTRAP value [7] for this, the resulting value for the deuteron mass agrees with the one reported in this work on a $1\,\sigma$ level. However, the deviation from the UW value is about $1.9\,\sigma$ and hence not conclusive. When inserting the current CODATA literature value [85] for the proton's atomic mass, which has a slightly increased uncertainty, the resulting deuteron mass agrees with both the UW and the LIONTRAP value on a $1\,\sigma$ level.
The mass of deuterium $m(\text{D})$ can be derived by adding the electron mass [85] and the ionization energy [86]. This yields

$$m(\text{D}) = 2.014\,101\,777\,842\,(17)\,\text{u}, \tag{5.11}$$

where the uncertainty is dominated by the uncertainty of the deuteron mass.

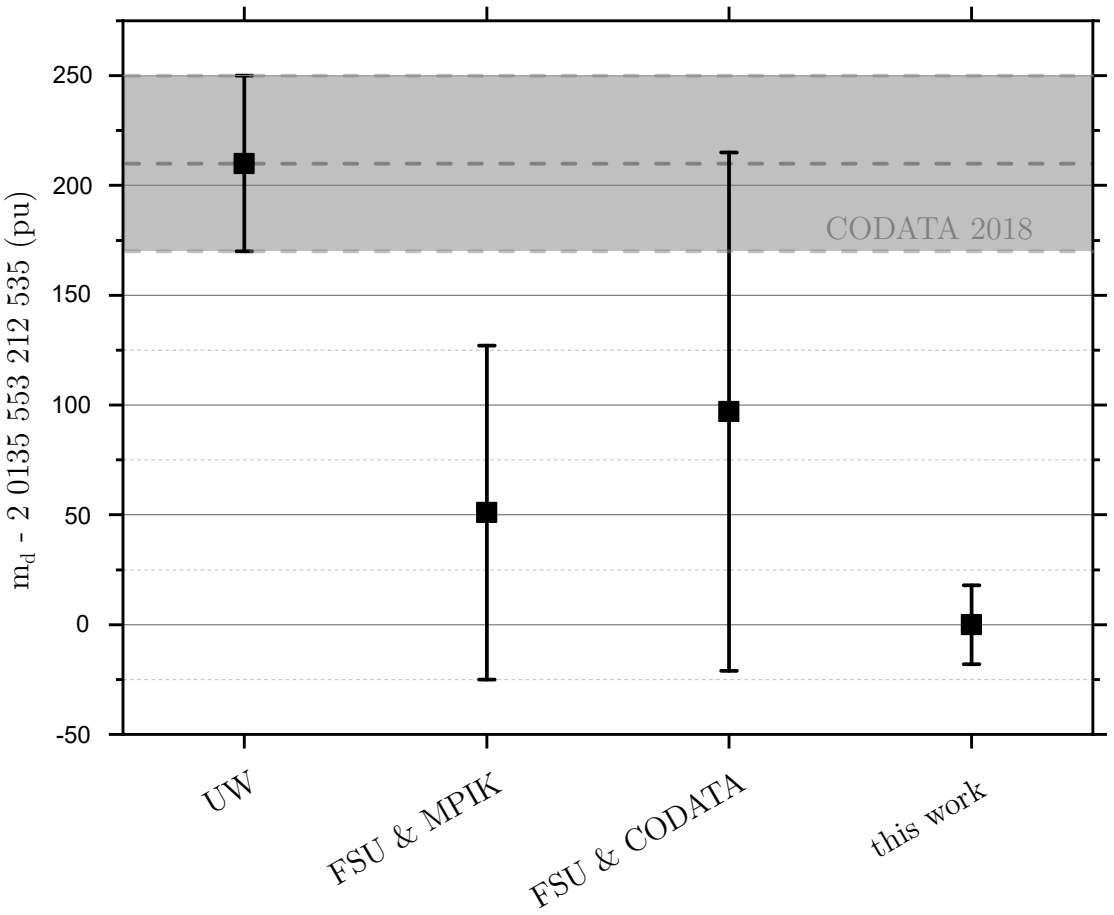

Figure 5.3: Comparison of the deuteron mass with literature. The value obtained in this work is compared to a mass value reported by the University of Washington (UW) [18] and to a combination of the deuteron-to-proton mass ratio reported by the Florida State University (FSU) [87] and a value for the proton mass, either the one reported by LIONTRAP [7] or the CODATA 2018 literature value [85]. The gray band with dashed borders denotes the literature value for m_d, which coincides with the value reported by the UW since the 2014 adjustment [88]. Our value is discrepant with the UW value, the discrepancy is $4.8\,\sigma$. The deuteron-to-proton mass ratio by the FSU is compatible with both values.

5.4 Measurement of the HD^+ Molecular Ion

During the deuteron measurement campaign, the discrepancy to the UW value [18] became apparent while measurements with the first ion pair were running. Owing to the existent inconsistencies in the light mass region (see section 1.2.2), a discrepancy to the UW value did not come as a surprise. Still, we were looking for possibilities to cross-check and validate our measurement. For the proton mass campaign, where also a $3.3\,\sigma$ discrepancy was revealed [8, 7], we measured the mass ratio of $^{12}C^{6+}$ compared to $^{12}C^{3+}$. This mass difference can be calculated with negligible uncertainty, since the electron mass and the binding energies are well known, making this comparison a good cross-check. However, this measurement was more relatable to the proton mass measurements, since there the charge-to-mass ratio of the ions also differed by a factor of ≈ 2.To closely resemble the deuteron measurement, we were looking into measurements with hydrogen molecular ions.

The H_2^+ molecular ion has a mass, which is very similar to the mass of deuteron. Also, it is easily available in our trap setup (see figure 4.1). Its mass is known from our previous proton mass measurement, making this system a suitable candidate for a validation measurement. However, owing to the symmetry of this molecular ion, its rovibrational states decay on very long time scales. Since the energy in these states leads to a mass shift on a relevant level, this makes measurements using the H_2^+ molecular ion tricky. In the FSU deuteron-to-proton mass measurement [87], this was tackled with great effort, utilizing Stark-quenching of the vibrational levels and modeling the rotational level distribution. However, this was still the leading uncertainty for the deuteron-to-proton mass ratio at 16 ppt.

To avoid such difficulties, we decided to attempt a measurement of HD^+, as its mass can also be derived from the masses of its constituents, see section 5.5. With a charge-to-mass ratio of $e/(3\mathrm{u})$, its frequencies are significantly different from deuteron. It is unlikely, that a potentially overlooked systematic effect happens to scale in a manner, that they cancel out in the combination of the measurements of the proton, the deuteron and HD^+ with different frequencies and systematics. It was unclear whether producing HD^+ would work. In the mass spectrum in figure 4.1, one can see that the amount of H_2^+ and the amount of deuterons was in the same order of magnitude, and the amount of protons was many orders of magnitude higher. Therefore, one expects there to be even less HD^+ then deuteron ions to be produced. However, by using the same production process as for the production of deuterons and looking at an expected trap voltage of $-11.4\,\mathrm{V}$, it was possible to produce and isolate a single HD^+ ion. For HD^+, the rovibrational states pose much less of a problem. The first excited rovibrational state has a lifetime of 149 s and a transition energy of 5.4 meV [89]. This corresponds to a temperature of 63 K. Since the mass measurements started about a week after the production of the HD^+ ion, it can be assumed to be in its rovibrational groundstate in our 4.2 K environment. Averaging over the thermal distribution is in this case not necessary, as the resulting effect on the frequency ratio is negligible. As a

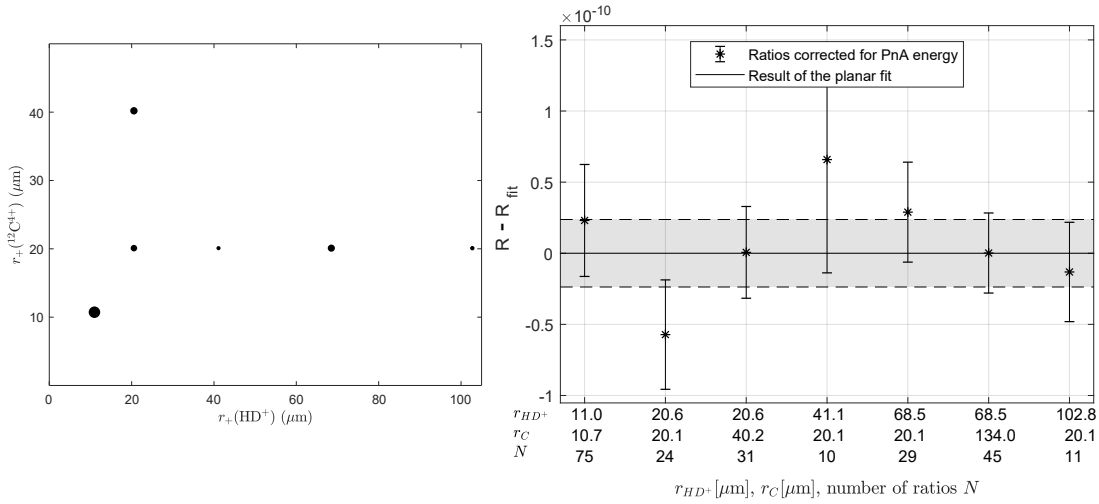

Figure 5.4: Surface fit for the HD^+ measurement. The scatter plot on the left indicates the excitation radii used. The area of the circles is proportional to the number of cycles N taken at this excitation. This number, together with the corresponding excitation radii, is also given on the x-axis of the plot on the right side. There, the residuals of the surface fit are shown. The gray band corresponds to the 1σ confidence level of R_0 extracted from the fit.

reference ion, $^{12}C^{4+}$ was used, since this also has a charge-to-mass ratio of $e/(3u)$. Its mass in atomic mass units is given by

$$m(^{12}C^{4+}) = 11.997\,805\,839\,274\,83\,(34)\,\text{u}. \tag{5.12}$$

The ionization energies used for the calculation of this value are given in table 5.1. With a relative precision of $2.8 \cdot 10^{-14}$, this mass is sufficiently well known to not limit a mass measurement of HD^+.

5.4.1 Statistical Evaluation

Prior to starting the data taking, the trap potential was optimized in the same way as for the deuteron ions. Preparatory measurements like a calibration of the cyclotron excitation κ_+, a measurement of the ions temperature and a check of the magnetic inhomogeneity B_2 were performed. For B_2 and the temperature, the values were in agreement with the ones measured for the deuteron. For HD^+, only one pair of ions trapped for about seven weeks was used. Again, the PnA excitation amplitudes were varied and the data was analyzed using the surface fit method, as shown in figure 5.4. The statistical frequency ratio R_{stat} resulting from the fit is

$$R_{\text{stat}} = 1.007\,310\,263\,850\,(19). \tag{5.13}$$

From the fitted slopes, values for the excitation calibrations for deuteron, and for

Table 5.4: Systematic shifts and their uncertainties after extrapolation to zero excitation amplitude for HD^+. All values are relative and in parts-per-trillion.

Effect	Shift of ν_c for HD^+	Shift of ν_c for $^{12}C^{4+}$	Correction to R^{CF}	Uncertainty
Image charge	−24.9	−98.7	73.8	3.7
Special relativity (thermal)	−1.5	−0.4	−1.1	0.5
Magnetic inhomogeneity	0.2	0.1	0.2	0.3
Electrostatic anharmonicity	0	0	< 0.1	0.4
Lineshape	0	0	0	6.75
Magnetron frequency	0	0	0	2.1
Polarization	−18.4	0	−18.5	< 0.1
Total	−44.6	−99.0	54.3	11.4

carbon,

$$\begin{aligned} \kappa_{+,d} &= 1.350\,(37) \cdot 10^{-2}\,\mathrm{m/Vpp/sec} \\ \kappa_{+,C} &= 1.362\,(17) \cdot 10^{-2}\,\mathrm{m/Vpp/sec}, \end{aligned} \tag{5.14}$$

can be derived. These values are to be compared with the direct measurement performed with a $^{12}C^{4+}$ ion, which yielded

$$\kappa_+ = 1.340(35) \cdot 10^{-2}\,\mathrm{m/Vpp/sec}. \tag{5.15}$$

All three values agree within their uncertainties.

5.4.2 Evaluation of Systematic Shifts

The systematic shifts and their uncertainties were evaluated in the same manner as for the deuteron. The only difference is the polarization shift introduced in section 2.7.3. The values for the systematic shifts are listed in table 5.4. The uncertainty originating in the image charge shift is slightly reduced, owing to the mass of HD^+ being $\approx 1\,\mathrm{u}$ higher than for deuteron. This increased mass is also the reason the term special relativity (thermal) becomes even smaller. On the other hand, the reduced cyclotron frequency of about 20 MHz is now closer to the axial frequency, which is why uncertainties during the dip measurement have an increased impact on the uncertainty of the cyclotron frequency ratio. This resulted in the dip lineshape being the dominant systematic uncertainty for the HD^+ measurement. The final ratio correct for systematic shifts is

$$R\left(^{12}C^{4+}/HD^+\right) = 1.007\,310\,263\,905\,(19)_{\mathrm{stat}}(8)_{\mathrm{sys}}(20)_{\mathrm{tot}}, \tag{5.16}$$

where the brackets again denote the statistical, systematic and combined uncertainty, respectively. The measurement is strongly limited by statistics.

5.5 Mass Value and Comparison with Expectation

From this measured frequency ratio and the mass of $^{12}C^{4+}$ given in equation (5.12), the directly measured value for the mass of the HD^+ molecular ion becomes

$$m\left(HD^+\right)_{\text{direct}} = 3.021\,378\,241\,561\,(56)_{\text{stat}}(24)_{\text{sys}}(61)_{\text{tot}}\,\text{u}. \tag{5.17}$$

The mass of HD^+ can also be derived by using the mass of its constituents. The atomic binding energy of the three body system electron, deuteron, and proton, which is about 16.3 eV, can be calculated theoretically to a precision where it does not contribute to the uncertainty anymore [90]. Converted into atomic mass units, the binding energy becomes $B(HD^+) = 17.4663 \cdot 10^{-9}\,\text{u}$ with negligible uncertainty. Together with the proton mass previously reported by LIONTRAP ($m_p = 1.007\,276\,466\,598\,(33)\,\text{u}$), the deuteron mass given in equation (5.10), and the electron mass [85, 62] ($m_e = 5.485\,799\,090\,65\,(16) \cdot 10^{-4}\,\text{u}$), the expected mass of HD^+ becomes

$$m\left(HD^+\right)_{\text{p+d}} = 3.021\,378\,241\,576\,(37)\,\text{u}. \tag{5.18}$$

Both values agree on a $1\,\sigma$ level, $m(HD^+)_{\text{p+d}} - m(HD^+)_{\text{direct}} = 15\,(71)\,\text{pu}$. The comparison is limited by the statistical precision of the direct measurement of HD^+. This is because the data taking with HD^+ was stopped when the uncertainty for R_{stat} taken from the preliminary analysis was on a comparable level to the uncertainty arising from the proton mass. However, the uncertainty in the final analysis turned out slightly larger. The agreement between both values opens up the possibility for a least square adjustment as described in the next section.

5.6 Least Square Adjustment

When taking the mass of the electron and the involved binding energies as fixed, one has a situation with more experimental links than underlying physical quantities. In such a situation, one can perform a least square adjustment to get the best possible estimates for the values of the underlying physical quantities. How this can be realized for mass measurements is described for example in [91]. Following a least square approach on a consistent data set results in adjusted values with reduced uncertainties. However, one needs to be careful, since the resulting values are correlated.

In this section, two least square adjustments are evaluated. An adjustment with only the results of LIONTRAP gives a best guess for a deuteron-to-proton mass ratio. This can then be compared with the one measured directly by the FSU [87]. Since both values agree, the FSU value can be included in a subsequent adjustment.

5.6.1 LIONTRAP internal adjustment

The quantities for which we are interested in adjusted values are the proton mass m_p and the deuteron mass m_d. The available input values are the direct measurements of both of these masses as well as the measurement of the HD^+ molecular ion. All three values are assumed to be uncorrelated. The proton mass was limited by the residual magnetic inhomogeneity, which does not play a relevant role for the deuteron and the HD^+. The HD^+ measurement was limited by statistics, for the deuteron mass both the statistical as well as the systematic uncertainty play a relevant role. While parts of the systematic uncertainties, most obviously the image charge shift, are correlated, the different limitations justify neglecting the correlations.
Performing this least square adjustment results in adjusted values

$$\begin{aligned} m_{p,\mathrm{lsq1}} &= 1.007\,276\,466\,595\,(29), \\ m_{d,\mathrm{lsq1}} &= 2.013\,553\,212\,534\,(17), \end{aligned} \tag{5.19}$$

with correlation coefficient $r(m_p, m_d) = -0.13$. Since the uncertainty of the HD^+ measurement was significantly larger than for the direct measurements, this results only in a slight decrease of the uncertainties. From these adjusted values, the deuteron-to-proton mass ratio

$$\frac{m_d}{m_p}(\textsc{Liontrap}) = 1.999\,007\,501\,228\,(58) \tag{5.20}$$

can be deduced. Here, the uncertainty including the correlation coefficient is calculated using the standard formula,

$$\delta\left(\frac{m_d}{m_p}\right) = \sqrt{\left(\frac{\delta(m_p)}{m_d}\right)^2 + \left(\frac{m_p\delta(m_d)}{m_d^2}\right)^2 + 2\mathrm{cov}(m_p, m_d)\frac{m_d}{m_p^3}}, \tag{5.21}$$

where $\mathrm{cov}(m_p, m_d) = r(m_p, m_d)\delta(m_p)\delta(m_d)$. Since $r(m_p, m_d) < 0$, taking into account the correlation actually reduces the uncertainty of the deuteron-to-proton mass ratio slightly.

5.6.2 Consistency Across Groups

This deuteron-to-proton mass ratio can be compared with the one derived from a measurement comparing H_2^+ and deuteron reported by the FSU [87]. Their value

$$\frac{m_d}{m_p}(\mathrm{FSU}) = 1.999\,007\,501\,274\,(38) \tag{5.22}$$

agrees with the value from the LIONTRAP adjusted values on a $1\,\sigma$ level. This consistency between different Penning-trap groups on such a level of precision does not only constitute a great cross-check for the involved measurement methods, it

also allows including this proton-to-deuteron mass ratio as another link in the least square adjustment, resulting in

$$\begin{aligned} m_{p,\mathrm{lsq2}} &= 1.007\,276\,466\,580\,(17) \\ m_{d,\mathrm{lsq2}} &= 2.013\,553\,212\,537\,(16). \end{aligned} \tag{5.23}$$

There, the reduced chi-squared of $\chi^2_{\mathrm{red}} = 0.43$ stresses the consistency between these four measurements. The main benefit of this adjustment is a reduced uncertainty of the value for the proton mass of only 17 ppt. Compared to the LIONTRAP measurement, the uncertainty is reduced by a factor of two, compared to the current CODATA literature value [85] even by a factor of three. The correlation coefficient is $r(m_p, m_d) = 0.26$.

5.6.3 Implications on the Neutron Mass

The atomic mass of the neutron cannot be measured using conventional mass spectrometry in Penning traps, as it has no charge. Therefore, its mass is determined by a combination of Penning-trap mass measurements on isotopes, which differ by one neutron, and a measurement of the neutron seperation energy S_n. This seperation energy can be measured at neutron beam facilities [33, 34] by using Bragg spectroscopy. There, an absolute wavelength measurement of the gamma-ray of the neutron capture is performed.
Traditionally, one uses the proton and the deuteron for this measurement. Owing to their low mass, the Penning-trap mass measurements do not pose a strong limitation on the determination of the neutron mass when using proton and deuteron. The reaction rate of the neutron capture process is decent and the energy of the gamma ray is with 2.2 MeV not too high. This principle was used in a 1999 measurement using the the GAMS4 flat crystal spectrometer [34], resulting in a value for S_n with a relative precision of about $1 \cdot 10^{-7}$ [33]. Up to this date, this measurement is still the only one at this level of precision.
In this bragg measurement, the actually observed quantity is the scattering angle of the gamma photon. To translate this angle into a wavelength, the lattice constant of the used crystal is needed. This crystal is referred to in the literature as ILL2.5. Its lattice constant had to be updated in 2006 [35] and recently in 2017 [92]. The 2017 and 2006 values for the lattice constant are

$$\begin{aligned} d_{\mathrm{new}} &= 192.015\,5721\,(64) \cdot 10^{-12}\,\mathrm{m}, \\ d_{\mathrm{old}} &= 192.015\,5822\,(96) \cdot 10^{-12}\,\mathrm{m}. \end{aligned} \tag{5.24}$$

While there are different approaches on how to translate the angle measurement into a wavelength measurement, all approaches yield the same dependency for small angle changes,

$$\lambda^{meas}_{\mathrm{new}} = \frac{d_{\mathrm{new}}}{d_{\mathrm{old}}} \lambda^{\mathrm{meas}}_{\mathrm{old}} \tag{5.25}$$

$$= 0.557\,671\,299\,(97) \cdot 10^{-12}\,\mathrm{m}. \tag{5.26}$$

Here, $\lambda_{\mathrm{old}}^{\mathrm{meas}} = 0.557\,671\,328\,(99) \cdot 10^{-12}\,\mathrm{m}$ [35] was used. This corresponds to an energy of

$$E^{\mathrm{meas}} = 2\,223\,248.69\,(39)\,\mathrm{eV}. \tag{5.27}$$

Both these values refer to the measured quantities, but to extract the binding energy, one has to correct for nuclear recoil [33]. This yields

$$\begin{aligned} S_n &= E^{\mathrm{meas}} + \frac{(E^{\mathrm{meas}})^2}{2m_d\mathrm{c}^2} \\ &= 2\,224\,566.35\,(39)\,\mathrm{eV} \\ &= 2.388\,170\,08\,(42) \cdot 10^{-3}\,\mathrm{u}. \end{aligned} \tag{5.28}$$

Here, $m_d\mathrm{c}^2$ is the atomic mass of deuteron expressed in eV using the conversion factor $(1\mathrm{u})c^2 = 9.314\,941\,024\,2\,(2\,8) \cdot 10^8\,\mathrm{eV}$ [85]. The discrepancies in m_d reported in this work as well as the conversion to eV do not play any role at the level of precision needed for the recoil correction.
Using value for the neutron binding energy given above and the masses for the proton and the deuteron after the least-square adjustment given in this work, the neutron mass becomes

$$m_n = 1.008\,664\,916\,04\,(42)\,\mathrm{u}, \tag{5.29}$$

with a relative precision of $4.2 \cdot 10^{-11}$. The precision is strongly limited by the precision of the gamma-ray measurement. The neutron mass m_n also has a correlation coefficient with both the proton mass m_p and the deuteron mass m_d, $r(m_p, m_n) = -0.03$ and $r(m_d, m_n) = 0.03$.
The value for the neutron mass given above is heavier by $9 \cdot 10^{-11}\,\mathrm{u}$ compared to the CODATA 2018 literature value [85]. It is noteworthy that the new value for the deuteron mass leads to an increase of the neutron mass calculated with this method by $2.1 \cdot 10^{-10}$. The difference between the LIONTRAP proton mass and the CODATA 2018 value gives rise to a shift in the neutron mass of $-0.4 \cdot 10^{-11}$ and the difference between the 2006 and 2017 binding energies to a shift of $-1.3 \cdot 10^{-10}$, which does not add up to the $9 \cdot 10^{-11}\,\mathrm{u}$ difference given above. The reason for this is that CODATA treats the lattice constant of the crystal used in this measurement as an adjusted value in their least-square adjustment [88]. However, as this value is not a fundamental constant, it is a so-called hidden parameter, and the 2018 value is not available yet.

5.6.4 Comparison with Molecular Spectroscopy

Recently, the spectroscopy of hydrogen molecular ions made a lot of progress [29, 30, 31, 32]. Precision measurements of the rovibrational transitions in HD^+ can be used to test three body calculations in quantum electrodynamics (QED). At a certain level of precision, one can also assume QED to be correct and extract

fundamental constants. The transitions in HD^+ are sensitive to a combination of the Rydberg constant R_∞ and the involved masses.
In the group of Stephan Schiller in Düsseldorf, the frequency of the fundamental rotational transition $(\nu, N) : (0, 0) \rightarrow (0, 1)$ at 1.3 THz is measured [31]. Here, ν and N denote the quantum numbers of the vibrational and rotational levels, respectively. From this, they extract a value

$$R_\infty \left(\frac{m_e}{m_p} + \frac{m_e}{m_d} \right)_{\text{Schiller}} = 8\,966.205\,150\,50\,(17)\,\text{m}^{-1}. \tag{5.30}$$

When inserting the values from the least square adjustment in section 5.6.2 and the CODATA 2018 value for the Rydberg constant $R_{\text{inf}} = 10\,973\,731.568\,160\,(21)\,\text{m}^{-1}$ [85], this yields

$$R_\infty \left(\frac{m_e}{m_p} + \frac{m_e}{m_d} \right)_{\text{mass lsq \& CODATA}} = 8\,966.205\,150\,96\,(28)\,\text{m}^{-1}. \tag{5.31}$$

Both values differ by $46\,(33) \cdot 10^{-8}\,\text{m}^{-1}$, which corresponds to $1.4\,\sigma$.
In the group of Jeroen Koelemeij in Amsterdam, the transition $(\nu, N) : (0, 3) \rightarrow (9, 3)$ is measured using two photons at 1.4 µm each [32]. The transition frequency depends on the masses, the Rydberg constant, the rms charge radii of the proton and the deuteron. The measured transition frequency is

$$\nu_{\text{exp}} = 415\,264\,925\,500.5\,(1.2)\,\text{kHz}. \tag{5.32}$$

This agrees well with the theory prediction, where the CODATA 2018 constants were used, $\nu_{\text{CODATA2018}} = 415\,264\,925\,496.2\,(7.4)\,\text{kHz}$. When instead using the adjusted masses of section 5.6.2, the theory frequency becomes

$$\nu_{\text{mass lsq \& CODATA}} = 415\,264\,925\,505.1\,(5.2)\,\text{kHz}. \tag{5.33}$$

This value still agrees with the experimentally measured one, however, it has a slightly improved uncertainty. The mass ratios from Penning traps are now limited by the electron mass, which is known with a relative precision of $2.9 \cdot 10^{-11}$. One can now either extract fundamental constants from the spectroscopy results, or use independent values for these constants and set limits on physics beyond the standard model by the fact, that both values agree [31].

5.6.5 The Puzzle of Light Ion Masses

The puzzle of light ion masses was introduced in section 1.2.2 Using the mass values from the least square adjustment above, the term $\Delta = m_p + m_d - m_{\text{he}}$ becomes

$$\Delta_{\text{C}} = 0.005\,897\,432\,449\,(50). \tag{5.34}$$

Here, the mass of the ^{3}He nucleus m_{he} is still the value reported by the University of Washington (UW) [18]. The masses of the proton and the deuteron are from the

adjustment including the direct mass measurements of the proton, the deuteron, HD^+ by LIONTRAP and the deuteron-to-proton mass ratio by the FSU [87], where a consistency between different measurement groups was shown. Comparing this value to the one derived by a mass ratio measurement of HD^+ and ^{3}He reported by the FSU [19] (Δ_{FSU}) yields a discrepancy of

$$\Delta_{\mathrm{FSU}} - \Delta_{\mathrm{C}} = 258(86)\,\mathrm{pu}. \tag{5.35}$$

Since a consistency between LIONTRAP and the FSU was already shown, and discrepancies to the values reported by the UW were observed both for the proton mass and the deuteron mass, this leaves ^{3}He as the most likely candidate to explain the remaining $3\,\sigma$ discrepancy. A mass measurement of ^{3}He will be among the next projects at LIONTRAP.

5.7 Limitations of the Deuteron Mass Campaign

In this section, I analyze the statistical limitations of the deuteron mass campaign. In total, 1100 cycles were used to reach the final statistical precision of $5.4 \cdot 10^{-12}$. Without increasing the shot-to-shot precision, achieving statistical precisions in the low 10^{-12} range seems infeasible. Therefore, the cause of the jitter of our frequency ratio needs to be investigated.

5.7.1 Modeling PnA Resolution

The resolution achievable with the PnA measurement is one of the major factors in determining the possible statistical precision achievable in a mass measurement campaign. The frequency resolution $\delta\nu$ is connected to the phase resolution $\delta\phi$ by

$$\frac{\delta\nu}{\nu} = \frac{\delta\phi}{\nu\, T_{\mathrm{evol}}\, 180^\circ}, \tag{5.36}$$

where $\delta\phi$ is given in degrees. The physical effects limiting this resolution can be divided into frequency and phase jitter. The following effects contribute a phase jitter:

1. Imprinting the phase. The phase is imprinted by a dipolar excitation. It is well defined, if the thermal radius is negligible compared to the excitation radius, $r_{\mathrm{exc}} \gg r_{\mathrm{thermal}}$. However, to avoid systematic shifts, a small excitation radius is desirable, so some phase jitter from imprinting the phase is accepted.

2. Phase jitter from the transfer to the axial motion. As described in section 2.6, the ions amplitude in the cyclotron mode must be significantly larger than the axial amplitude multiplied with $\sqrt{\frac{\omega_z}{\omega_+}}$ (equation (2.70) therein). If this condition is met to a lesser degree the axial phase will influence the measured phase more. As the axial phase has no phase relation to the cyclotron phase we want to measure, this leads to an additional jitter. Because both modes

are thermalized to the same axial resonator, this jitter and the one detailed above are related.

3. Read-out jitter. In reading-out the phase in the axial mode, the limited signal-to-noise ratio leads to a phase jitter. For the PnA-technique, the amplitude of the second PnA pulse can be optimized in order to minimize this effect.When increasing the amplitude of the second pulse, the read-out jitter is reduced until the amplitudes become big enough for field inhomogeneities to introduce an additional read-out jitter. The read-out jitter can be numerically simulated, the validity of this simulation was checked in [54, 93]. The phase-jitter occurring when the second PnA pulse is too strong is not easily modeled as it originates in high order field inhomogeneities which are hard to access. However, usually one uses excitation amplitudes, where this phase-jitter does not play a significant role yet.

4. Residual dipolar excitation of the second PnA pulse. The second PnA pulse, which is supposed to be a quadrupolar excitation at $\nu_+ + \nu_z$ can inhibit a residual off-resonant dipole component. If the phase relation between the first and the second PnA pulse are constant, this can lead to a systematic shift of the measured phase. This effect was measured to be $< 1°$ [54]. In order to not have a systematic effect, the phase of the first PnA pulse was chosen randomly in every cycle, translating the potential phase shift in a phase jitter. However, this phase jitter can be neglected compared to the other sources of jitter presented here.

5. Jitter from the used Devices. In principle, the timing system and the read-out devices also contribute to the phase jitter. However, in our system these contributions are $< 0.1°$ and thus negligible.

On the other hand, the following frequency jitter can occur:

1. Special relativity. The motional amplitude during the PnA gives rise to a relativistic shift. In the same manner as described in section 2.4, the motional amplitude and thus the shift varies depending on the random phase relation between the excitation pulse and the initial phase of the ion. The frequency jitter from this effect depends on the proportions between the thermal radius and the excitation radius. For ions excited to the same radius, the jitter decreases for increasing mass.

2. Field imperfections. In the same manner as in the previous point, field imperfections also lead to a frequency shift dependent on the excitation amplitude. For the magnetic homogeneity and the electric harmonicity at LIONTRAP, the jitter originating from this effect is negligible compared to the relativistic jitter.

3. Magnetic field drifts. Magnetic field drifts limit the resolution available to mass measurements. However, for the purpose of evaluating the frequency

Table 5.5: Examples of the measured phase jitter during the deuteron mass campaign and comparison with a Monte-Carlo simulation. All phase jitters are given in degrees. For details see text.

			Measurement		Model			
Ion	r_{exc}	T_{evol}	$\delta\phi$	SNR	$\delta\phi_{\mathrm{tech.}}$	$\delta\phi_{\mathrm{therm.}}$	$\delta\phi_{\mathrm{rel.}}$	$\delta\phi_{\mathrm{tot.}}$
C^{6+}	10 µm	10 ms	11.6	20.1	5.8	10.2	< 0.1	11.7
		30 s	19.4				1.5	11.8
	100 µm	10 ms	4.3	23.2	3.9	1.0	< 0.1	4.0
		25.2 s	19.6				12.2	12.8
d	10 µm	10 ms	27.1	17.3	8.1	28.5	< 0.1	29.6
		30 s	28.2				3.7	29.9
	100 µm	10 ms	10.6	15.4	10.0	2.5	< 0.1	10.3
		25.2 s	35.3				29.3	31.1

resolution, constant linear magnetic field drifts can be eliminated to a large extend by examining the standard deviation of the difference between subsequent PnA measurements. For normally distributed data exhibiting a slow drift, this standard deviation of the differences is about $\sqrt{2}$ times the standard deviation of the original sample without drift.

4. Jitter of the atomic clock. When the frequency standard given by the atomic clock jitters, this does not affect the particle. However, the read-out phase will jitter, because the evolution time T_{evol} will differ depending on the actual frequency of the atomic clock. Our model was specified to have an Allan variance of better than $1 \cdot 10^{-11}$ on a time scale of 10 s, which is comparable to the evolution time. On longer time scales, this becomes even better. In test measurements, where the clock used at LIONTRAP was compared to a different clock of the same manufacturer, no excess instabilities were seen, indicating that the effect of the atomic clock can be neglected for now.

In principle one can increase the evolution time, until the phase-unwrap can no longer be performed unambiguously. To this end, the maximally accepted phase jitter is typically about 40°. When increasing the evolution time, the impact of phase jitter on the frequency resolution is reduced, while the impact of frequency jitter is not affected.
In table 5.5, the phase jitter measured during the deuteron mass campaign for different settings are compared to a Monte-Carlo simulation taking into account the effects detailed above.
There, $\delta\phi_{\mathrm{tech.}}$ corresponds to the read-out phase jitter originating in the limited SNR. $\delta\phi_{\mathrm{therm.}}$ denotes the phase jitter from imprinting the phase onto the thermal ion and $\delta\phi_{\mathrm{rel.}}$ denotes the mostly relativistic frequency jitter expressed as a phase jitter. The quadratic sum of all three gives the total phase jitter expected in this

model $\delta\phi_{\text{tot.}}$, which is to be compared with the measured phase jitter $\delta\phi$. The statistical uncertainty of the stated measured phase jitter is about 2°. For the modeled phase jitter, various sources of uncertainty play a role. For the technical read-out jitter, it is hard to give a valid estimate of uncertainty, as this is a very simplified model. However, the agreement between model and measurement for both ions at $r_{\text{exc}} = 100\,\mu\text{m}$ and $T_{\text{evol}} = 10\,\text{ms}$, where the read-out jitter is dominant, suggests that uncertainties are below a few degrees. The jitter from imprinting the phase $\delta\phi_{\text{therm.}}$ and from relativistic shifts $\delta\phi_{\text{rel.}}$ depend heavily on the temperature of the ion. In section 2.4, the uncertainty for the temperature measurement was given as $T = 1.2\,(5)\,\text{K}$. This translates for example in an uncertainty for the combination of $\delta\phi_{\text{therm.}}$ and $\delta\phi_{\text{rel.}}$ of $\approx 7°$ for deuteron at both 10 µm and 100 µm. For carbon, the respective uncertainty is lower and about 2.2° at 10 µm and $\approx 0.2°$ at 100 µm.

In the examples shown in table 5.5, the modeled phase jitter $\delta\phi_{\text{tot}}$ agrees with the measured phase jitter $\delta\phi$ for short evolution times $T_{\text{evol}} = 10\,\text{ms}$ within the uncertainties given above. Although the uncertainties of the model for the phase jitter are hard to estimate, the agreement with the measured phase jitters shown here suggests that the model accurately describes the involved jitter. Furthermore, the value for the temperature is indeed accurate and the uncertainty might even be slightly overestimated.

For the long evolution times, the magnetic field jitter adds to the modeled phase jitter. To estimate this, we compare the measured phase jitter of the long evolution times, with the measured phase jitter for $T_{\text{evol}} = 10\,\text{ms}$. For carbon at 100 µm this difference is the largest. The 30 s phases show an additional jitter of $\sqrt{19.6^2 - 4.3^2} = 19.1°$. The modeled phase jitter suggests a contribution of 12.2° from the relativistic frequency jitter. Subtracting this in squares results in a remaining phase jitter of 14.7°. If one attributes this to magnetic field jitter, this corresponds to a stability of the magnetic field of $\delta B/B = 4.7 \cdot 10^{-11}$. For carbon at 10 µm, the same calculation yields a remaining phase jitter of 15.5°, indicating that the magnetic field was similarly stable throughout the measurement campaign.

For the deuteron, the magnetic field jitter barely contributes to the observed phase jitter. When averaging over PnA cycles, one thus averages mostly over the thermal distribution of the ion. Therefore, a decreased temperature would not only result in reduced systematic uncertainties, but also in a reduced phase jitter and with that an improved statistical precision.

From the phase jitters given in table 5.5, one can estimate the expected resolution of the PnA measurement. For $^{12}\text{C}^{6+}$ at 10 µm, the uncertainty of the 10 ms phase is $11.6°/\sqrt{6} = 4.7°$, as this phase was measured six times during each cycle. The phase with long evolution time was also measured six times, however, there the most outer cycle was disregarded to avoid the influence of potential voltage drifts after transport. This phase uncertainty is thus $19.4°/\sqrt{5} = 8.7°$. This results in a resolution for the modified cyclotron frequency of $\delta\nu_+/\nu_+ \approx 4.3 \cdot 10^{-11}$. For the deuteron at 10 µm, the same consideration yields to a resolution of $\delta\nu_+/\nu_+ \approx$

$7.6 \cdot 10^{-11}$. For the ratio, both resolutions can be added in squares as they can be assumed to be independent, yielding a resolution for the frequency ratio of

$$\left(\frac{\delta R}{R}\right)_{\text{PnA, 10 µm}} = 8.9 \cdot 10^{-11}. \tag{5.37}$$

Throughout the measurement campaign the measured stability of the frequency ratio for the data taken with radii of 10 µm was about $2.0 \cdot 10^{-10}$. For the whole data set, this value was a bit better with $1.6 \cdot 10^{-10}$. Therefore, other factors need to play a role in the statistical limitation of the frequency ratio.

5.7.2 Magnetic Field Drifts

In the last section we found, that magnetic field jitter does not play a major role for the statistical limitation in the deuteron measurement campaign, and one averages mostly over the thermal energy distribution of the ion. However, in the analysis of the magnetic field jitter, slow magnetic field drifts drop out because the standard deviation of the phase differences were considered per cycle. For the cyclotron frequency ratio, these drifts nevertheless play a role, and as shown in figure 5.5, slow drifts did occur during the measurement campaign, even though a decay of the magnetic field as observed in freshly charged magnets does not occur in our magnet anymore, as it was charged 25 years ago in 1995. However, between runs and between ion pairs, jumps in the cyclotron frequency can be observed, owing to different used settings and the filling of cryo-reservoirs which occurs between runs. During runs drifts of the cyclotron frequency of typically 8 mHz per cycle occur. The origin of these drifts is not yet understood. The most likely explanation are long term effects of the thermalization after filling, but other effects like the level of the cryo-reservoirs might also play a role.
The measurement cycle is, depending on the exact settings used, between 63 min minutes and 76 min long. The measurement of the phases with long evolution time, which are sensitive to magnetic field variations take in total ≈ 10 min per ion, the transport and pre-cooling took ≈ 330 s. In the analysis, the most inner PnA cycle was disregarded to exclude potential drifts of the voltage after transport[1]. Therefore, the center times of the used PnA cycles were ≈ 17 min apart, approximately 1/4 of the total time of a measurement cycle. When combining this with the 8 mHz typical drift between cycles above, one expects the magnetic field to drift an amount of typically $\delta B/B \approx 7 \cdot 10^{-11}$ between the measurements of deuteron and carbon. As the order of the ions is random, and the drift at least to some extend, too, this effect does not give rise to a systematic shift, but rather a jitter of the frequency ratio R of

$$\left(\frac{\delta R}{R}\right)_{\text{magnet drift}} \approx 7 \cdot 10^{-11}. \tag{5.38}$$

[1]For simplicity, the most inner PnA cycle of both ions was disregarded, although for the first ion in each measurement cycle no transport occurred immediately before the PnA measurements.

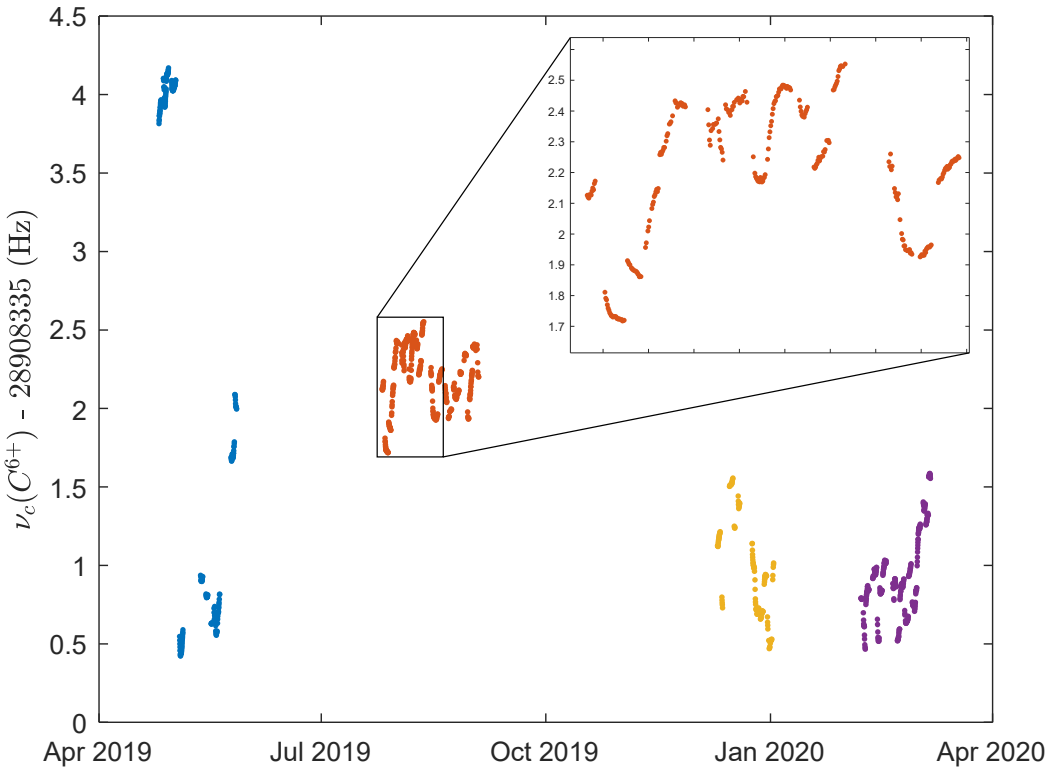

Figure 5.5: Magnetic field drifts. Plotted are the cyclotron frequencies of $^{12}C^{6+}$ throughout the measurement campaign, the four ion pairs are color coded. Especially in the beginning of the measurement campaign, significant variations of the cyclotron frequency of up to $\approx 3.5\,\mathrm{Hz}$ are observed, corresponding to magnetic field shifts of $\delta B/B \approx 1 \cdot 10^{-7}$. There, the temperature stabilization parameters were varied, possibly explaining these large jumps. With ion pairs three and four, the magnetic field scatter is about 1 Hz, corresponding to $\delta B/B \approx 3 \cdot 10^{-8}$. A linear drift as seen with freshly charged magnets is no longer visible. The inset shows a zoom-in to a part of the data taken with ion pair two. The magnetic field shows jumps in the gaps between runs, where filling occurred, and otherwise relatively smooth drifts.

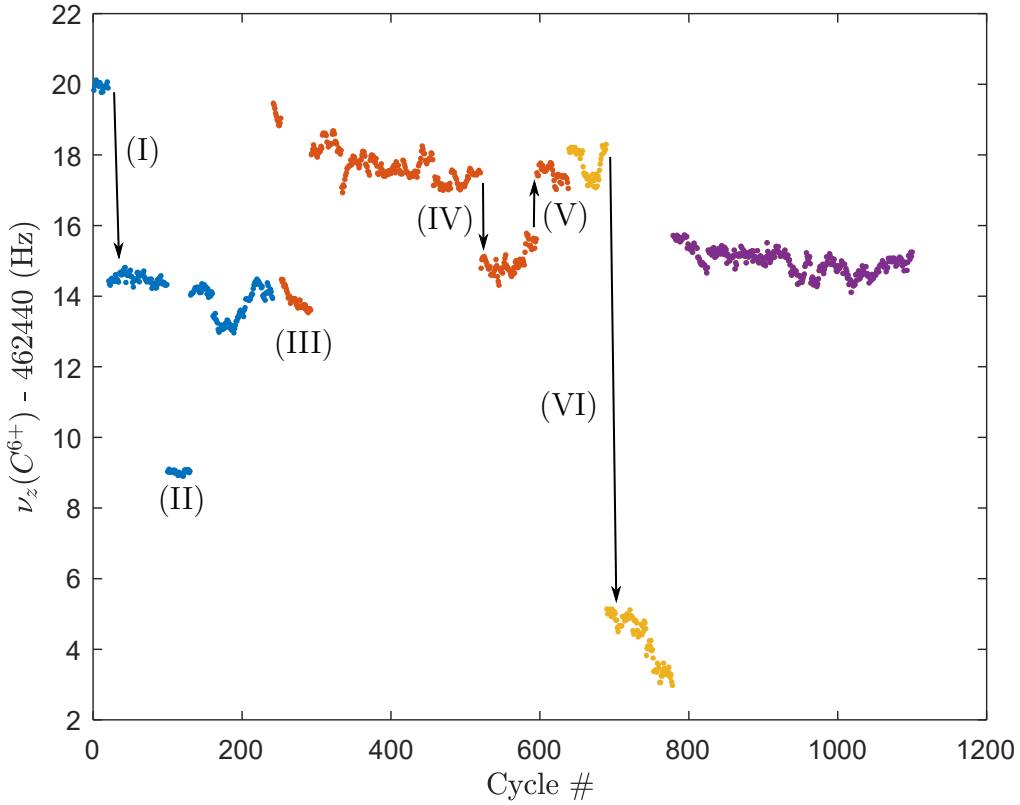

Figure 5.6: Axial frequency of $^{12}C^{6+}$ during the whole measurement campaign. The axial frequency ν_z is shown as a function of the cycle number. The frequency stayed relatively constant during the measurement campaign. Large jumps within each ion pair are marked with roman numbers. In (I), a number of devices unused in the mass measurement were disconnected. The fans used to circulate the air inside our temperature stabilized volume were off in the data marked with (II) and (III), leading to increased temperature gradients across the magnet. In (IV) and (V), the set-temperature of the temperature stabilization was changed from 33°C to 30°C and from 30°C to 32°C, respectively. At the position marked with (VI), the voltage was changed by 0.13 mV$\approx$4 Hz.

However, this jitter does not necessary have to be Gaussian distributed. In the extreme case of a perfectly constant drift and in absence of any other jitter, one would just observe two distinct frequency ratios, which jitter around the true frequency ratio by $\pm 7 \cdot 10^{-11}$, depending on which ion was chosen to be measured first.

5.7.3 Axial Frequency Determination

The determination of the axial frequency can also play a role in the statistical precision of the cyclotron frequency ratio. However, due to the use of the invariance-theorem, the impact of the axial frequency is reduced, $\delta\nu_c/\nu_c = \delta\nu_z\nu_z/\nu_c^2$. The axial frequency of $^{12}C^{6+}$ throughout the measurement campaign is shown in fig-

ure 5.6. Large jumps are marked with their causes given in the caption. When disregarding jumps between runs, the axial frequency scatters about 75 mHz for carbon and 72 mHz. The fact, that these numbers are so close while the width of the dip differs by a factor 6 suggests that voltage fluctuations cause this frequency scatter. If uncorrelated, such a scatter leads to a jitter of the frequency ratio of

$$\left(\frac{\delta R}{R}\right)_{\text{voltage drift}} = 5.1 \cdot 10^{-11}. \tag{5.39}$$

One should note that if this was just the voltage being different after each transport, it would not affect the free space cyclotron frequency at all, as the modified cyclotron frequency would shift accordingly and the magnetron frequency's impact can be neglected in the invariance theorem. However, if the axial frequency jitter is an expression of a voltage jitter far from the trap center, this could result in a shifted equilibrium position, and in combination with a linear magnetic field gradient in a cyclotron frequency jitter. In the magnetic field gradient measured in the PT ($B_1 = 0.00234(12)\,\mathrm{mT\,mm^{-1}}$), a displacement of 16 nm would be needed. This may not sound like a lot, but it is hard to draw a scenario where on the one hand, the axial frequency is as stable as observed, and on the other hand, the position jitters on a level which would result in a sizable cyclotron frequency jitter. For example, a voltage of 1 mV on the last endcap of the PT would result in a shift of the equilibrium position of only 1.6 nm, but shift the axial frequency by 0.2 Hz.

5.7.4 Conclusion of the Limitations of the Deuteron Mass Campaign

In this section, three main contributions to the statistical uncertainty were identified and analyzed. The resolution of the PnA, drifts of the magnetic field and the axial stability. However, when adding these in squares, one would expect a jitter for the ratio of $1.2 \cdot 10^{-10}$, to be compared with the measured jitter of $2.0 \cdot 10^{-10}$ (both values for 10 µm). To explain the measured statistical jitter using these three contributions, one would need to assume that they are correlated, which seems unreasonable. However, it is possible, that the voltage jitter causes an additional magnetic field jitter. Any change in the trap potential can potentially lead to a slightly shifted equilibrium position of the ion. In combination with a residual magnetic field gradient, this would lead to a magnetic field jitter. While this jitter in principle would appear in the analysis in section 5.7.2, there we assumed the magnetic field jitter to be suppressed by a factor of four due to the timings in the measurement cycle. When a significant portion of the magnetic field jitter is cause by the transport, this suppression is no longer justified, and could lead to above effect. To check for this effect, a distinct voltage source just for ion transport, which is completely disconnected during measurements, is in planning at LIONTRAP.
In summary it can be stated, that many effects play a role for the stability of the measured frequency ratio on a relevant scale. To improve, the first step is to eliminate the transport as a potential source of jitter. Then, one can improve

the resolution of the PnA by achieving lower temperatures. This would also allow to use less PnA measurements at long evolution times, potentially also reducing the impact of magnetic field drifts. A potential further step is to improve the measurement of the axial frequency. This could be done either by measuring peaks, which is a lot faster, but prone to systematic errors, or by taking the dip spectra during the evolution time of the PnA. Alternatively, the two-ion balance as implemented by the MIT [81, 84, 37] can potentially remove influences of magnetic field instabilities to a large extend and make ion transport unnecessary. However, when having two ions in the trap the motion of the ions becomes much more complex, resulting in systematic shifts, which one would need to carefully evaluate to see, if this technique would be feasible at LIONTRAP.

6 Outlook and Summary

In this chapter, I give an outlook on future projects at LIONTRAP and briefly summarize the findings in this work. The outlook begins with a discussion of measurements with simultaneous PnA in two traps and is followed by a description of a proposed new cooling method using electronic feedback cooling of the axial motion of a cloud of ions. The summary forms the final section of this chapter.

6.1 Simultaneous PnA in Two Traps

As outlined in section 3.4.2, one of the ideas to improve the statistical precision in mass measurements was the use of a magnetometer trap (MT). Under the assumption that changes of the magnetic field are homogeneous over both traps, the monitored magnetic field can be used to correct for such magnetic field changes and potentially improve the statistical precision of mass measurements, see also [7]. To investigate this possibility, various measurements were performed with both the MT and the ST1, while the transistor board was constantly heated and precision mode channels were used for the voltage supply.
In section 5.7.1, we saw that even for long evolution times of $T_{\mathrm{evol}} \approx 30\,\mathrm{s}$, magnetic field jitter only played a minor role in the observed phase stability in PnA measurements in the PT. In both the MT and the ST1, the stabilities were unfortunately much worse. As the phase jitter was also clearly scaling with the evolution time, the following explanations for this are possible:

1. Significantly worse field homogeneities or an increased temperature. As the trap setup is designed such that the PT is positioned in the most homogeneous region of the magnetic field and the homogeneity of the magnetic fields there is optimized by the B_2 coil, the magnetic inhomogeneity was significantly worse in the MT ($B_2 \approx 1.3\,\mu\mathrm{T\,mm^{-2}}$) and the ST1 ($B_2 \approx 0.5\,\mu\mathrm{T\,mm^{-2}}$) compared to the PT ($B_2 = 0.0024\,(24)\,\mu\mathrm{T\,mm^{-2}}$). Also, due to a technical problem, there was no electronic feedback available in the MT and ST1, resulting in an axial temperature of $\approx 4.2\,\mathrm{K}$, which is significantly higher than what was achievable in the PT ($T = 1.2\,(5)\,\mathrm{K}$). Although a detailed modeling of the involved phase jitter was not performed yet, this is a likely explanation for the observed phase jitter. However, if this is the origin of the phase jitter, at least for short term fluctuations one cannot hope to gain a benefit from comparing short term data.

2. The magnetic field jitter is actually higher. This could possibly be caused by magnetic material somewhere close to the traps, or by external fluctuations,

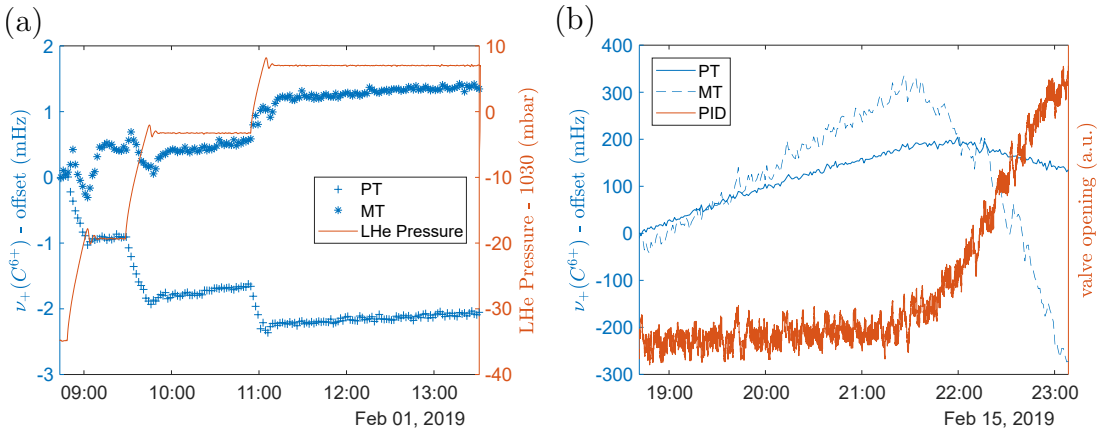

Figure 6.1: PnA in two traps. Shown are two example measurements, where simultaneous PnA measurements were performed in the PT and the MT. In (a), the pressure in the LHe reservoir was increased step-wise over a wide range, and the impact on the modified cyclotron frequency is measured with a relatively short evolution time of $T_{\text{evol}} = 2\,\text{s}$. The magnetic field in both traps behaves differently on magnetic field changes. In (b), the LHe pressure was stabilized, and the LN_2 pressure was unstabilized. However, the PID increasing the opening the exhaust valve hints to an increased ambient pressure towards the end of the measurement, which seems to have a large influence on the MT, but not on the PT.

which are shielded differently for the different traps. To measure this, a Helmholtz-coil was wound around the magnet and the shielding factor for homogeneous magnetic field changes was measured to be ≈ 146 in the PT and about the same in the neighboring ST1. In the MT, the shielding factor was lower by $\approx 25\%$. The difference is too small for external field jitter to play a role in the MT, but not in the PT.

From above considerations it is unlikely that we see any short term correlations of the magnetic field in neighboring traps. But what about long term drifts?
In figure 6.1, two example measurements, where simultaneous PnA measurements were performed in the PT and the MT are shown. There it becomes clear that both traps react differently to environmental changes. In order to benefit from this monitoring of the magnetic field, all environmental parameters which act differently on both traps need to be sufficiently stable. As this would probably increase the stability of the magnetic field in each of the traps and the drift of the magnetic field as estimated in section 5.7.2 was not limiting the statistical ratio, it is unclear if this technique can be used in a beneficial way in the near future.

6.2 Cooling Ions with Electrons

In section 5.7.1, we saw that the resolution of the PnA measurements is is limited by its temperatur, especially for the deuteron. Therefore, mass measurements

would greatly benefit from a reduced ion temperature. There are various approaches to achieve this, e.g. sympathetic cooling with laser cooled ions [94] or cooling with a cyclotron resonator [60], each with its own advantages and disadvantages. In the framework of this thesis a novel approach was started, where the axial motion of a cloud of electrons is cooled via electronic feedback and coupled to the cyclotron motion of an ion. Here, I want to sketch the idea behind this approach, present the measurements done in this direction and give a perspective for the future.

6.2.1 Equation of motion

A sketch of the principle is shown in figure 6.2. Electrons and the ion to be cooled are stored in independent Penning traps. The trap electrodes have capacitances C_i and effective electrode distances $D_i = |U_i/\frac{\partial U_i}{\partial z}|_{z=0}|$. The N electrons with charge Nq induce an image current on electrode 1, which is given by

$$i_{ind} = \frac{Nq}{D_1}\dot{z}, \tag{6.1}$$

with the electrons axial velocity $\dot{z}$. Here, the electrons are described in a simplified model as one particle with charge Ne and mass Nm_e. This implicitly assumes that only the collective motional mode of the cloud is in the considered frequency range and interactions with the internal modes are negligible. This current is translated into a voltage by the impedance $Z = -i/(\omega C_1)$ of the trap capacitance. It is then amplified by a factor A, phase shifted and fed back onto a second electrode. Both voltages cause a force on the electrons, given by

$$\begin{aligned} F_i &= \frac{qU_i}{D_i} \quad \text{, where} \\ U_1 &= \frac{-iqN}{\omega C_1 D_1}\dot{z}, \\ U_2 &= \frac{-Ae^{i\phi}qN}{\omega C_1 D_1}\dot{z}. \end{aligned} \tag{6.2}$$

The resulting equation of motion is then given by

$$\ddot{z}(t) = -\omega^2 z(t) + \left(\frac{-iq^2N}{\omega C_1 D_1^2 m} + \frac{A * e^{i\phi}q^2N}{\omega C_1 m D_1 D_2}\right)\dot{z}. \tag{6.3}$$

An imaginary part of the coefficient in front of $\dot{z}$ leads to a frequency shift. Therefore, one has an indicator to tune the phase such that $e^{i\phi} = 1$. This equation of motion results in a damping with rate

$$\tau_{\text{eff}} = \frac{m_e\omega}{q^2N}\frac{D_1D_2C_1}{A\,\text{Re}\,(e^{i\phi})}. \tag{6.4}$$

The damping rate scales as $1/N$, so using more electrons will lead to faster damping. Therefore, using as many electrons as possible is desirable. However, one has

Figure 6.2: Scetch of the setup for cooling ions with electrons. The electrons are axially by feeding the amplified and phase shifted signal they induce in electrode 1 back to electrode 2. Another electrode picks the electron signal up and is connected to a split electrode (4) of a neighboring trap, where an ion is stored. The coupling leads to an exchange of energy of the axial mode of the electrons with the cyclotron mode of the ion.

to guarantee that inside the volume filled by the electrons the electric field is sufficiently harmonic in order to have a coherent center of mass motion, which gives a practical limitation on the number of electrons. For the example calculations shown here, I used an estimate of $N = 1 \cdot 10^4$ electrons.

6.2.2 Temperature Limitation

The temperature reachable using this method is limited by the signal-to-noise ratio of the signal, which is fed back onto the second electrode. Here, I assume the use of a low-noise semiconductor amplifier based on a field-effect transistor. While a SQUID in principle can yield better signal to noise ratios, its use close to a high magnetic field is challenging.
The noise of a semiconductor amplifier in this frequency range can be modeled as consisting of two parts [52], noise that is present at the output stage and noise that is present at the input stage of the amplifier. The noise at the output stage is referred to as voltage noise. It is convenient to express it as a noise density at the input of the amplifier e_n. However, the voltage is not actually there, but added during the amplification process. Noise at the input stage can originate from currents in the gate or from voltage noise, which is fed back to the input through the Miller capacitance. It is referred to as current noise, and also denoted as a voltage noise density at the input stage $e_{n,I}$. This voltage can potentially be correlated to e_n, however, for the treatment shown here they are assumed to be uncorrelated. In the situation with feedback applied, both noise sources can heat the ions motion. However, Voltage noise can be reduced by cooling more slowly, while current noise provides a constant heating rate. Therefore, it is immediately clear that one has to adjust the amplification A and thus the cooling rate in order

to to minimize the temperature.
To quantify this and get an effective temperature caused by these noise sources, one can model the system as a resistor connected to electrode 1. The voltage noise density u_n of an resistor is given by

$$u_n = \sqrt{4k_bTR}, \tag{6.5}$$

with k_b being the Boltzmann constant and R the resistance. A system of N particles in a Penning trap dumping energy into an ohmic resistance has a cooling time constant of

$$\tau_R = \frac{mD^2}{Nq^2R}. \tag{6.6}$$

To get an effective temperature, the first step is comparing τ_R with τ_{eff}, which yields an effective resistance

$$R_{\text{eff}} = \frac{A^*}{\omega_z C_1}, \tag{6.7}$$

with $A^* = AD_1/D_2$. As a second step, one needs to model all heating processes as from electrode 1 and then compare the effective noise density to the one of a an ohmic resistor given in equation (6.5).
The force acting on the electrons caused by a voltage on electrode 2 is described by equation (6.2). The same force originating from a voltage on electrode 1 would thus be caused by a voltage $U_1 = \frac{D_1U_2}{D_2}$. The noise voltage Au_n on electrode 3 can be written as effective noise voltage $e_{n,\text{eff}}$ on electrode 1, which is given by

$$e_{n,\text{eff}} = \frac{AD_1e_n}{D_2} = A^*e_n. \tag{6.8}$$

The noise originating from currents in the gate $e_{n,I}$ is added in quadrature to the voltage noise, assuming both to be uncorrelated. Combining this with equation (6.5) and equation (6.7) one gets an effective temperature

$$T_{\text{eff.}} = \frac{\omega_z C_1}{4k_b}\left(A^*e_n^2 + \frac{e_{n,I}^2}{A^*}\right). \tag{6.9}$$

As expected, one is able to adjust A^* in order to get a minimal effective temperature. This minimal temperature is given by

$$T_{\min} = \frac{\omega_z C_1}{2k_b}e_ne_{n,I}, \tag{6.10}$$

and is reached for

$$A^* = \frac{e_{n,I}}{e_n}. \tag{6.11}$$

Interestingly, this minimal temperature is independent of the number of electrons used. However, for more electrons, the minimal temperature is reached faster. While the noise density of the cryo-amplifiers in use at LIONTRAP is in the order of $e_n \approx 500\,\text{pV}/\sqrt{\text{Hz}}$, the current noise is hard to estimate. However, as we do

not observe an impact of current noise on the temperature of our resonators, it is justified to assume this to be small. When taking a value of $e_{n,I}/e_n = 0.01 = A^*$, a trap capacitance of $C_1 = 10\,\mathrm{pF}$ and an axial frequency of $\omega_z = 2\pi \cdot 30\,\mathrm{MHz}$, one arrives at a lower limit for the temperature of $\approx 170\,\mathrm{mK}$. The cooling time constant corresponding to this temperature can be estimated using $D_1 = D_2 = 10\,\mathrm{mm}$ and $N = 1 \cdot 10^4$ to be $\tau_{eff} \approx 67\,\mathrm{ms}$, which is feasible. However, this stresses that an ensemble of electrons is needed, because for $N = 1$ this cooling time constant would be in the order of 11 min, which is unfeasible long. One should note that this can be shortened by increasing the amplification A, at the cost of an increased temperature.

6.2.3 Coupling of Electrons and Ions

The coupling between particles in adjacent traps has been proposed and theoretically treated by Heinzen and Wineland [95]. In their treatment they consider one of the particles as being laser-cooled to the quantum mechanical ground state and ask if it is possible to prepare the other particle also in the quantum mechanical ground state. When we translate his ideas into our concept, one has to replace the laser-cooled ion with a number of electrons being cooled by electronic feedback.
In the case of both particles having identical frequencies ω, this results in an oscillatory exchange of energy with a frequency Ω given by

$$\begin{aligned} \Omega &= \frac{g^2}{2\omega} \quad \text{, where} \\ g^2 &= \frac{q_1 q_2 \sqrt{N}}{C_c D_3 D_4 \sqrt{m_1 m_2}}. \end{aligned} \tag{6.12}$$

Here, q_1 and q_2 are the charges of an electron and the ion to be cooled, respectively. C_C is the capacitance of the connected electrodes, through which the coupling occurs, and D_3 and D_4 are the respective effective electrode distances. Note that D_4 refers to the effective electrode distance in radial direction, in order to cool the modified cyclotron mode of ions. Assuming $D_3 = D_4 = 5\,\mathrm{mm}$ and a single deuteron, this exchange of energy occurs on a timescale of $2\pi/\Omega \approx 13\,\mathrm{s}$. Note that this effective electrode distance for the radial motion is not achievable in the PT of LIONTRAP, where the radial effective electrode distance of the split ring electrode is $\approx 38\,\mathrm{mm}$, but would require a dedicated coupling trap.
In the analytical treatment in [95] it is assumed that the cooling is turned off during the coupling and vice versa. While this switching is necessary to achieve ground-state cooling, it is technically very hard to achieve. If the coupling is constantly there, and much slower than the cooling of the electron cloud $\tau \gg 1/\Omega$, solving the coupled equations of motion yields and effective cooling time constant for the ion of

$$\tau_{\mathrm{ion}} = \frac{\omega^2}{\tau g^4} \approx 15\,\mathrm{s}. \tag{6.13}$$

For the scenario outlined here, this is only slightly larger than the time constant of the exchange of energy without feedback. This damping time is faster than typical damping constants for a cyclotron resonator. The electrons can furthermore be put easily in resonance with any ion by changing the trap voltage. Also, the modified cyclotron mode is directly thermalized, not through the axial mode. When transferring the $T_+ \approx 170\,\mathrm{mK}$ to the axial mode, with the frequency conditions at LIONTRAP a temperature of $T_z = \frac{\nu_z}{\nu_+} T_+ \approx 2.7\,\mathrm{mK}$, which would be a factor of ≈ 400 lower than the current temperature.

6.2.4 Experimental Steps and Limitations

From above considerations the technique looks promising, but can we implement it in the experiment? One obvious limitation is voltage stability. In order for the cooling to work, the electrons' axial frequency needs to jitter less than approximately the inverse cooling time. For the cooling time of 67 ms given above, this would at $\nu_z = 30\,\mathrm{MHz}$ translate into a voltage stability of better than $8 \cdot 10^{-7}$. If one aims to couple to ions, the 15 s becomes the relevant timescale, corresponding to a voltage stability of better than $4 \cdot 10^{-9}$. The UM1-14 can achieve stabilities in the 10^{-7} range, however, reaching stabilities of 10^{-9} is very challenging. That is the reason why the transistor board described in section 3.4.3 and evaluated in section 4.7 was implemented. As described there, it was not possible to stabilize the voltage to the desired extend. However, with new ideas on how to stabilize the trap voltage, one can investigate this electron cooling further. An optimized coupling sequence might also significantly shorten the time scale of the coupling and thus relax the demands on voltage stability, as shown in a recent work [96] at ALPHATRAP [97] in the context of laser-cooled ions.
We showed at LIONTRAP that we can produce and store clouds of electrons, which were detected by using a cyclotron resonator for ions, connected to an off center electrode. However, during these test productions, another problem became clear: at least in resonance with the tank circuit, the electrons get lost after a few minutes. When the electrons are produced, detected and shifted out of resonance, their life-time is significantly prolonged. One possible explanation would be that the problem lies in the more complicated mode structure of the electrons' axial motion. If and how this will affect the proposed cooling method needs to be investigated in future measurements.

6.3 Summary

In this thesis, I presented various experimental improvements and measurements culminating in the measurement of the deuteron's atomic mass with an unprecedented precision. One of the highlights is the in-situ tuning of the residual magnetic inhomogeneity B_2. With the reduced B_2, the systematic effect which was so far limiting mass measurements at LIONTRAP was reduced to a negligible level. The

mass measurement of the deuteron was a factor of 2.4 more precise then the previous best value. The LIONTRAP value presented here and the previous best value deviate by $4.8\,\sigma$. With a direct measurement of the mass of HD^+ also presented in this thesis, I was able to show consistency between the masses of the proton, the deuteron, and HD^+, all reported by LIONTRAP. This is a profound consistency check substantiating our measurement methods. Furthermore, the consistency with the deuteron-to-proton mass measurement by the FSU allowed for a least square adjustment in the light ion mass sector, yielding a reduction of the uncertainty of the proton mass by a factor of 2 compared to our direct measurement [7]. I discussed the implications of these new values on the mass of the neutron and the spectroscopy of rovibrational states in HD^+.

The analysis of the data in the deuteron campaign yielded starting points to improve on further mass measurements at LIONTRAP. Among these, one of the next projects will be a measurement of ^{3}He, in order to clear up the remaining tension in the light ion mass puzzle.

Publications

While working on this thesis, I contributed to the following publications:

1. S. Rau et al. "Penning trap mass measurements of the deuteron and the HD^+ molecular ion". In: Nature 585.7823 (2020), pp. 43–47. url: https://doi.org/10.1038/s41586-020-2628-7. [6]

   - I was responsible for the experimental setup, the data taking, the subsequent analysis and wrote the manuscript. The data and findings of this article are fully presented in this thesis.

2. F. Heiße et al. "High-Precision Measurement of the Proton's Atomic Mass". In: Phys. Rev. Lett. 119 (3 2017), p. 033001. url: https://link.aps.org/doi/10.1103/PhysRevLett.119.033001. [8]

   - I took part in the data taking, the analysis and the revision of the manuscript. In this thesis, only the main results of this article are used.

3. F. Heiße et al. "High-precision mass spectrometer for light ions". In: Phys. Rev. A 100 (2 2019), p. 022518. url: https://link.aps.org/doi/10. 1103/PhysRevA.100.022518. [7]

   - I took part in the data taking, the analysis and the revision of the manuscript. In this thesis, only the main results of this article are used.

4. M. Schuh et al. "Image charge shift in high-precision Penning traps". In: Phys. Rev. A 100 (2 2019), p. 023411. url: https://link.aps.org/doi/10.1103/PhysRevA.100.023411. [63]

   - In this article, an extensive theoretical analysis of the image charge shift is presented together with a measurement of this shift at LIONTRAP. I contributed in the experimental part of the paper, where I took part in the data taking and analysis. Additionally, I discussed the whole manuscript with the other authors.

5. D. A. Glazov et al. "g Factor of Lithiumlike Silicon: New Challenge to Bound- State QED". In: Phys. Rev. Lett. 123 (17 2019), p. 173001. url: https: //link.aps.org/doi/10.1103/PhysRevLett.123.173001. [98]

   - The data taking for this article occurred before I joined LIONTRAP. I took part in the analysis of systematic shifts and discussed the manuscript with the other authors.

Bibliography

[1] M. K. Gaillard, P. D. Grannis, and F. J. Sciulli. "The standard model of particle physics". In: *Rev. Mod. Phys.* 71 (2 1999), pp. 96–111. URL: https://link.aps.org/doi/10.1103/RevModPhys.71.S96.

[2] S. Dürr et al. "Ab Initio Determination of Light Hadron Masses". In: *Science* 322.5905 (2008), pp. 1224–1227. URL: https://science.sciencemag.org/content/322/5905/1224.

[3] C. G. Parthey et al. "Improved Measurement of the Hydrogen $1S - -2S$ Transition Frequency". In: *Phys. Rev. Lett.* 107 (20 2011), p. 203001. URL: https://link.aps.org/doi/10.1103/PhysRevLett.107.203001.

[4] A. Matveev et al. "Precision Measurement of the Hydrogen $1S-2S$ Frequency via a 920-km Fiber Link". In: *Phys. Rev. Lett.* 110 (23 2013), p. 230801. URL: https://link.aps.org/doi/10.1103/PhysRevLett.110.230801.

[5] A. Beyer et al. "The Rydberg constant and proton size from atomic hydrogen". In: *Science* 358.6359 (2017), pp. 79–85. URL: https://science.sciencemag.org/content/358/6359/79.

[6] S. Rau et al. "Penning trap mass measurements of the deuteron and the HD^+ molecular ion". In: *Nature* 585.7823 (2020), pp. 43–47. URL: https://doi.org/10.1038/s41586-020-2628-7.

[7] F. Heiße et al. "High-precision mass spectrometer for light ions". In: *Phys. Rev. A* 100 (2 2019), p. 022518. URL: https://link.aps.org/doi/10.1103/PhysRevA.100.022518.

[8] F. Heiße et al. "High-Precision Measurement of the Proton's Atomic Mass". In: *Phys. Rev. Lett.* 119 (3 2017), p. 033001. URL: https://link.aps.org/doi/10.1103/PhysRevLett.119.033001.

[9] E. G. Myers. "High-Precision Atomic Mass Measurements for Fundamental Constants". In: *Atoms* 7.1 (2019), p. 37. URL: http://dx.doi.org/10.3390/atoms7010037.

[10] F. Heiße. "High-precision measurement of the proton's atomic mass". PhD thesis. Ruprecht-Karls-Universität Heidelberg, 2019. URL: http://hdl.handle.net/11858/00-001M-0000-002D-A0E2-D.

[11] Y. Fukuda et al. "Measurements of the Solar Neutrino Flux from Super-Kamiokande's First 300 Days". In: *Phys. Rev. Lett.* 81 (6 1998), pp. 1158–1162. URL: https://link.aps.org/doi/10.1103/PhysRevLett.81.1158.

[12] Q. R. Ahmad et al. “Direct Evidence for Neutrino Flavor Transformation from Neutral-Current Interactions in the Sudbury Neutrino Observatory”. In: *Phys. Rev. Lett.* 89 (1 2002), p. 011301. URL: https://link.aps.org/doi/10.1103/PhysRevLett.89.011301.

[13] Q. R. Ahmad et al. “Measurement of Day and Night Neutrino Energy Spectra at SNO and Constraints on Neutrino Mixing Parameters”. In: *Phys. Rev. Lett.* 89 (1 2002), p. 011302. URL: https://link.aps.org/doi/10.1103/PhysRevLett.89.011302.

[14] E. W. Otten and C. Weinheimer. “Neutrino mass limit from tritium β decay”. In: *Reports on Progress in Physics* 71.8 (2008), p. 086201. URL: https://doi.org/10.1088%2F0034-4885%2F71%2F8%2F086201.

[15] G. Drexlin. “Direct neutrino mass searches”. In: *Nuclear Physics B - Proceedings Supplements* 138 (2005). Proceedings of the Eighth International Workshop on Topics in Astroparticle and Undeground Physics, pp. 282–288. URL: http://www.sciencedirect.com/science/article/pii/S0920563204006292.

[16] M. Aker et al. “Improved Upper Limit on the Neutrino Mass from a Direct Kinematic Method by KATRIN”. In: *Phys. Rev. Lett.* 123 (22 2019), p. 221802. URL: https://link.aps.org/doi/10.1103/PhysRevLett.123.221802.

[17] E. G. Myers, A. Wagner, H. Kracke, and B. A. Wesson. “Atomic Masses of Tritium and Helium-3”. In: *Phys. Rev. Lett.* 114 (1 2015), p. 013003. URL: https://link.aps.org/doi/10.1103/PhysRevLett.114.013003.

[18] S. L. Zafonte and R. S. Van Dyck Jr. “Ultra-precise single-ion atomic mass measurements on deuterium and helium-3”. In: *Metrologia* 52.2 (2015), p. 280. URL: http://stacks.iop.org/0026-1394/52/i=2/a=280.

[19] S. Hamzeloui, J. A. Smith, D. J. Fink, and E. G. Myers. “Precision mass ratio of $^3He^+$ to HD^+”. In: *Phys. Rev. A* 96 (6 2017), p. 060501. URL: https://link.aps.org/doi/10.1103/PhysRevA.96.060501.

[20] R. S. Van Dyck Jr., D. L. Farnham, S. L. Zafonte, and P. B. Schwinberg. “High precision Penning trap mass spectroscopy and a new measurement of the proton’s atomic mass”. In: *AIP Conf. Proc.* 457.1 (1999), pp. 101–110. URL: http://aip.scitation.org/doi/abs/10.1063/1.57450.

[21] D. O’Leary. “The deeds to deuterium”. In: *Nature Chemistry* 4.3 (2012), pp. 236–236. URL: https://doi.org/10.1038/nchem.1273.

[22] H. C. Urey, F. G. Brickwedde, and G. M. Murphy. “A Hydrogen Isotope of Mass 2 and its Concentration”. In: *Phys. Rev.* 40 (1 1932), pp. 1–15. URL: https://link.aps.org/doi/10.1103/PhysRev.40.1.

[23] R. T. Birge and D. H. Menzel. “The Relative Abundance of the Oxygen Isotopes, and the Basis of the Atomic Weight System”. In: *Phys. Rev.* 37 (12 1931), pp. 1669–1671. URL: https://link.aps.org/doi/10.1103/PhysRev.37.1669.2.

[24] R. T. Birge. “Probable Values of the General Physical Constants”. In: *Rev. Mod. Phys.* 1 (1 1929), pp. 1–73. URL: https://link.aps.org/doi/10.1103/RevModPhys.1.1.

[25] F. W. Aston. “Bakerian Lecture. - A new mass-spectrograph and the whole number rule”. In: *Proceedings of the Royal Society of London. Series A, Containing Papers of a Mathematical and Physical Character* 115.772 (1927), pp. 487–514. URL: https://royalsocietypublishing.org/doi/abs/10.1098/rspa.1927.0106.

[26] H. C. Urey, G. M. Murphy, and F. G. Brickwedde. “A Name and Symbol for H^2”. In: *The Journal of Chemical Physics* 1.7 (1933), pp. 512–513. URL: https://doi.org/10.1063/1.1749326.

[27] A. Antognini et al. “Proton Structure from the Measurement of 2S-2P Transition Frequencies of Muonic Hydrogen”. In: *Science* 339.6118 (2013), pp. 417–420. URL: https://science.sciencemag.org/content/339/6118/417.

[28] Y. I. Neronov and S. G. Karshenboim. “NMR spectroscopy of hydrogen deuteride and magnetic moments of deuteron and triton”. In: *Phys. Lett. A* 318.1 (2003), pp. 126–132. URL: http://www.sciencedirect.com/science/article/pii/S0375960103014087.

[29] J. Biesheuvel et al. “Probing QED and fundamental constants through laser spectroscopy of vibrational transitions in HD+”. In: *Nature Communications* 7.1 (2016), p. 10385. URL: https://doi.org/10.1038/ncomms10385.

[30] S. Alighanbari, M. G. Hansen, V. I. Korobov, and S. Schiller. “Rotational spectroscopy of cold and trapped molecular ions in the Lamb–Dicke regime”. In: *Nat. Phys.* 14.6 (2018), pp. 555–559. URL: https://doi.org/10.1038/s41567-018-0074-3.

[31] S. Alighanbari et al. “Precise test of quantum electrodynamics and determination of fundamental constants with HD+ ions”. In: *Nature* 581.7807 (2020), pp. 152–158. URL: https://doi.org/10.1038/s41586-020-2261-5.

[32] S. Patra et al. “Proton-electron mass ratio from laser spectroscopy of HD+ at the part-per-trillion level”. In: *Science* (2020). URL: https://science.sciencemag.org/content/early/2020/07/29/science.aba0453.

[33] E. G. Kessler et al. “The deuteron binding energy and the neutron mass”. In: *Phys. Lett. A* 255.4 (1999), pp. 221–229. URL: http://www.sciencedirect.com/science/article/pii/S037596019900078X.

[34] E.G. Kessler et al. “The GAMS4 flat crystal facility”. In: *Nuclear Instruments and Methods in Physics Research Section A: Accelerators, Spectrometers, Detectors and Associated Equipment* 457.1 (2001), pp. 187–202. URL: http://www.sciencedirect.com/science/article/pii/S0168900200007531.

[35] M. S. Dewey et al. “Precision measurement of the ^{29}Si, ^{33}S, and ^{36}Cl binding energies”. In: *Phys. Rev. C* 73 (4 2006), p. 044303. URL: https://link.aps.org/doi/10.1103/PhysRevC.73.044303.

[36] M. Jentschel and K. Blaum. “Balancing energy and mass with neutrons”. In: *Nat. Phys.* 14.5 (2018), pp. 524–524. URL: https://doi.org/10.1038/s41567-018-0132-x.

[37] S. Rainville et al. “A direct test of E=mc2”. In: *Nature* 438.7071 (2005), pp. 1096–1097. URL: https://doi.org/10.1038/4381096a.

[38] J. Krempel. “A new spectrometer to measure the molar Planck constant”. PhD thesis. LMU München: Fakultät für Physik, 2011.

[39] K. Blaum. “High-accuracy mass spectrometry with stored ions”. In: *Physics Reports* 425.1 (2006), pp. 1–78. URL: http://www.sciencedirect.com/science/article/pii/S0370157305004643.

[40] L. S. Brown and G. Gabrielse. “Precision spectroscopy of a charged particle in an imperfect Penning trap”. In: *Phys. Rev. A* 25 (4 1982), pp. 2423–2425. URL: https://link.aps.org/doi/10.1103/PhysRevA.25.2423.

[41] J. L. Verdú Galiana. “Ultrapräzise Messung des elektronischen g-Faktors in wasserstoffähnlichem Sauerstoff”. PhD thesis. Johannes Gutenberg-Universität Mainz, 2003.

[42] G. Gabrielse. “Why Is Sideband Mass Spectrometry Possible with Ions in a Penning Trap?” In: *Phys. Rev. Lett.* 102 (17 2009), p. 172501. URL: https://link.aps.org/doi/10.1103/PhysRevLett.102.172501.

[43] M. Mukherjee et al. “ISOLTRAP: An on-line Penning trap for mass spectrometry on short-lived nuclides”. In: *Eur. Phys. J. A* 35.1 (2008), pp. 1–29. URL: https://doi.org/10.1140/epja/i2007-10528-9.

[44] A. G. Marshall, C. L. Hendrickson, and G. S. Jackson. “Fourier transform ion cyclotron resonance mass spectrometry: A primer”. In: *Mass Spectrometry Reviews* 17.1 (1998), pp. 1–35. URL: https://onlinelibrary.wiley.com/doi/abs/10.1002/%28SICI%291098-2787%281998%2917%3A1%3C1%3A%3AAID-MAS1%3E3.0.CO%3B2-K.

[45] L. S. Brown and G. Gabrielse. “Geonium theory: Physics of a single electron or ion in a Penning trap”. In: *Rev. Mod. Phys.* 58 (1 1986), pp. 233–311. URL: https://link.aps.org/doi/10.1103/RevModPhys.58.233.

[46] J. Ketter et al. “First-order perturbative calculation of the frequency-shifts caused by static cylindrically-symmetric electric and magnetic imperfections of a Penning trap”. In: *International Journal of Mass Spectrometry* 358 (2014), pp. 1–16. URL: http://www.sciencedirect.com/science/article/pii/S1387380613003722.

[47] K. S. Viswanathan. “The theory of the anharmonic oscillator”. In: *Proceedings of the Indian Academy of Sciences - Section A* 46.3 (1957), pp. 203–217. URL: https://doi.org/10.1007/BF03045969.

[48] W. Demtröder. *Experimentalphysik 2, Elektrizität und Optik*. Springer Spektrum, 2017.

[49] W. Shockley. “Currents to Conductors Induced by a Moving Point Charge”. In: *Journal of Applied Physics* 9.10 (1938), pp. 635–636. URL: https://doi.org/10.1063/1.1710367.

[50] J. B. Johnson. “Thermal Agitation of Electricity in Conductors”. In: *Phys. Rev.* 32 (1 1928), pp. 97–109. URL: https://link.aps.org/doi/10.1103/PhysRev.32.97.

[51] H. Nyquist. “Thermal Agitation of Electric Charge in Conductors”. In: *Phys. Rev.* 32 (1 1928), pp. 110–113. URL: https://link.aps.org/doi/10.1103/PhysRev.32.110.

[52] S. Sturm. “The g-factor of the electron bound in $^{28}Si^{13+}$: The most stringent test of bound-state quantum electrodynamics”. PhD thesis. Johannes Gutenberg-Universität Mainz, 2012.

[53] D. J. Wineland and H. G. Dehmelt. “Principles of the stored ion calorimeter”. In: *J. Appl. Phys.* 46.2 (1975), pp. 919–930. URL: https://doi.org/10.1063/1.321602.

[54] F. Köhler-Langes. “Bound-Electron g-Factor Measurements for the Determination of the Electron Mass and Isotope Shifts in Highly Charged Ions”. PhD thesis. Ruprecht-Karls-Universität Heidelberg, 2015. URL: http://hdl.handle.net/11858/00-001M-0000-0029-2933-3.

[55] S. Braun et al. “Negative Absolute Temperature for Motional Degrees of Freedom”. In: *Science* 339.6115 (2013), pp. 52–55. URL: https://science.sciencemag.org/content/339/6115/52.

[56] E. A. Cornell, R. M. Weisskoff, K. R. Boyce, and D. E. Pritchard. “Mode coupling in a Penning trap: π pulses and a classical avoided crossing”. In: *Phys. Rev. A* 41 (1 1990), pp. 312–315. URL: https://link.aps.org/doi/10.1103/PhysRevA.41.312.

[57] “The Dressed Atom Approach”. In: *Atom—Photon Interactions*. John Wiley & Sons, Ltd, 2008. Chap. 6, pp. 407–514. URL: https://onlinelibrary.wiley.com/doi/abs/10.1002/9783527617197.ch6.

[58] I. Arapoglou. “First measurement of the ground-state g-factor of boronlike argon $^{40}Ar^{13+}$ in Alphatrap”. PhD thesis. Ruprecht-Karls-Universität Heidelberg, 2019. URL: http://hdl.handle.net/21.11116/0000-0005-599C-8.

[59] S. Ulmer et al. “High-precision comparison of the antiproton-to-proton charge-to-mass ratio”. In: *Nature* 524.7564 (2015), pp. 196–199. URL: http://dx.doi.org/10.1038/nature14861.

[60] G. Schneider et al. “Double-trap measurement of the proton magnetic moment at 0.3 parts per billion precision”. In: *Science* 358.6366 (2017), pp. 1081–1084. URL: https://science.sciencemag.org/content/358/6366/1081.

[61] C. Smorra et al. “A parts-per-billion measurement of the antiproton magnetic moment”. In: *Nature* 550.7676 (2017), pp. 371–374. URL: https://doi.org/10.1038/nature24048.

[62] S. Sturm et al. “High-precision measurement of the atomic mass of the electron”. In: *Nature* 506.7489 (2014), pp. 467–470. URL: https://doi.org/10.1038/nature13026.

[63] M. Schuh et al. “Image charge shift in high-precision Penning traps”. In: *Phys. Rev. A* 100 (2 2019), p. 023411. URL: https://link.aps.org/doi/10.1103/PhysRevA.100.023411.

[64] S. Sturm, A. Wagner, B. Schabinger, and K. Blaum. “Phase-Sensitive Cyclotron Frequency Measurements at Ultralow Energies”. In: *Phys. Rev. Lett.* 107 (14 2011), p. 143003. URL: https://link.aps.org/doi/10.1103/PhysRevLett.107.143003.

[65] J. Ketter et al. “Classical calculation of relativistic frequency-shifts in an ideal Penning trap”. In: *International Journal of Mass Spectrometry* 361 (2014), pp. 34–40. URL: http://www.sciencedirect.com/science/article/pii/S1387380614000426.

[66] R. S. Van Dyck, F. L. Moore, D. L. Farnham, and P. B. Schwinberg. “Number dependency in the compensated Penning trap”. In: *Phys. Rev. A* 40 (11 1989), pp. 6308–6313. URL: https://link.aps.org/doi/10.1103/PhysRevA.40.6308.

[67] J. K. Thompson, S. Rainville, and D. E. Pritchard. “Cyclotron frequency shifts arising from polarization forces”. In: *Nature* 430.6995 (2004), pp. 58–61. URL: https://doi.org/10.1038/nature02682.

[68] M. Cheng et al. “Dipole moments and orientation polarizabilities of diatomic molecular ions for precision atomic mass measurement”. In: *Phys. Rev. A* 75 (1 2007), p. 012502. URL: https://link.aps.org/doi/10.1103/PhysRevA.75.012502.

[69] S. Schiller, D. Bakalov, A. K. Bekbaev, and V. I. Korobov. "Static and dynamic polarizability and the Stark and blackbody-radiation frequency shifts of the molecular hydrogen ions H_2^+, HD^+, and D_2^+". In: *Phys. Rev. A* 89 (5 2014), p. 052521. URL: https://link.aps.org/doi/10.1103/PhysRevA.89.052521.

[70] S. Sturm et al. "*g*-Factor of Hydrogenlike $^{28}Si^{13+}$". In: *Phys. Rev. Lett.* 107 (2 2011), p. 023002. URL: https://link.aps.org/doi/10.1103/PhysRevLett.107.023002.

[71] N. Hermanspahn. "Aufbau eines Tieftemperaturkryostaten zum Betrieb einer Penningfalle." Diploma thesis. Johannes Gutenberg-Universität Mainz, 1996.

[72] H. Preston-Thomas. "The International Temperature Scale of 1990 (ITS-90)". In: *Metrologia* 27.1 (1990), pp. 3–10. URL: https://doi.org/10.1088%2F0026-1394%2F27%2F1%2F002.

[73] Bureau International des Poids et Mesures. *SI Brochure: The International System of Units (SI), 9th edition*. 2020. URL: https://www.bipm.org/en/publications/si-brochure/.

[74] S. Streubel. "Kontrolle der Umwelteinflüsse auf THe-Trap am Beispiel der Bestimmung des Massenverhältnisses von Kohlenstoff-12 zu Sauerstoff-16". PhD thesis. Ruprecht-Karls-Universität Heidelberg, 2014. URL: http://hdl.handle.net/11858/00-001M-0000-0019-1781-7.

[75] S. Streubel et al. "Toward a more accurate Q value measurement of tritium: status of THe-Trap". In: *Applied Physics B* 114.1 (2014), pp. 137–145. URL: https://doi.org/10.1007/s00340-013-5669-x.

[76] B. Schabinger et al. "Towards *g*-factor determination of the electron bound in highly-charged calcium ions". In: *Journal of Physics: Conference Series* 58 (2007), pp. 121–124. URL: https://doi.org/10.1088%2F1742-6596%2F58%2F1%2F021.

[77] S. Sturm et al. "On *g*-factor experiments with individual ions". In: *J. Phys. B* 43.7 (2010), p. 074016. URL: https://doi.org/10.1088%2F0953-4075%2F43%2F7%2F074016.

[78] Ensinger GmbH, Nufringen, Germany. URL: http://www.ensinger-online.com/de (visited on 04/30/2017).

[79] J. Meija et al. "Atomic weights of the elements 2013 (IUPAC Technical Report)". In: *Pure and Applied Chemistry* 88.3 (2016), pp. 265–291. URL: https://www.degruyter.com/view/journals/pac/88/3/article-p265.xml.

[80] R. Haas et al. "Development and characterization of a Drop-on-Demand inkjet printing system for nuclear target fabrication". In: *Nucl. Instrum. Meth. A* 874 (2017), pp. 43–49. URL: http://www.sciencedirect.com/science/article/pii/S0168900217308987.

[81] S. Rainville. “A two-ion balance for high precision mass spectrometry”. PhD thesis. Massachusetts Institute of Technology, 2003.

[82] Panasonic Industry. Datasheet Stacked Metallized PPS Film Chip Capacitor, ECHU(X) series. 2017. URL: http://industrial.panasonic.com/cdbs/www-data/pdf/RDI0000/ABD0000C173.pdf.

[83] N. M. Zimmerman. “Capacitors with very low loss: cryogenic vacuum-gap capacitors”. In: *IEEE Transactions on Instrumentation and Measurement* 45.5 (1996), pp. 841–846.

[84] S. Rainville, J. K. Thompson, and D. E. Pritchard. “An Ion Balance for Ultra-High-Precision Atomic Mass Measurements”. In: *Science* 303.5656 (2004), pp. 334–338. URL: https://science.sciencemag.org/content/303/5656/334.

[85] P. J. Mohr, D. B. Newell, B. N. Taylor, and E. Tiesinga. *CODATA Recommended Values of the Fundamental Physical Constants: 2018*. 2019. URL: http://physics.nist.gov/constants.

[86] A. Kramida, J. Ralchenko, J. Reader, and the NIST ASD Team. *NIST Atomic Spectra Database*. 2017. URL: http://physics.nist.gov/asd.

[87] D. J. Fink and E. G. Myers. “Deuteron-to-Proton Mass Ratio from the Cyclotron Frequency Ratio of H_2^+ to D^+ with H_2^+ in a Resolved Vibrational State”. In: *Phys. Rev. Lett.* 124 (1 2020), p. 013001. URL: https://link.aps.org/doi/10.1103/PhysRevLett.124.013001.

[88] P. J. Mohr, D. B. Newell, and B. N. Taylor. “CODATA recommended values of the fundamental physical constants: 2014”. In: *Rev. Mod. Phys.* 88 (3 2016), p. 035009. URL: https://link.aps.org/doi/10.1103/RevModPhys.88.035009.

[89] H. Olivares P. and D. Baye. “Dipole transitions in the bound rotational-vibrational spectrum of the heteronuclear molecular ion HD^+”. In: *Phys. Rev. A* 88 (3 2013), p. 032502. URL: https://link.aps.org/doi/10.1103/PhysRevA.88.032502.

[90] V. I. Korobov, L. Hilico, and J.-Ph. Karr. “Fundamental Transitions and Ionization Energies of the Hydrogen Molecular Ions with Few ppt Uncertainty”. In: *Phys. Rev. Lett.* 118 (23 2017), p. 233001. URL: https://link.aps.org/doi/10.1103/PhysRevLett.118.233001.

[91] W. Huang. “Direct Mass Measurements and Global Evaluation of Atomic Masses”. PhD thesis. Université Paris-Saclay, 2018. URL: https://cds.cern.ch/record/2654978.

[92] E. G. Kessler et al. “The Lattice Spacing Variability of Intrinsic Float-Zone Silicon”. In: *J. Res. Natl. Inst. Stan.* 122.24 (2017). URL: https://doi.org/10.6028/jres.122.024.

[93] F. Köhler et al. “The electron mass fromg-factor measurements on hydrogen-like carbon $^{1}2C^{5+}$”. In: *J. Phys. B* 48.14 (2015), p. 144032. URL: https://doi.org/10.1088%2F0953-4075%2F48%2F14%2F144032.

[94] A. Egl. “High-Precision Laser Spectroscopy of the Fine Structure in $^{40}Ar^{13+}$ at ALPHATRAP”. PhD thesis. Ruprecht-Karls-Universität Heidelberg, 2020. URL: http://hdl.handle.net/21.11116/0000-0006-49C2-D.

[95] D. J. Heinzen and D. J. Wineland. “Quantum-limited cooling and detection of radio-frequency oscillations by laser-cooled ions”. In: *Phys. Rev. A* 42 (5 1990), pp. 2977–2994. URL: https://link.aps.org/doi/10.1103/PhysRevA.42.2977.

[96] B. Tu et al. “A Tank-Circuit Assisted Coupling Method for Sympathetic Laser Cooling”. In: *submitted to Phys. Rev. Lett.* (2020).

[97] S. Sturm et al. “The ALPHATRAP experiment”. In: *Eur. Phys. J. Spec. Top.* 227.13 (2019), pp. 1425–1491. URL: https://doi.org/10.1140/epjst/e2018-800225-2.

[98] D. A. Glazov et al. “g Factor of Lithiumlike Silicon: New Challenge to Bound-State QED”. In: *Phys. Rev. Lett.* 123 (17 2019), p. 173001. URL: https://link.aps.org/doi/10.1103/PhysRevLett.123.173001.

List of Figures

List of Tables

A Appendix

A.1 Approximation Formulas Invariance Theorem

In this section, I describe the derivation of the approximation formulas in equation (2.20) of section 2.1.2.
Starting point are the equations (9-11) of reference [40]. With the notations used within this thesis, they are:

$$\omega_+^2\omega_z^2 + \omega_-^2 = \frac{1}{4}\omega_{z,0}\left(1-\epsilon^2\right) \tag{A.1a}$$

$$\begin{aligned}\omega_+^2\omega_z^2 + \omega_+^2\omega_-^2 + \omega_z^2\omega_-^2 = \omega_c^2\omega_{z,0}^2\left(1 - \frac{3}{2}\sin^2(\theta) - \frac{1}{2}\epsilon\sin^2(\theta)\cos(2\phi)\right)\\ - \frac{3}{4}\omega_{z,0}^4\left(1+\frac{1}{3}\epsilon^2\right)\end{aligned} \tag{A.1b}$$

$$\omega_+^2 + \omega_z^2 + \omega_-^2 = \omega_c^2. \tag{A.1c}$$

Here, ω_+, ω_z and ω_- denote the frequencies of the imperfect trap, ω_c is the free space cyclotron frqeuency and $\omega_{z,0}$ is the axial frequency for $\epsilon = 0$ and $\theta = 0$. The formulas in equation (A.1) are exact, in a sense that they do not contain any approximation. However, solving them is not straight forward. To get the dependence for small angles $\theta \ll 1$ and small deformations $\epsilon \ll 1$, I used the following ansatz:

$$\omega_+ = \omega_{+,0} + \Delta\omega_+ \tag{A.2a}$$

$$\omega_z = \omega_{z,0} + \Delta\omega_z \tag{A.2b}$$

$$\omega_- = \omega_{-,0} + \Delta\omega_-. \tag{A.2c}$$

Again, $\omega_{\pm,0}$ denotes the corresponding frequency for $\epsilon = 0$ and $\theta = 0$. Putting this ansatz into equation (A.1) and using $\omega_{z,0}^2 = 2\omega_{+,0}\omega_{-,0}$ yields

$$\omega_+^2\Delta\omega_+ + \omega_z^2\Delta\omega_z + \omega_-^2\Delta\omega_- = 0 \tag{A.3a}$$

$$\Delta\omega_+ + \Delta\omega_z + \Delta\omega_- = -\epsilon^2 \tag{A.3b}$$

$$\begin{aligned}\Delta\omega_z\left(2\omega_+^2 + 2\omega_-^2\right) + \Delta\omega_+\left(\omega_z^2/2 + 2\omega_+^2\right) + \Delta\omega_-\left(\omega_z^2/2 + 2\omega_-^2\right) =\\ \omega_c^2\left(-\frac{3}{2}\sin^2(\theta) - \frac{1}{2}\epsilon\sin^2(\theta)\cos(2\phi)\right) - \frac{1}{4}\omega_z^2\epsilon^2,\end{aligned} \tag{A.3c}$$

where I omitted the zeroes since all quantities without zero have been eliminated. This system of equation can be solved analytically, giving rather lengthy expressions for the frequency shifts. However, for $\omega_c \approx \omega_+ \gg \omega_z \gg \omega_-$ they reduce to

equation (2.20) in section 2.1.2, repeated here for convenience:

$$\Delta\omega_+ = \frac{\omega_{z,0}^2}{\omega_{+,0}}\frac{3}{4}\theta^2\left(1+\frac{1}{3}\epsilon\cos(2\phi)\right) + \frac{\omega_{-,0}^2}{2\omega_{+,0}}\epsilon^2 \tag{A.4a}$$

$$\Delta\omega_z = -\frac{3}{4}\omega_{z,0}\theta^2\left(1+\frac{1}{3}\epsilon\cos(2\phi)\right) \tag{A.4b}$$

$$\Delta\omega_- = \frac{3}{4}\omega_{-,0}\theta^2\left(1+\frac{1}{3}\epsilon\cos(2\phi)\right) + \frac{1}{2}\omega_{-,0}\epsilon^2. \tag{A.4c}$$

Here, I included the index zero for the frequencies just to make clear, that there is no dependence on the trap imperfections hidden in the frequencies. In equation (15) of [40], a relatable formula for the frequency shift of ω_z is given:

$$\omega_z = \omega_{z,0}\sqrt{1-\frac{3}{2}\sin^2(\theta)\left(1+\frac{1}{3}\epsilon\cos(2\phi)\right)}. \tag{A.5}$$

A series expansion of the square root and using $\sin(\theta)\approx\theta$ for $\theta \ll 1$ reproduces equation (A.4b).
For the frequency shift of ω_+, there is no comparable formula given in [40].
However, neglecting the third term of equation (17) therein, multiplying with ω_+ and using equation (A.5) gives

$$\omega_c = \omega_+\left(1+\frac{1}{2}\left(\frac{\omega_{z,0}\alpha}{\omega_+}\right)^2\right), \tag{A.6}$$

using the short notation $\alpha = \sqrt{1-\frac{3}{2}\sin^2(\theta)\left(1+\frac{1}{3}\epsilon\cos(2\phi)\right)}$. This can be solved for ω_+ and then approximated:

$$\begin{aligned}
\omega_+ &= \frac{\omega_c}{2}\left(1+\sqrt{1-\frac{2\omega_{z,0}^2\alpha^2}{\omega_c^2}}\right)\\
&= \frac{\omega_c}{2}\left(1+\sqrt{1-\frac{2\omega_{z,0}^2}{\omega_c^2}}-\sqrt{1-\frac{2\omega_{z,0}^2}{\omega_c^2}}+\sqrt{1-\frac{2\omega_{z,0}^2\alpha^2}{\omega_c^2}}\right)\\
&= \omega_{+,0}+\frac{\omega_c}{2}\left(\sqrt{1-\frac{2\omega_{z,0}^2\alpha^2}{\omega_c^2}}-\sqrt{1-\frac{2\omega_{z,0}^2}{\omega_c^2}}\right)\\
&\approx \omega_{+,0}+\frac{\omega_{z,0}^2}{2\omega_c}\left(1-\alpha^2\right)\\
&= \omega_{+,0}+\frac{\omega_{z,0}^2}{\omega_c}\frac{3}{4}\sin^2(\theta)\left(1+\frac{1}{3}\epsilon\cos(2\phi)\right).
\end{aligned} \tag{A.7}$$

This reproduces equation (A.4a)
For the frequency shift of ω_-, equation (16) in [40] gives

$$\omega_- = \frac{\omega_z^2}{2\omega_+}\sqrt{1-\epsilon^2}\left[1-\frac{3}{2}\sin^2(\theta)\left(1+\frac{1}{3}\epsilon\cos(2\phi)\right)\right]^{-3/2}. \tag{A.8}$$

Again, the dependency of the axial frequency on the trap imperfection needs to be inserted into this formula. In principle, the dependency of the modified cyclotron frequency needs to be considered as well. However, it turns out that, the axial dependency is dominating. A series expansion again reproduces equation (A.4c). To measure the angle of a trap in practice one can use the formula

$$\omega_+ + \omega_- - \omega_c = \omega_- \left(\frac{9}{4}\theta^2 - \frac{1}{2}\epsilon^2 \right) \tag{A.9}$$

derived in [42]. This formula can be reproduced by adding equation (A.4a) and equation (A.4c), neglecting cross terms of order $\theta^2\epsilon$ and the contribution of ϵ^2 to $\Delta\omega_+$, which is supressed by the quantity ω_-/ω_+.

Danksagung

An dieser Stelle möchte ich allen danken, die zum Gelingen dieser Arbeit beigetragen haben.

Lieber Klaus, vielen Dank für alles, was du die letzten Tage für mich getan hast. Ich finde es unglaublich gut, wie du trotz deiner großen Arbeitsgruppe jederzeit für jeden ein offenes Ohr hast. Mit deiner positiven Art schaffst du es, deine Studenten immer wieder neu zu motivieren. Durch dein Organisationstalent hast du mir immer den Rücken frei gehalten, danke dafür.

Herrn Markus Oberthaler möchte ich für die bereitwillige Übernahme der Zweitkorrektur danken.

Lieber Sven, vielen Dank für die unzähligen Erklärungen und Gespräche, sei es im Labor oder auch mal privat. Dein tiefes Verständnis in quasi allem, was du anfasst, zusammen mit deiner Bescheidenheit beeindrucken mich jedes mal aufs neue. Du warst mir die letzten Jahre über nicht nur ein toller Betreuer, sondern auch menschlich ein Vorbild, danke.

Lieber Florian, du warst in den letzten vier Jahren mein erster Ansprechpartner bei Problemen aller Art. Du hast mich mit offenen Armen im Labor aufgenommen und mich und Fabian in die Welt der Ionen geführt. Vielen Dank! Ich werde die intensiven Diskussionen, seien sie physikalischer oder gesellschaftlicher Natur, vermissen und wünsche dir alles Gute auf deinem weiteren Weg.

Lieber Fabian, fast drei Jahre lang standen wir zusammen im Labor, haben zusammen tolle Erfolge gefeiert oder auch mal Mist gebaut. Du warst immer ein guter Ansprechpartner und auf dein überragendes Gedächtnis war immer Verlass. Danke!

Dear Sangeetha, we did not work too closely yet, as I was mostly busy writing since you where here. Still, I enjoy our conversations during filling and am looking forward to work with you and Olesia.

Ich möchte Herrn Günter Werth danken. Ihr großer Erfahrungsschatz und Ihre postive Art haben mich immer inspiriert.

Ein großer Dank gilt dem ganzen proton g-factor team, vor allem Matt, Markus, Christian, Andi und Georg für tolle Gespräche in der Mensa und kurzfristige Hilfe bei Materialknappheit.

Ich danke auch Michael Jentschel, der mich auf die aktualisierte Gitterkonstante hingewiesen hat.

Mein Dank geht auch an die gesamte Infrastruktur des Instituts für Physik in Mainz, insbesondere der Werkstatt, die uns in Notlagen auch sehr kurzfristig geholfen hat, dem Team vom Heliumverflüssiger und der Institutsleitung.

Ich danke meiner Familie, insbesondere meinen Eltern und Großeltern, die mich zu jeder Zeit unglaublich unterstützt haben. Ohne euch wäre diese Arbeit niemals möglich gewesen, danke.

Danke an meine Freunde, vor allem David und Simon, für gelegentliche Hilfe beim Füllen, das Lesen der Arbeit und die schöne Zeit neben der Arbeit.
Liebe Ramona, vielen Dank für deine Geduld, vor allem in dieser letzten stressigen Phase vor der Abgabe. Deine Hilfe, nicht nur beim Korrektur lesen, sondern bei allen Dingen des täglichen Lebens, ist unschätzbar wertvoll. Danke.